

Roll-to-Roll Advanced Materials Manufacturing DOE Laboratory Collaboration - Early Stage R&D FY 2019 Final Report

ORNL/SPR-2020/1443

February 2020

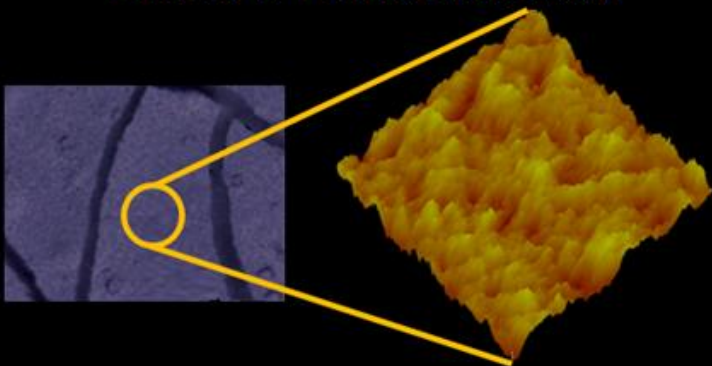
Funding provided by:

U.S. Department of Energy

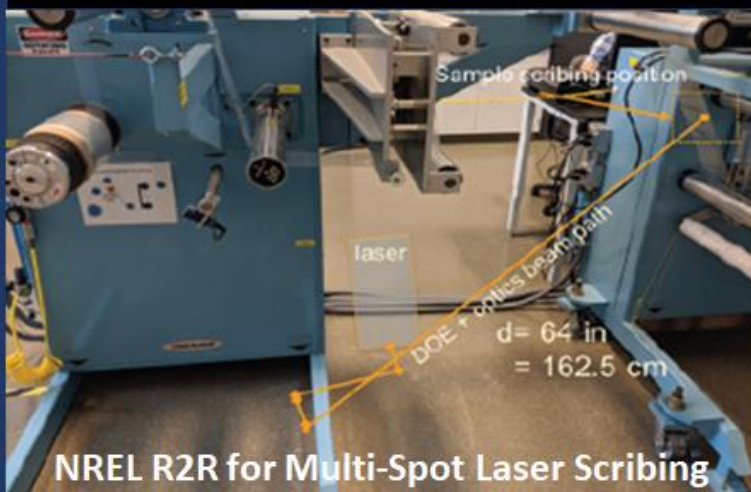
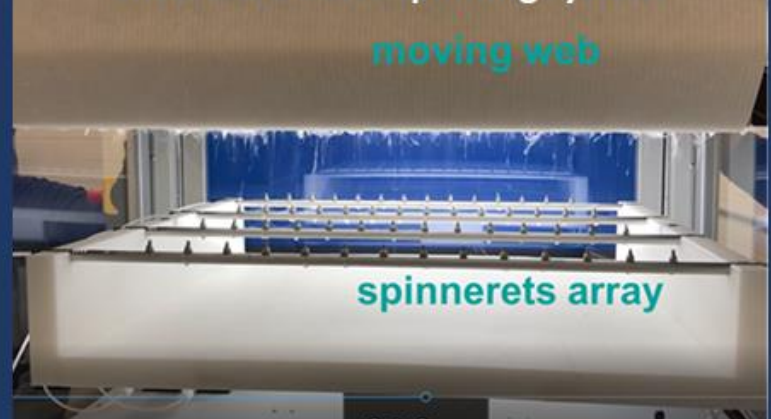
Office of Energy Efficiency and Renewable Energy

Advance Manufacturing Office

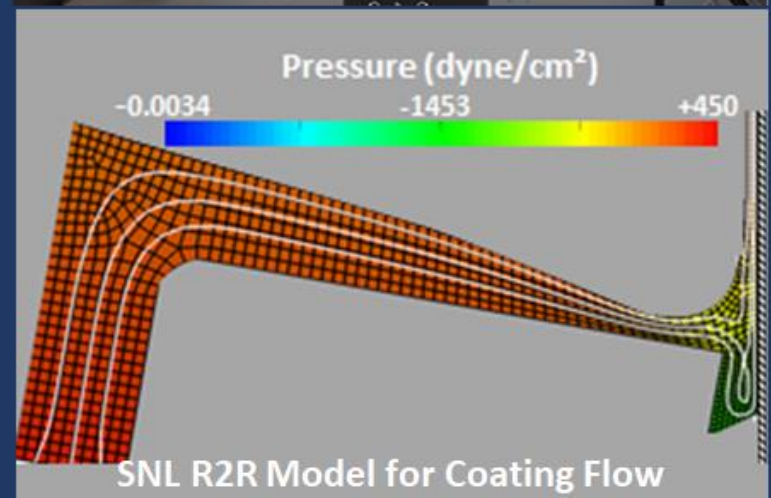
ORNL R2R Coating AFM Image



ANL R2R Electrospinning System



NREL R2R for Multi-Spot Laser Scribing



SNL R2R Model for Coating Flow



Disclaimer

This report was prepared as an account of work sponsored by an agency of the United States government. Neither the United States government nor any agency thereof, nor any of their employees, makes any warranty, express or implied, or assumes any legal liability or responsibility for the accuracy, completeness, or usefulness of any information, apparatus, product, or process disclosed or represents that its use would not infringe privately owned rights. Reference herein to any specific commercial product, process, or service by trade name, trademark, manufacturer, or otherwise does not necessarily constitute or imply its endorsement, recommendation, or favoring by the United States government or any agency thereof. The views and opinions of authors expressed herein do not necessarily state or reflect those of the United States government or any agency thereof.

DOCUMENT AVAILABILITY

Reports produced after January 1, 1996, are generally available free via US Department of Energy (DOE) SciTech Connect.

Website <http://www.osti.gov/scitech/>

Reports Produced before January 1, 1996, may be purchased by members of the public from the following source:

National Technical Information Service
5285 Port Royal Road
Springfield, VA 22161
Telephone 703-605-6000 (1-800-553-6847)
TDD 703-487-4639
Fax 703-605-6900
E-mail info@ntis.gov
Website <http://www.ntis.gov/help/ordermethods.aspx>

Reports are available to DOE employees, DOE contractors, Energy Technology Data Exchange representatives, and International Nuclear Information System representatives from the following source:

Office of Science and Technical Information
PO Box 62
Oak Ridge, TN 37831
Telephone 865-576-8401
Fax 865-576-5728
Email reports2osti.gov
Website <http://www.osti.gov/contact.html>

Foreword

Oak Ridge National Laboratory (ORNL), Argonne National Laboratory (ANL), Lawrence Berkeley National Laboratory (LBNL), and the National Renewable Energy Laboratory (NREL) performed as a collaborative Roll-to-Roll Advanced Materials Manufacturing (R2R AMM) Department of Energy (DOE) Laboratory Consortium in Fiscal Year (FY) 2016 through FY 2018. In June 2018, the Consortium responded to a FY 2019 Advanced Manufacturing Office (AMO) Lab Call, DE-LC-000L059, for Topic 3 titled “Roll-to-Roll Processing” with a proposal “Early-stage advanced national multi-laboratory roll-to-roll research and development collaboration with industrial Cooperative Research and Development Agreement (CRADA) collaboration”. Over 50 white papers were solicited from multiple national laboratories, including the four Consortium laboratories, and five were selected for including in the proposal to the Lab Call. One paper from Sandia National Laboratories (SNL), Albuquerque, NM was selected, so SNL was added to the multi-laboratory collaboration. The R2R AMM DOE Laboratory Collaboration (i.e. R2R Collaboration) proposal was accepted for funding in FY 2019 through FY 2021 contingent on annual budget authorizations.

This R2R Collaboration’s goal is to advance our understanding of R2R processing for high-throughput advanced manufacturing through an early-stage research approach to enable new devices and lower the cost of existing processing routes for competitive U.S. manufacturing. The projects directly address the AMO’s Multi-Year Program Plan challenges for the use of multilayer coating technologies applicable to flexible and integrated electronics, separation membranes, photovoltaics (PV), and selective barrier materials addressing both of the AMO identified targets of technologies with a 10x production capacity increase and in-line instrumentation tools to evaluate the performance and functionality. Working with industry partners through CRADA projects, the R2R Collaboration is addressing challenges and barriers for continuous R2R processing, registration and alignment, scalability, materials compatibility and defects, stoichiometry control and the availability of materials data for R2R processing. The R2R Collaboration targets the development of technologies that reduce the cost per manufactured throughput of continuous R2R manufacturing processes, and the development of in-line instrumentation tools that will evaluate the quality of single and multilayer materials on process weblines.

The FY 2019 core program consisted of a broad range of research task areas focused on colloidal chemistry and slurry formulation, novel R2R deposition systems based on electrospinning (ES) technology, in-line real-time non-destructive evaluation (NDE) and advanced in-situ testing capabilities, physics and methodologies for multilayer coatings, ink formulations and rheology, modeling and simulation of drying and curing processes, and continuum-scale models for the capillary hydrodynamics of coating deposition. Three CRADA projects that were initiated in FY 2018 continued into FY 2019 with one completing in May 2019. The primary applications of the research in the CRADA projects include freeze casting studies, advanced separator for flexible solid-state lithium ion batteries, diffractive multiplexing laser patterning of flexible organic PV modules, and electrodes for low-cost hydrogen production. The Collaboration laboratories have unique assets that complement each other for the research, development, testing and evaluation of these energy saving technologies. These include the following infrastructure, testing, operations, characterization, and analysis capabilities:

- Precision coating equipment
- Pilot-scale R2R operations support
- Device assembly assistance
- Electrochemical and cell performance evaluation
- State-of-the-art microscopy and tomography
- Surface characterization
- X-ray and neutron characterization facilities
- Computational science

- Process modeling and characterization capabilities
- World-class data analysis
- In-line quality control (QC)

DOE cost targets for advanced energy storage and conversion applications will not be met without significant and timely advancements in R2R manufacturing. Required R2R advances include adaptation of existing processing methods (gravure, slot die, slide die) and development of novel methods (simultaneous multilayer coatings) that have the potential to significantly impact U.S. manufacturing sector recovery, environmental applications in clean water, energy security, and sustainable transportation. Economies of scale through increased manufacturing volumes based on traditional assembly and processing methods will not suffice. For example, current baseline technology cell costs in the lithium ion battery industry are about 2.5× the \$100/kilowatt-hour ultimate target of DOE Vehicle Technologies Office (VTO). [1] To increase the capacity from 250 Wh/kg to 1000 Wh/kg for anode materials, novel R2R processing technologies will be required. Furthermore, polymer electrolyte membrane fuel cell (PEMFC) stacks currently cost almost 10× in low volumes compared to the ultimate cost of the DOE Fuel Cells Technology Office (FCTO) target of \$20/kilowatt by the year 2020. [2] Water consumption for renewable energy technologies can be as high as a medium value 4,500 gallons/megawatt-hours and more than 44,000 gallons/megawatt-hours for non-renewable energy applications. [3] New technologies are needed to increase the capacity of these systems to meet future needs. Other examples of the Energy Efficiency and Renewable Energy (EERE) Office funded technologies that have a similar cost-target issue are chemical-process industry membranes, window films, PV films, and electronic films. The EERE AMO is poised to assist in reaching the low dollars per unit costs of these various critical energy related applications through addressing R2R manufacturing problems common to each application.

Preface

The following report provides a description of the program structure and technical accomplishments made during FY 2019 to overcome challenges for expanding use of R2R technologies and processes for clean energy applications. Areas of interest encompass colloidal chemistry, surfactant research, slurry processing, and drying and curing; novel R2R deposition using ES; methodologies for ink formulations, multilayer coatings, rheology and deposition; fabrication and in situ characterization of prototype components and devices; and in-line real-time NDE. The particle- and continuum-scale modeling and simulations for these layered materials, energy storage technologies and continuous manufacturing processes being developed will allow for improvements and advances in R2R manufacturing applications, particularly for design and scale-up. This report documents the research conducted by five DOE national laboratories as a collaborative group with participation from industry partnerships. The approach is to develop advanced and novel materials, methods and techniques for multilayer coatings and depositions that can be used for R2R processes that are applicable to enhancing the performance of renewable energy technologies and systems. This effort supports building the foundation of technologies, processes and a U.S. manufacturing base that will enable an order of magnitude in shorter process development cycles with the pathway for initial commercialization within months instead of years.

Acknowledgements

First and foremost, the following scientists, investigators and technical support who are working diligently to realize their innovative ideas and technological developments in R2R processing and their desire to deploy them broadly for energy storage applications are acknowledged for their contributions:

ANL: Deborah Myers, Jae Hyung Park, Albert Lipson, Donna Brunner, Yuepeng Zhang, Erik Dahl, Devon Powers, Brian Ingram, Lei Cheng

ORNL: David Wood, Jianlin Li, Marissa Wood, Jaswinder Sharma, Georgios Polyzos, Erin Creel, Kelsey Grady, Ritu Sahore, Charl Jafta

NREL: Peter Rupnowski, Brian Green, Scott Mauger, KC Neyerlin, Sunil Khandavalli, Jason Pfeilsticker, Min Wang, Janghoon Park, Nisha Sharma, Maikel van Hest, Bertrand Tremolet deVillers

LBNL: Fuduo Ma, Vince Battaglia, Kenny Higa, Ravi Prasher, Zhi Huang

SNL/University of New Mexico: Kristianto Tjiptowidjojo, Chris Wall, Ben Wall, Robert Malakhov

DOE EERE AMO: Brian Valentine and Bob Gemmer (Technical Project Management)

DOE EERE FCTO: Nancy Garland (Technical Project Management)

We would also like to acknowledge the principal investigators and project managers at Fisker, Inc.; Navitas Systems, LLC; SolarWindow Technologies, Inc.; General Motors, Nel Hydrogen/Proton OnSite, Giner, Plug Power, Eastman Kodak, and Saint-Gobain for their coordination and collaboration on the R2R projects.

Finally, we would also like to acknowledge the contributions of Fred Crowson, Energetics, for his project management assistance and involvement in preparing and publishing this report.

The research at

- Oak Ridge National Laboratory, managed by UT Battelle, LLC for the U.S. Department of Energy, under contract DE-AC05-00OR22725
- Argonne National Laboratory, managed by University of Chicago Argonne, LLC for the U.S. Department of Energy, under contract DE-AC02-06CH11357
- Lawrence Berkeley National Laboratory, managed by University of California for the U.S. Department of Energy, under contract DE-AC02-05CH11231
- National Renewable Energy Laboratory, managed by Alliance for Sustainable Energy, LLC for the U.S. Department of Energy, under contract DE-AC36-08GO28308
- Sandia National Laboratories managed and operated by National Technology and Engineering Solutions of Sandia, LLC., a wholly owned subsidiary of Honeywell International, Inc., for the U.S. Department of Energy's National Nuclear Security Administration under contract DE-NA-0003525.

was sponsored by EERE AMO, Valri Lightner and Brian Valentine.

Acronyms and Abbreviations

°C	degrees Centigrade
μm or μ	micrometers or microns
1C, 2C etc.	a charge current of 1, 2, etc. time the rated capacity
A	amp
A/cm ²	amps per centimeter squared
AFM	atomic force microscopy
AMM	Advanced Materials Manufacturing
AMO	Advanced Manufacturing Office
ANL	Argonne National Laboratory
APS	Advanced Photon Source
at%	atomic percent
BET	Brunauer-Emmett-Teller
C	chemical symbol for carbon
CA	California
cm ²	centimeter squared
CMC	carboxymethyl cellulose
CO	Colorado
CRADA	Cooperative Research and Development Agreement
c-LLZO	cubic phase lithium lanthanum zirconium oxide
D _f	fractal dimension
DC	District of Columbia
DMF	dimethylformamide
DOE	U.S. Department of Energy (when referring to the agency)
DOE	diffractive optical element (when referring to laser scribing)
DOL	diffractive optics-based laser
EDS	energy dispersive X-ray spectroscopy
EERE	Energy Efficiency and Renewable Energy
e.g.	abbreviation meaning “for example”; a Latin phrase, “ <i>exempli gratia</i> ” meaning “for the sake of example”
ES	electrospinning
etc.	abbreviation for the Latin phrase “ <i>et cetera</i> ” which means “and so forth”
FCTO	Fuel Cell Technologies Office
FY	fiscal year
g	gram or grams
GDE	gas diffusion electrode
h or hr	hour
HFP	hexafluoropropylene
Hg	chemical symbol mercury
HSC	high surface-area carbon
I/C or I:C	ionomer-to-carbon ratio
IL	Illinois
IPA	isopropyl alcohol
IrO _x	iridium oxohydroxide
IrO ₂	iridium oxide
kg	kilogram
LBNL	Lawrence Berkeley National Laboratory
Li	chemical symbol for lithium

LLZO	lithium lanthanum zirconium oxide, $\text{Li}_7\text{La}_3\text{Zr}_2\text{O}_{12}$
LSC	low surface-area carbon
LSCF	lanthanum strontium cobalt iron oxide, $\text{La}_{0.6}\text{Sr}_{0.4}\text{Co}_{0.2}\text{Fe}_{0.8}\text{O}_3$
mAh/g	milliamp-hour per gram
MERF	Materials Engineering Research Facility
mg/cm ²	milligram per square centimeter
MgO	magnesium oxide
min(s)	minute(s)
mm	millimeters
mmol	millimole
Mn	chemical symbol for manganese
MW	molecular weight
MWh	megawatt-hour
NDE	non-destructive evaluation
ml or mL	milliliter
nm	nanometer
NMC	nickel-manganese-cobalt
NMP	N-Methyl-2-pyrrolidone
nPA	normal propyl alcohol (or normal propanol)
NREL	National Renewable Energy Laboratory
OCV	open circuit voltage
ORNL	Oak Ridge National Laboratory
PAA	polyacrylic acid
PAN	polyacrylonitrile
PEM	polymer electrolyte membrane
PEMFC	polymer electrolyte membrane fuel cell
PEO	polyethylene oxide
pH	the negative logarithm of the effective hydrogen-ion concentration or hydrogen-ion activity in gram equivalents per liter of the solution
Pt	chemical symbol for platinum
Pt/C	platinum to carbon ratio
PV	photovoltaic
PVDF	polyvinylidene fluoride
PVP	polyvinylpyrrolidone
QC	quality control
R2R	roll-to-roll
rpm	revolutions per minute
s	second(s)
SAXS	small-angle X-ray scattering
SEM	scanning electron microscope (or microscopy)
SLC	designation by Superior Graphite for a natural graphite surface treated with an amorphous carbon coating
SNL	Sandia National Laboratories
STEM	scanning transmission electron microscopy
TEM	transmission electron microscopy
T _g	glass transition temperature
TN	Tennessee
U.S.	United States
USAXS	ultra-small angle X-ray scattering

vs.	versus
VTO	Vehicle Technologies Office
wt%	percent by weight
XPS	X-ray photoelectron spectroscopy
XRD	X-ray diffraction
XRF	X-ray fluorescence spectroscopy

Table of Contents

Disclaimer.....	i
Foreword.....	ii
Preface	iv
Acknowledgements.....	v
Acronyms and Abbreviations	vi
Table of Contents.....	ix
List of Figures.....	xi
List of Tables	xvii
Executive Summary	1
Accomplishments	3
Technology Assessment.....	5
Roll-to-Roll Advanced Materials Manufacturing DOE Laboratory Collaboration Project Overview	6
Collaboration Contacts.....	6
Annual Operating Plan Title and Corporate Planning System (CPS) Agreement Numbers	7
Project Introduction	8
Objectives	8
Approach.....	8
Core Program	8
FY 2020 Plans	12
Technology Transfer Paths.....	15
Results.....	15
Novel R2R Deposition System Based on ES Technology and Advanced/In Situ Characterization and Testing (ANL Lead Laboratory)	15
R2R ES Platform Development	15
Advanced Materials and ES Recipe Development	18
In-situ X-ray Study of the ES Process	20
Fabrication Toward Prototype Components and Devices.....	21
Advanced Ink and Membrane Characterization.....	22
Colloidal Chemistry, Surfactant Research, Slurry Processing, Deposition and Drying/Curing Methods (ORNL Lead Laboratory).....	27
Colloidal Chemistry and Slurry Processing	27

Deposition and Drying/Curing.....	30
R2R ES Platform Development Support	45
Physics and Methodologies for Multilayer Coatings/Deposition; Fabrication and In Situ Testing of Prototype Components and Devices; and Novel Non-Destructive Evaluation, Quality Control and Metrology (NREL Lead Laboratory)	54
Cutting-Edge Coating and Deposition Science for R2R Applications.....	54
Fabrication and In Situ Testing of Prototype Components and Devices	65
Novel NDE, QC, and Metrology Methods.....	67
Macroscopic Mathematical Model of the Drying of a Single Layer Generic Slurry Containing Monodispersed Colloidal Particles, Binder and Solvent (LBNL Lead Laboratory)	69
Slurry Drying Model.....	69
Validated Continuum-Scale Models to Accelerate Design and Scale-up of Simultaneous Die Coating Process Technology (SNL Lead Laboratory).....	71
Model Development and Validation for Multilayer R2R Applications	71
Collaboration/Coordination/Outreach/CRADA Projects	73
Core Program.....	73
CRADA Projects.....	73
Fisker, Inc.....	73
Navitas Systems, LLC.....	83
SolarWindow Technologies, Inc. (SWT).....	94
Nel/Proton OnSite	98
Workforce Development/Educational Outreach	98
Challenges/Contingencies	99
Risks and Risk Handling	99
Project Ratings	101
Conclusions.....	102
Key Publications	103
References.....	104

List of Figures

Figure 1. The R2R AMM DOE Laboratory Collaboration team and major research efforts. Source: ORNL	1
Figure 2 ES configurations of (a) bottom-up spinning where nanofibers are projected upward and (b) top-down spinning where droplets fall onto the already-made nanofiber products under gravity. Source: ANL.....	16
Figure 3 A picture of the ES process for the R2R ES system implemented at the ANL MERF, which shows simultaneous fiber deposition from 56 needles on a moving web. Source: ANL.....	16
Figure 4 Fiber diameter as a function of evaporation rate for different concentrations of IPA in solution. Source: ANL.....	17
Figure 5 Comparison of fibers produced from precursors with and without IPA at different voltages and working distances for R2R ES process optimization. Source: ANL.....	17
Figure 6 LLZO precursor nanofibers deposited on an aluminum web at scale using R2R ES module. Source: ANL	18
Figure 7 SEM images of the as-spun LLZO polymer precursor nanofibers that were synthesized under the different voltages shown. Source: ANL.....	18
Figure 8 SEM images of as-spun LLZO polymer precursor nanofibers fabricated with optimum ES conditions. Source: ANL.....	19
Figure 9 SEM images of LSCF precursor nanofibers fabricated at different voltages. Source: ANL.....	19
Figure 10 (a) ES unit mounted at 12-ID-B beamline of APS for in-situ SAXS study and (b) generation of FeNi polymer precursor nanofibers recorded by a high-resolution camera at the beamline. Source: ANL	20
Figure 11 (a) 2D-SAXS data of FeNi nanofibers, (b) intensity vs. scattering vector ($I(q)$ - q) plots obtained from 2D-SAXS data (blue) and simulation (purple) and (c) SEM image of the studied nanofibers. Source: ANL.....	21
Figure 12 (a) TEM image and (b) X-ray profile of LLZO fibers after 700°C annealing. Source: ANL	22
Figure 13 PVDF-based polymer nonwoven structure for water filtration membrane application viewed from (a) top and (b) side. Source: ANL	22
Figure 14 USAXS profiles and fitting results for IrO_x inks with and without ionomer. IR2: 25wt% IrO_x , 0.2 Ionomer/Catalyst (I/C). IR1: 25wt% IrO_x , 0 I/C. Source: ANL	24
Figure 15 (a) USAXS scattering curves for 35wt% IrO_2 dispersions both without and with ionomer (2.4 wt%) in the inks. (b) The corresponding volume size distribution of the inks without and with ionomer. Source: ANL	25
Figure 16 USAXS results for 2.5wt% Nafion ionomer solution for N1: 10/90 nPA/ H_2O , N2: 25/75 nPA/ H_2O , N3: 50/50 nPA/ H_2O , N4: 75/25 nPA/ H_2O , and N5: 90/10 nPA/ H_2O dispersions listed in Table 1. Source: ANL	26
Figure 17 USAXS profiles for Pt/Vulcan-ionomer-solvent inks as a function of solvent mixture and ionomer. Source: ANL.....	27
Figure 18 SEM images of the carbon particles coated with Pt catalyst; carbon primary particle size is approximately 50 nm. Source: ORNL	28
Figure 19 (a) Area where EDS measurements were taken and the element maps for (b) platinum and (b) carbon atoms on the surface of the coated particles. Source: ORNL	28

Figure 20 (a) Survey XPS spectrum of the Pt/C particles and (b) XPS core data analysis and the element at% on the surface of the particles. Source: ORNL	29
Figure 21 Zeta potential measurements of Pt/C particles dispersed in water having 5% KNO ₃ . Source: ORNL	29
Figure 22 Zeta potential measurements of Pt/C particles dispersed in water, IPA and Nafion. Source: ORNL	30
Figure 23 Rheological properties of the slurries with 8 wt% and 10 wt% Pt/C content. Source: ORNL.....	31
Figure 24 SEM cross-section images of the GDE coated with 8 wt% slurry formulation at different magnifications. Source: ORNL.....	31
Figure 25 The area where EDS measurements were taken and the element maps according to EDS analysis of the 8 wt% coating on the GDE substrate. Source: ORNL	32
Figure 26 Optical microscope images of the coatings based on (a) and (b) for the 8 wt% and (c) and (d) 10 wt% formulations. Source: ORNL.....	32
Figure 27 Thickness profile measurements for the (a) and (b) 8 wt% and (c) and (d) 10 wt% coatings. Source: ORNL	33
Figure 28 Surface topography of the 8 wt% coating under (a) an optical microscope and (b) according to AFM imaging measurements. Source: ORNL.....	33
Figure 29 AFM surface profile of an area with well dispersed particles on the surface of the 8 wt% coating. Source: ORNL	34
Figure 30 AFM surface profile of an area with particle agglomeration on the surface of the 8 wt% coating. Source: ORNL	34
Figure 31 SEM images at different magnifications of the coated GDE using a slot-die technique. Source: ORNL	35
Figure 32 SEM cross-section image of the slot-die coated GDE. Source: ONRL.....	35
Figure 33 EDS analysis of the cross-section of the slot-die coated GDE. Source: ONRL	36
Figure 34 GDEs (4.5 inches x 2.5 inches) coated with slurries prepared at different mixing times. Source: ORNL	37
Figure 35 SEM images of the coated GDE for the slurry mixed for 15 min at 10,000 rpm. Source: ORNL	38
Figure 36 (a) EDS element map of the slurry according to (b) the EDS analysis for mixing 15 min at 10,000 rpm. Source: ORNL.....	39
Figure 37 SEM images for the coated GDE slurry mixed for 30 min at 10,000 rpm. Source: ORNL	41
Figure 38 SEM images for the coated GDE slurry mixed for 60 min at 10,000 rpm. Source: ORNL	42
Figure 39 SEM cross section images of the GDE with a Pt loading of 0.179 mg/cm ² . Source: ORNL	44
Figure 40 EDS element analysis of GDE cross section with a Pt loading of 0.179 mg/cm ² . Source: ORNL	44
Figure 41 SEM images of the coated GDE showing pronounced particle agglomeration. Source: ORNL.....	45
Figure 42 Schematic illustration of the experimental setup used for the nanofiber ES. Source: ORNL.	45
Figure 43 SEM image of electrospun LLZO nanofibers according to recipe 1. Source: ORNL	46
Figure 44 SEM image of electrospun LLZO nanofibers according to recipe 2. Source: ORNL	46

Figure 45 SEM image of electrospun LLZO nanofibers according to recipe 3. Source: ORNL	47
Figure 46 XRD plot of the annealed LLZO nanofibers. Source: ORNL	47
Figure 47 (a) Electrospun PAN fibers from Recipe 1 and (b) 10X magnification. Source: ORNL.....	48
Figure 48 (a) Electrospun PAN fibers according to recipe 2 and (b) at 20x magnification. Source: ORNL.....	49
Figure 49 Carbonization setup that was used to carbonize the PAN fibers. Source: ORNL	50
Figure 50 SEM images of the synthesized carbon nanofibers with diameters of 200-300 nm. Source: ORNL..	51
Figure 51 SEM images of the aluminum-LLZO nanofibers prior to their annealing with a diameter of approximately 200 nm. Source: ORNL	52
Figure 52 (a) XRD of the aluminum-LLZO powder mixed with MgO powder at several temperatures. (b) Peak assignment where the blue vertical lines correspond to the c-LLZO phase and the green vertical lines correspond to the MgO peaks. Source: ORNL	53
Figure 53 Heterogeneous ink rheology as a function of solids loading and solvent ratio. Source: NREL	54
Figure 54 (a) 2 wt% and (b) 5 wt% catalyst ink rheology as a function of ionomer addition for 50:50 water-to- nPA solvent ratio. Source: NREL.....	55
Figure 55 Results of empirical process window model for total dry thickness (assuming 5 wt% solids solutions) of a two-layer slide die coating as a function of flow rate. Source: NREL.....	55
Figure 56 Target dry thickness validation of three-layer configuration using analytical slide die model. Source: NREL.....	56
Figure 57 Factor impact contour plots for (a) the density and (b) the viscosity of the top layer ink. Source: NREL.....	56
Figure 58 Pt/LSC quadratic model outputs for (a) ink density, (b) viscosity at shear rates of 1/s, (c) surface tension and (d) viscosity at shear rates of 100/s. Source: NREL	58
Figure 59 (a) Cast membrane thickness as a function of coating gap and (b) proton conductivity of the cast membranes compared to a commercially available membrane. Source: NREL.....	59
Figure 60 (a) Simulated multilayer structures via ultrasonic spray and (b) standard individual-layer structures. Source: NREL.....	59
Figure 61 (a) Dummy ink rheology for catalyst ink and (b) ionomer solution (actual target inks in black). Source: NREL.....	60
Figure 62 Computer-aided design drawing of 3-layer slide die from Allied Die. Source: NREL.....	60
Figure 63 Steady-shear rheology of ionomer/PAA and ionomer/particle/PAA slurries over a PAA range of 5- 20 wt%. Source: NREL	61
Figure 64 Amplitude sweep shear rheology data for carrier-ionomer-particle slurries as a function of carrier (PAA) solids loading from 5-20 wt%. Source: NREL.....	62
Figure 65 (a) Extensional viscosity and (b) shear viscosity data for carrier-ionomer and carrier-ionomer- particle slurries. Source: NREL	62
Figure 66 Summary of fiber diameter as a function of PAA concentration for the process window study. Source: NREL.....	63

Figure 67 PAA spinning process window depiction; inset images show examples of droplets (no fibers), spinning mostly beads, and spinning good fibers, as well as viscous instability of the Taylor cone at high PAA wt%. Source: NREL	64
Figure 68 Full PEM electrode ink process window depiction with SEM insets showing resulting materials. Source: NREL.....	64
Figure 69 (a) Polarization performance of two multilayer sprayed cells (for comparison, performance should be at least 0.8 A/cm ² at 0.6 volts) and (b) optical microscopy of the sprayed membrane layer. Source: NREL.....	65
Figure 70 (a) Typical catalyst coated membrane cell structure with membrane (Nafion 211) sealing area and (b) the new structure for three-layer target construction (Cathode-D2020-Anode). Source: NREL	66
Figure 71 (a) Polarization performance of the ORNL cell without and with ionomer overlayer, and (b) ORNL cells compared to NREL R2R GDE cells. Source: ORNL	66
Figure 72 Optical micrographs for (a) a particle-polymer electrode, (b) an anionic membrane, (c) a cationic membrane and (d) a reverse osmosis membrane. Source: NREL.....	68
Figure 73 Attenuated total reflectance-infrared spectroscopy of polymer-particle inks during drying, with characteristic polymer peaks indicated, at (a) higher polymer content and (b) lower polymer content. Source: NREL.....	69
Figure 74 (a) Relative and (b) absolute particle positions in settling particle network submodel. Source: LBNL	70
Figure 75 Solid model in a finite element mesh. Source: SNL.....	71
Figure 76 Single layer mesh and pattern of pressure (color map) and flow (streamlines). Source: SNL.....	72
Figure 77 Two-layer pattern of pressure (color map) and flow (streamlines) for ORNL slot die geometry. Source: SNL.....	72
Figure 78 SEM fracture surface images of freeze tape cast (10 vol.% LLZO slurry) produced at thicknesses of 300 μ m, 220 μ m and 160 μ m and at various casting speeds. Source: LBNL	733
Figure 79 (a) Sintered dense/porous LLZO bilayer and (b) and (c) the cathode component infiltrated bilayer. Source: LBNL.....	74
Figure 80 (a) and (b) SEM images and (c) XRD analyses of as-received LLZO power and LLZO powder compacted (pellet) and heated to 1090°C for 3 hours where blue arrows indicate t-LLZO peaks. (d) Zeta potentials of as-received LLZO with selected dispersants at varying pH. Source: LBNL	75
Figure 81 (a) and (b) Fracture surface SEM images of freeze tape cast LLZO green tapes produced at LBNL, and (c) and (d) surface SEM images of green tapes produced at ORNL. Sources: LBNL and ORNL	76
Figure 82 Photographs of a water-based LLZO slurry (a) after mixing and (b) after ~30 mins. Source: ORNL	76
Figure 83 Zeta potential of LLZO in the presence/absence of dispersants. Source: ORNL	77
Figure 84 (a) SEM fracture surface image of freeze tape cast NEI LLZO green tape and (b) at 10x magnification. Source: LBNL.....	77
Figure 85 SEM fracture surface images of (a) a sintered porous/dense LLZO bilayer and (b) at 10x magnification. Source: LBNL.....	78
Figure 86 SEM images of the cross sections of the freeze tape cast porous tapes obtained with slurries that have either (a) double the amount of PAA or (b) double the amount of VANZAN compared to the original recipe shown in Table V. Source: ORNL	79

Figure 87 Schematic showing the areas of the tape that were characterized via SEM. Source: ORNL	80
Figure 88 SEM of the cross-sections from three different areas of the LLZO freeze tape cast green tape from the first run. Source: ORNL.....	81
Figure 89 Schematic highlighting the difference in the way the freeze tape cast was fractured for SEM imaging the cross-sections for the second run. Source: ORNL	82
Figure 90 SEM of the cross-sections from three different areas of the LLZO freeze tape cast green tape obtained from the second run. Source: ORNL.....	82
Figure 91 Voltage profiles for various separators: (a) Celgard, (b) Separator B and (c) Separator C. Source: ORNL	84
Figure 92 Rate performance comparison for three separators: (a) capacity and (b) normalized discharge capacity vs C-rate. Source: ORNL.....	84
Figure 93 OCV of cells with various separators during a 24-hour rest. Source: ORNL.....	85
Figure 94 Top view of the mechanical design for lines in the 3D-printed prototype mask. Source: ORNL	85
Figure 95 Substrate sprayed with the mask showing a cross-hatched line pattern . Source: ORNL	86
Figure 96 XRF data showing uniformity and shape of the sprayed lines. Source: ORNL	86
Figure 97 Ceramic coating on separators with various binders. (a) PVDF-HFP, (b) CMC and (c) PVDF-HFP and CMC. Source: ORNL.....	87
Figure 98 SEM images of (a) the Al_2O_3 coated separator and the (b) TiO_2 coated separator showing completely covered surfaces. Source: ORNL.....	88
Figure 99 Electrochemical impedance spectroscopy results for the Separator B separator with different thicknesses of Al_2O_3 coatings. Source: ORNL	88
Figure 100 Electrochemical impedance spectroscopy results for the separators coated with the different ratios of Al_2O_3 and TiO_2 . Source: ORNL	89
Figure 101 (a) 3D-printed spray mask and (b) alumina/crosshatch pattern-sprayed coating. Source: NREL	89
Figure 102 Separator with full interdigitated patterned coating showing spatial non-uniformities (e.g. lower left side of the image). Source: NREL	90
Figure 103 (a) N_2 physisorption isotherms of the uncoated and the differently coated separators with their corresponding BET surface areas and (b) their pore size distribution as calculated from the desorption data. Source: ORNL	91
Figure 104 The average contact angle formed from water droplets on five separators with different coatings and from Generation II electrolyte on the uncoated separator. Source: ORNL	91
Figure 105 Voltage profile and rate performance with various separators at rates of (a) C/10, (b) C/2, (c) 1C, and (d) 2C. (e) The performance for all separators at all rates from 0 to 45 cycles. Source: ORNL.....	92
Figure 106 OCV of cells with various separators. Source: ORNL	93
Figure 107 Side view of forward gravure setup. Source NREL	94
Figure 108 Patterned gravure rollers with a crosshatch pattern (top) and a diamond pattern (bottom). Source: NREL.....	94

Figure 109 (a) Annotated photo showing the proposed location of the laser and multiplexing optics on NREL diagnostic R2R line; (b) the R2R system for the multi-spot DOE scribing with the finished safety enclosure. Source: NREL.....	96
Figure 110 Optical microscope images of multiplexed DOL scribes in ZnO/ITO/PET as a function of laser spot focal distance. Source: NREL.....	97

List of Tables

Table I List of USAXS-SAXS Samples	23
Table II Unified Fitting Results of 2.5wt% Nafion Ionomer Solutions	26
Table III Sample List and Unified Fitting Results of Pt/Vulcan Inks	27
Table IV ES Process Conditions for PAA Process Window Study	63
Table V NEI LLZO Slurry Recipe for Freeze Tape Casting Transferred from LBNL to ORNL	78
Table VI Modified NEI LLZO Slurry Recipe for Freeze Tape Casting	80
Table VII Coin Cell Electrode Areal Loading and Composition	83
Table VIII Formulations of the Al ₂ O ₃ Slurries	86
Table IX Educational Development at the Collaboration Laboratories	98
Table X Risks Identified During FY 2019 and Their Mitigation	99
Table XI R2R AMM Laboratory Collaboration Project Ratings	101

Executive Summary

R2R processing is used to manufacture a wide range of products for various applications which span many industrial business sectors. The overall R2R methodology has been in use for decades and this continuous technique traditionally involves deposition of material(s) onto moving webs, carriers or other continuous belt-fed or conveyor-based processes that enable successive steps to build a final version which serves to support the deposited materials. Established methods that typify R2R include tape casting, silk-screen printing, reel-to-reel vacuum deposition/coating and R2R lithography. Products supported by R2R manufacturing include micro-electronics, electro-chromic window films, PVs, fuel cells for energy conversion, battery electrodes for energy storage, and barrier and membrane materials. Due to innovation in materials and process equipment, high-quality yet very low-cost multilayer technologies have the potential to be manufactured on a very cost-competitive basis. To move energy-related products from high-cost niche applications to the commercial sector, a means must be available to enable manufacture of these products in a cost-competitive manner that is affordable. Fortunately, products such as fuel cells, thin- and mid-film PVs, batteries, electrochromic and piezoelectric films, water separation membranes, and other energy saving technologies readily lend themselves to manufacture using R2R approaches. However, more early-stage research is needed to solve the challenge of linking the materials (particles, polymers, solvents, additives) used in ink and slurry formulations, though the ink processing, coating and drying processes, to the ultimate performance of the final R2R product, especially for a process that uses multiple layers of deposition to achieve the end product.

To solve the problems associated with this R2R “Grand Challenge”, the R2R AMM DOE Laboratory Collaboration is executing a research program with outcomes that will ultimately link modeling, processing, metrology and defect detection tools, thereby directly relating the properties of constituent particles and processing conditions to the performance of final devices. The Collaboration team and their research efforts with industry involvement are illustrated schematically in Figure 1. This collaborative approach was designed to foster identification and development of materials and processes related to R2R for clean-energy materials development. Using computational and experimental capabilities by acknowledged subject matter experts within the supported National Laboratory system, this project leverages the capabilities and expertise at each of five national laboratories to further the development of multilayer technologies that will enable high-volume, cost-competitive platforms.

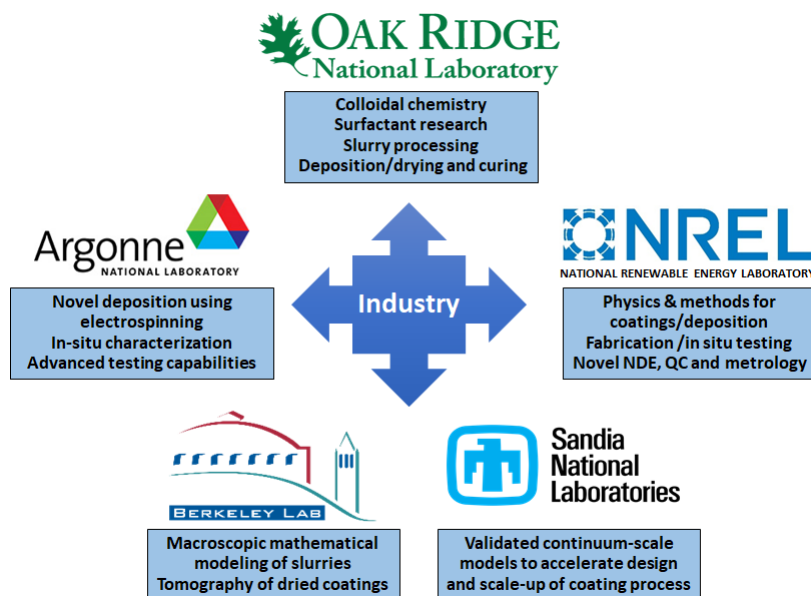


Figure 1. The R2R AMM DOE Laboratory Collaboration team and major research efforts. Source: ORNL

A typical R2R process has three steps: 1) mixing of particles and various constituents in a slurry, 2) coating of the ink/slurry mixture on a substrate, and 3) drying/curing and processing of the coating. Final performance of devices made via R2R processes is dependent on the active materials (e.g. electrochemical particles in battery or fuel cell electrodes) and the device structure that stems from the governing component interactions within the various steps. However, a fundamental understanding of the underlying mechanisms and phenomena is still lacking, which is why industrial-scale R2R process development and manufacturing is still largely empirical in nature.

The FY 2019 through FY 2021 program addresses aspects of the following two targets from the AMO Multi-Year Program Plan:

- Target 8.1 Develop technologies to reduce the cost per manufactured throughput of continuous R2R manufacturing processes.
 - Increasing throughput of R2R processes by 5 times for batteries (to 50 square feet per minute (50 ft²/min)) and capacitors and 10 times for printed electronics and the manufacture of other substrates and MEs used in support of these products.
 - Developing resolution capabilities to enable registration and alignment that will detect, align, and co-deposit multiple layers of coatings and print < 1-micron (1 μ m) features using continuous process scalable for commercial production.
 - Developing scalable and reliable R2R processes for solution deposition of ultra-thin (<10 nm) films for active and passive materials.
 - Develop in-line multilayer coating technology on thin films with yields greater than 95%.
- Target 8.2 Develop in-line instrumentation tools that will evaluate the quality of single and multilayer materials in-process.
 - Developing in-line QC technologies and methodologies for real-time identification of defects and expected product properties “in-use/application” during continuous processing at all size-scales with a focus on the “micro” and “nano” scale traces, lines, and devices
 - Developing technologies to increase the measurement frequency of surface rheology without significant cost increases with a goal of a 10-nanometer in-line profilometry at a production rate of 100,000 square millimeters per minute (100,000 mm²/min).

The category of electrochemical conversion devices that apply to fuel cells was selected to begin the FY 2019 efforts; however, research was kept general enough that other applications could include low-temperature water electrolysis, CO₂ separation/reduction and water filtration/purification. Of specific interest was ES technology. ES is a technology platform that is capable of fabricating advanced nanofiber-based materials across a wide range of applications and industrial domains. It offers high surface-to-volume ratio which makes nanofibers the ideal candidate for various applications where high porosity and high surface areas are desirable. There are currently a few barriers to commercialization of ES. It is limited to filtration applications produced in single-step, batch processes; advanced materials used in electronics, fuel cells and batteries require continuous, post-ES processing; complex multi-step physiochemical processes create challenges transferring technology from the bench to commercial production; and material transfer between process steps is time consuming. However, integration of R2R processing can enable the adoption of electrospun advanced materials into a wider range of applications

The FY 2019 collaborative effort successfully completed all tasks to develop an ES method using a R2R manufacturing process and to provide continuum-scale modeling, simulation, processing, and manufacturing techniques and metrology that demonstrate the feasibility and potential for scale-up. A R2R ES capability was established at ANL, which demonstrated fabrication of polymer nanofiber membranes on a 0.5 meter wide moving web using 56 nozzles. Nanofibers were produced using the ES system at ANL for three applications: (1) Li₇La₃Zr₂O₁₂ (LLZO) solid electrolyte, (2) La_{0.6}Sr_{0.4}Co_{0.2}Fe_{0.8}O₃ (LSCF) oxide fuel cell electrode,

and polyvinylidene fluoride (PVDF) water filtration membrane. In-situ small angle X-ray scattering (SAXS) was conducted at ANL's Advanced Photon Source (APS) to accelerate ES process optimization. ANL and ORNL both fabricated cubic phase LLZO (c-LLZO) from the electrospun precursors through post-annealing at temperatures well below the powder LLZO sintering temperatures (1100 °C), showing the benefit of the ES technology.

ORNL produced uniform PEMFC cathode gas diffusion electrode (GDE) coatings of uniform thickness on their pilot slot-die coating line and a membrane electrode assembly without an overlayer on the cathode with reasonable performance. NREL developed an empirical slide die coating window model and full-quadratic ink models for catalyst ink surface tension using the Box-Behnken methodology and completed a study for a multi-region process window. LBNL developed a generic particle network settling model as part of its longer-term coating drying modeling efforts but recognizing the deep lack of fundamental knowledge about the concentrated dispersions of interest, proposed a set of novel experiments for probing the influence of component interactions on macroscopic dispersion behavior. LBNL proposed to design and execute these experiments in order to obtain information that will be incorporated into its dispersion mixing and multilayer coating drying models. SNL completed two-layer slide and slot coating models using Goma 6.0. The models are equipped for slot- and slide-deposition systems with accommodation for three or more simultaneous miscible layers. SNL also advanced a user-interface that will greatly ease analysis of slide and slot-die coating head design.

Technology transfer for these and other technologies applicable to R2R manufacturing was initiated through collaboration with industry partners and through the continuation of three CRADA projects with industry and completion of one of those projects.

Accomplishments

Highlights of the FY 2019 accomplishments for the primary tasks at each laboratory are listed below.

Core Program Projects

ANL Novel R2R Deposition System Based on ES Technology and Advanced/In Situ Characterization and Testing Capabilities

- Fabricated nanofibers for three applications: (1) LLZO solid electrolyte, (2) LSCF oxide fuel cell electrode, and PVDF water filtration membrane.
- Developed R2R ES capabilities that include a 0.55 m x 30 m (width x length) moving web, 56 nozzle spinnerets running at a maximum homogeneous coating speed of 3 m/min, and ES recipes that are tailored for a high deposition rate. R2R fabrication of PVDF fibers was demonstrated.
- Achieved optimum ES recipes for LLZO precursor fiber fabrication using in-situ SAXS, which accelerated the development speed of LLZO. Fabricated nanocrystalline high-ionic-conductivity c-LLZO fibers out of the polymer precursor fibers at 700°C.

ORNL Colloidal Chemistry, Surfactant Research, Slurry Processing, Deposition and Drying and Curing and Curing Methods

- Optimized PEMFC cathode catalyst ink formulations by developing standard mixing protocol and equipment with NREL, quantifying zeta potentials of ink components, and measuring ink rheological properties for high-solids-loading slot-die coating formulation.

- Produced uniform PEMFC cathode GDE coatings with an ink composition of 12.16% Solids, 8 wt% platinum to carbon (Pt/C) on the ORNL pilot slot-die coating line with a uniform coating thickness $\approx 20\ \mu\text{m}$ and micron-size cracks.
- Coated cathode GDEs without an ionomer overlayer (0.38 and $0.18\ \text{mg-Pt}/\text{cm}^2$) resulting in performance comparable to the NREL baseline GDE spraying and slot-die coating approaches with loadings of $0.1\ \text{mg Pt}/\text{cm}^2$.
- Fabricated c-LLZO, which is several orders of magnitude more conductive than the tetragonal phase, after annealing at 700°C for two hours using a scalable recipe for the R2R system at ANL.

NREL Physics and Methodologies for Multilayer Coatings/Deposition; Fabrication and In Situ Testing of Prototype Components and Devices; and Novel NDE, Quality Control and Metrology

- Leveraged an empirical slide die coating window model to predict target multi-layer coating structures and coatability and inform continuum-scale model development
- Developed full-quadratic ink models for target multi-layer ink surface tension, viscosity and density using the Box-Behnken methodology
- Provided ink and coating models and property measurements to SNL to coordinate on the development of multi-layer slide die continuum models
- Specified and ordered three-layer slide die for upcoming experiments
- Completed a study showing a multi-region ES process window for a widely used polyacrylic acid (PAA) carrier polymer characterized by droplet spraying, spinning of fibers and beads (mostly fibers), and an unstable flow region with viscous instability in the Taylor cone.

LBNL Macroscopic Mathematical Model of the Drying of a Single Layer Generic Slurry Containing Monodisperse Colloidal Particles, Binder, and Solvent

- Developed generic particle network settling model with intuitively reasonable results; however, limited available information on dense, multicomponent suspensions, along with assumptions made to build model, suggested that greater understanding of component-level interactions during drying is needed.
- Began planning for experiments to obtain information needed for model development using a wide array of analytical tools, including those at the Advanced Light Source (ALS).

SNL Validated Continuum-Scale Models to Accelerate Design and Scale-Up of Simultaneous Die Coating Process Technology

- Completed two-layer slide coating models using Goma 6.0. The Goma 6.0 software was a 2014 Research and Development 100 Award Winner, with the award in part due to prior successes in applying the software for process modeling of pre-metered coating flow deposition.
- Designed models for slot- and slide-deposition systems with accommodation for three or more simultaneous miscible layers (multiple layers of varying rheology).
- Analyzed the one- and two-layer coating geometries for the as-drawn NREL slide die and ongoing single and two-layer slot-die coating work at ORNL. For two-layer systems, the model can predict

interlayer and free surface shape at varying flowrates and web speeds. Current work focused on minimizing flow recirculation near interlayer and preventing interlayer mixing.

- Advanced a continuum scale drying and solidification model for polymer-solvent systems and verified the implementation in Goma 6.0 with published literature studies.

CRADA Projects

Three CRADA projects that initiated in mid-FY 2018 continued through FY 2019 with one project completing in May 2019. Fisker, Inc. partnered with LBNL and ORNL to demonstrate all-solid-state batteries based on LLZO separators and cathode scaffolds and scaled a freeze casting coating process to the pilot level at ORNL. Initial recommendations were made to Fisker, Inc. on how the freeze casting process could be industrially scaled. Navitas Systems, Inc. partnered with ORNL and NREL to demonstrate R2R production of an advanced separator for lithium ion batteries. ORNL and NREL developed thermal and mechanical coating inks, coating processes, and a patterned deposition method as well as conducted cell testing. Navitas also began some trial operations handling the separator in a R2R manner at their product site. SolarWindow Technologies, Inc. partnered with NREL and ANL to demonstrate diffractive multiplexing for high-throughput R2R laser patterning of flexible organic PV modules. NREL selected a diffractive-optical-element (DOE)-based multiplexing system for R2R laser scribing that will drastically reduce up-front capital and on-going operational costs compared to currently used laser/optics systems and will also increase process speeds over galvanometer step-and-scan systems. Scribing experiments were initiated in FY 2019. Nel/Proton OnSite will partner with NREL, ORNL, and ANL in FY 2020 to research R2R manufacturing of advanced (low-loading, directly coated onto membrane) electrolysis electrodes for low-cost hydrogen production. The CRADA was initiated in September 2019 at the end of FY 2019. NREL will perform ink characterization and optimization and develop metrology capabilities, ORNL will conduct R2R coating experiments, and ANL will perform advanced electrode characterization.

Collaboration and Outreach

The R2R AMM DOE Laboratory Collaboration team participated in bi-monthly review meetings with DOE AMO and FCTO Technical Project Officers to ensure information for each project was available on a continuous and regular basis. Team members also presented at the Association of International Metallizers, Coaters and Laminators, TechConnect World Innovation Conference, the 2019 DOE Hydrogen and Fuel Cells Program and Vehicle Technologies Office Annual Merit Review and Peer Evaluation Meeting, the 2019 AMO Peer Review, the 2019 ASME Power and Energy Conference and Exhibition, the 20th International Coating Science and Technology Symposium, Beyond Lithium-Ion XI Symposium, and the Electro Chemical Society 2019 Spring Meeting.

As a team, laboratory principal investigators collaborated with the industry partners as part of the CRADA projects described above. Educational outreach by the R2R AMM DOE Laboratory Collaboration has supported a total of 28 post docs, graduate and undergraduate students, and interns from 24 separate universities.

Technology Assessment

Efforts for FY 2019 began in February 2019 due to late receipt of funding. Because of the nature of the early-stage research tasks, the technologies under development were not matured sufficiently for transfer to industry; however, technology transfer for these and other technologies applicable to R2R manufacturing was initiated through collaboration with industry partners and through the continuation of three CRADA projects with industry. One CRADA project was completed in FY 2019. Since this is a three-year research program, the other technologies under development are expected to mature for commercialization by FY 2021.

Roll-to-Roll Advanced Materials Manufacturing DOE Laboratory Collaboration Project Overview

Collaboration Contacts

Claus Daniel, Project and Collaboration Team Lead

Oak Ridge National Laboratory (ORNL)
National Transportation Research Center
2360 Cherahala Blvd.
Knoxville, TN 37932
Phone: 865-946-1544
Email: danielc@ornl.gov

David L. Wood III, ORNL Project Team Lead

Oak Ridge National Laboratory (ORNL)
National Transportation Research Center
2360 Cherahala Blvd.
Knoxville, TN 37932
Phone: 865-574-1157
Email: wooddl@ornl.gov

Gregory K. Krumdick, ANL Project Team Lead

Argonne National Laboratory (ANL)
9700 S. Cass Avenue
Building 362
Argonne, IL 60439-4844
Phone: 630-252-3952
Email: gkrumdick@anl.gov

Michael Ulsh, NREL Project Team Lead

National Renewable Energy Laboratory (NREL)
15013 Denver West Parkway
Golden, CO 80401
Phone: 303-275-3842
Email: Michael.Ulsh@nrel.gov

Vince Battaglia, LBNL Project Team Lead

Lawrence Berkeley National Laboratory (LBNL)
1 Cyclotron Road
MS 70R 0108B
Berkeley, CA 94720
Phone: 510-495-2679
Email: vsbattaglia@lbl.gov

P. Randall (Randy) Schunk, SNL Project Team Lead

Sandia National Laboratories (SNL)
Advanced Materials Laboratory
1001 University Blvd., SE
Albuquerque, NM 87106

Phone: 505-272-7603
Email: prschun@sandia.gov

Brian Valentine, DOE Roll-to-Roll Technical Project Officer

Department of Energy (DOE)
Energy Efficiency and Renewable Energy (EERE), EE-5A
Advanced Manufacturing Office (AMO)
1000 Independence Ave., S.W., Suite 5F-063
Washington, DC 20585-0121
Phone: 202-586-9741
E-mail: brian.valentine@ee.doe.gov

Technical Contacts:

ORNL: Jianlin Li, Yarom Polsky, Georgios Polyzos, Jaswinder Sharma, Erin Creel
ANL: Deborah Myers, Yuepeng Zhang, Erik Dahl
NREL: Scott Mauger, Peter Rupnowski, Maikel Van Hest
LBNL: Kenny Higa, Marca Doeff

Industry Partners:

Fisker, Inc.
Navitas Systems LLC
SolarWindow Technologies, Inc.
Nel/Proton OnSite
General Motors
Giner
Plug Power
Saint-Gobain
Eastman Kodak

Annual Operating Plan Title and Corporate Planning System (CPS) Agreement Numbers

Roll-to-Roll Manufacturing Science and Applications: From Ideal Materials to Real-World Devices

ORNL CPS# 97995
ANL CPS #s 29915, 32553 and 32681
NREL CPS #97995
LBNL CPS #31112
SNL CPS #35102

Project Introduction

Modern variants of proven, classical R2R coating technologies, as well as new coating methods, are needed for enabling widespread commercialization of renewable energy storage and conversion technologies. Established coating methods, such as multilayer slot-die, gravure, reverse comma, tape casting, etc. with homogeneity and uniformity superior to spraying methods need to be further adapted for improving performance of various technologies. The shape, size, and morphology of the materials, the chemistry of the formulation, the nature of slurries, their coating rate, the rate of drying etc. all play a role in determining the final coating architecture, quality, and performance. In addition, NDE of the produced coatings for improving in-line QC and identification of defects, prior to down-stream value added steps being performed, is of paramount importance.

More early-stage research is required to solve the challenge of linking particles used in material formulations to the performance of the final R2R product, especially for a process that uses multiple layers of deposition to achieve the end product. This activity brought together expertise from five national laboratories to understand the complex nature of the R2R process and develop methods to improve existing production capabilities.

Objectives

The overall objective of this collaborative effort is to advance technologies applicable to continuous manufacturing to reduce cost, increase precision, and enable in-line QC and defect detection that will result in expanded use of R2R processing to produce clean energy technologies. Modeling and simulation of the materials and processes being developed will be used to understand the fundamental physics and particle interactions of those materials as they relate to the manufacturing process on both a macroscopic scale and a continuum scale.

A specific objective is to develop methodologies for multilayer coatings, including those achieved by a single layer (or single process) construction, with the same performance as structures fabricated in multiple process steps, thus reducing the number of process steps and reducing manufacturing cost. Another objective is to advance ES and casting technologies to enable functional multilayer coating approaches for a variety of applications. Metrology and analytic tools and methods will be developed to further enable identification of process defects and impacts on a real-time basis. The sum of these efforts that are applicable to flow batteries for grid applications, filtration applications, electrochemical applications, fuel cell and electrolysis membranes, catalysts free of Pt group metals, electrodes for electrochemical carbon dioxide reduction concepts, water manufacturing, and others will serve to advance the state-of-the-art processing science related to these technologies.

Approach

Core Program

This early stage research and development project on R2R advanced technologies in a national multi-lab collaboration will deliver advances in the fundamental understanding of R2R processing on moving webs, carriers, or other substrates and develop tools, metrology approaches, processes, and new materials to improve yields, overall quality, processing rates and reduce cost. It will overcome the lack of scalability and understanding of fundamental chemistry and materials properties demonstrated on selected key technology applications with cross-cutting impacts. The collaboration will explore and execute new methods to engage with industry and other R2R stakeholders that will enable pre-commercial, low technology readiness level activities.

Technology focus will be on the process science of multilayered coating deposition and drying and curing, its associated fundamental kinetics, modeling and simulation, and metrology to understand quality and defects. An advanced mathematical modeling approach will be implemented where LBNL develops particle-scale colloidal and slurry optimization models that enables understanding of particle effects on mixing. This information will be subsequently provided to SNL for developing more accurate rheology constitutive relationships for the continuum-scale coating deposition and drying models. In turn, this latter information will be provided to LBNL for developing models for wet coating consolidation and drying processes. ORNL, ANL, and NREL will support the overall three-phase modeling effort by providing experimental data for materials, components, processing parameters, and devices.

Novel R2R Deposition System Based on ES Technology and Advanced/In Situ Characterization and Testing (ANL Lead Laboratory)

ANL will perform tasks in coordination with ORNL, LBNL, NREL, and SNL, with a focus on the development of a novel R2R deposition system based on ES technology, as well as advanced and in-situ characterization and testing capabilities. Materials developed through this pathway are applicable to fuel cell/electrolysis, air and water filtration/purification, solid-state battery electrolytes, organic PVs, and CO₂ separation/reduction when integrated with multilayer coating techniques. The development of this highly versatile deposition process will enable significantly improved productivity and device quality (as compared to conventional deposition methods) for a wide range of high performance applications. In addition to toolsets, ANL will also develop recipes and processing parameters that are suitable for high throughput R2R ES processes. ANL will also collaborate with ORNL and NREL to develop innovative nanofiber material systems as an effort to demonstrate the benefit of R2R ES manufacturing. Three model material systems will be developed under this context.

ANL will also support NREL's in-situ metrology development by providing electrospun fiber mats of different materials, thicknesses, and fiber morphologies for NREL to perform characterization tool design and testing. In addition, ANL will contribute to modeling and simulation work related to inks and multilayer coatings by providing ink data to partner labs to enable theoretical studies of correlations between ink compositional properties (e.g., ingredients, solvents, viscosity) and ink flow, deformation, and drying behavior.

Advanced and in situ testing and characterization of prototype components and devices will be a collaborative effort between ANL, ORNL, and NREL and will focus on fabricating components and devices prevalent within water, fuel cell, and energy storage applications. ANL will provide nanofiber materials, ink solutions, and solvents for distribution to the other laboratory partners for slurry and multilayer composite membrane synthesis and testing. Advanced ink and electrode characterization will focus on obtaining ink and electrode microscopic and tomographic properties using high-resolution synchrotron-based diffraction and imaging techniques, to enable a more in-depth understanding of structure properties of multilayer coatings. ANL will conduct ultra-small-angle X-ray scattering (USAXS), SAXS and X-ray computed tomography (XCT) studies of the ink and electrodes provided by ORNL and NREL.

Colloidal Chemistry, Surfactant Research, Slurry Processing, Deposition and Drying/Curing Methods (ORNL Lead Laboratory)

ORNL will utilize materials provided by ANL and other collaboration partners and provide R2R processed materials to ANL and NREL for characterization. ORNL will also work with SNL on advanced modeling and simulation and processing science for special coating operations such as slot die. ORNL will work with LBNL to provide data for modeling and simulation of the drying behavior with a special focus on interfaces and solvent/curing agent behavior and relevant defect structures. LBNL staff will spend research time at ORNL to

understand processing science with hands-on experiments and enable a close integration of modeling and simulation into the results guiding the experiments.

Materials will be received from other project partners and integrated into a fully-controlled and optimized multilayer coating operation. Slurry processing efforts will focus on understanding particle interactions, receiving experimental guidance from the modeling and simulation tasks at LBNL and SNL, measuring zeta-potential of individual slurry constituents, optimizing multi-component mixing and long-term stabilization of slurries. Advanced characterization methods such as transmission electron microscopy (TEM) and X-ray photoelectron spectroscopy (XPS) will be utilized to determine the material properties.

Optimized slurries in single and multi-slurry systems will be deposited in multiple steps and single steps (dry on wet and wet on wet) to create multilayer coatings. During drying and curing operations, phase separations and phase intermixing phenomena will be studied and resulting interfacial behavior and their effects on functional properties will be determined and optimized. This methodology will be conducted in close collaboration with the modeling and simulation tasks at LBNL and SNL. Coated materials will also be distributed to the other laboratory partners to study defect structures and functional device performance.

To support R2R ES platform development by ANL, ORNL will provide lab-scale support of collaboration advancements in the fundamental understanding of R2R processing on moving webs, carriers, and other substrates. ORNL will assist in development of tools, metrology approaches, processes, and new materials to improve yields, overall quality, processing rates, while also reducing cost. Benchtop experiments will be performed that are aimed at overcoming the lack of scalability and understanding of fundamental chemistry and materials properties demonstrated on multiple selected key applications with cross-cutting benefits and impacts.

Physics and Methodologies for Multilayer Coatings/Deposition; Fabrication and In Situ Testing of Prototype Components and Devices; and Novel Non-Destructive Evaluation, Quality Control and Metrology (NREL Lead Laboratory)

The NREL effort for multilayer coatings and deposition will focus on the physics, methodologies, and equipment for multilayer coatings, which are applicable across a vast range of materials, including functionalized membranes and porous media, ion transport media, catalytic membranes, water filtration and purification media, electrochemical active layers, and opto-electronic films. Multilayer structures can be implemented in various forms, including being coated or deposited in simultaneous but discrete layers, or by being coated in a single layer but taking advantage of consolidation physics to stratify individual constituents. A particular focus will be exploration of multilayer coating technologies that generally are not or have not been applied to these applications, but may provide great improvements in throughput, energy consumption, or quality, and could lead to novel structures. Examples are slide coating and ES. In support of a process-focused study, detailed exploration of particle-polymer-solvent interactions in the subject inks and slurries will be undertaken, with advanced characterization, modeling and/or visualization support from other labs. It is expected that close coordination with SNL and LBNL on slurry, coating and drying modeling will be pursued to achieve fundamental understandings of these processes and materials. Small-scale ES fabrication capabilities will be leveraged to pursue basic process understandings for the ES process, including the development of detailed process windows. NREL will collaborate with ANL to explore scale-up of ES formulations at ANL's R2R ES facility.

Fabrication and in-situ testing of prototype components and devices, representative of potential commercial products, is critical to understand the impact of novel R2R processing techniques on new material

technologies. NREL will bring to bear a wide range of application-specific device fabrication and testing capabilities to support the breadth of material technologies within the multi-lab collaboration.

Real-time in-line and in-process measurement techniques for NDE, QC and metrology are a ubiquitous and cross-cutting need for novel R2R materials, as identified in the AMO MYPP. In close coordination with industry and Collaboration partners, NREL will develop and demonstrate real-time inspection techniques that are broadly applicable. A particular focus of this effort at NREL will be thermal and multispectral imaging techniques to measure material properties or detect defects in multilayer structures. This work will leverage existing thermographic, optical, electro-optical, and fluorescence test-beds, at various scales, and a full-scale industrial web-line, in order to explore excitation physics, impact of material motion, and optimization of sensitivity and resolution, as well as to demonstrate methods on the web-line using sheet or roll materials from industry or fabricated at NREL or partner labs.

Macroscopic Mathematical Model of the Drying of a Single Layer Generic Slurry Containing Monodispersed Colloidal Particles, Binder and Solvent (LBNL Lead Laboratory)

LBNL will produce mathematical models of component association and aggregation in mixing and for drying and consolidation of dispersion coatings. As the component interactions and their effects on macroscopic behavior for these concentrated dispersions of interest are poorly understood, LBNL will design and execute novel experiments needed to provide the necessary physical insight into these processes. These experiments will include computer-controlled mixing and monitoring of component sizes, as well as computer-controlled drying of cast dispersion films.

The modeling approach for drying of multilayer coatings will consider the selection and processing affect for the arrangement and interaction of dispersion components, how the dispersion formulation and processing affect the dynamics of film drying, and the component interactions that determine the final product quality. Models for the drying of coatings will ultimately address the following factors: (1) the dispersion composition including preparation of components, (2) component mixing order (potentially mixing conditions, mixing times, mixing rates, temperatures, disperser tool geometry, container geometry and positioning or movement of disperser tool in container, etc.), (3) coating conditions (potentially dispersion handling, thickness, deposition mechanism and rate, number of layers, layer composition, and substrate) and (4) drying conditions (potentially atmosphere, heating mechanisms, heating rate, and drying times).

Validated Continuum-Scale Models to Accelerate Design and Scale-up of Simultaneous Die Coating Process Technology (SNL Lead Laboratory)

Continuous liquid film coating process technology is one manufacturing sector that has arguably benefitted the most from continuum scale models of the underpinning capillary hydrodynamics of deposition and subsequent drying/solidification. SNL will focus on building and validating continuum-scale models that support the R2R Collaboration multi-laboratory effort to accelerate design and scale-up of coating process technology underpinning target applications, with a specific focus on simultaneous multilayer coating die/process technology in FY 2019. Model development will also be aimed at drying and solidification of multiple layers, simultaneously, so as to understand the underpinning mechanisms of defect formation and prevention.

SNL will coordinate with ORNL (for processing and characterization), LBNL (for materials/microstructure modeling), and will leverage existing NREL test-beds, platforms and capabilities in solution processing, R2R processing, and metrology. The aim of the coordinated activities will be model validation (including the

sensitivity analysis of the most relevant coating and drying success/failure factors, e.g. rheology, particulate uniformity and microstructure, wettability and hydrodynamic defect detection at process-envelope boundaries.

The focus will be to develop continuum finite element coating and drying process models of sufficient fidelity to address the range of materials and breadth of processing routes of the collaboration. In these models, material variability manifests in the chosen rheological constitutive relationships, capillary wetting models (static and dynamic), process-model boundary conditions, and composition/microstructural representations during solidification. As such, close collaboration with the other laboratories for ink/solution characterization and metrology will be maintained. Extra focus will be on multilayer coating systems, and model fidelity will be sufficient to capture layer-to-layer stability, process operating window defined by boundaries of hydrodynamic defect formation and drying/solidification defect rate-processes (drying, curing, fluid flow). All these aspects will be examined with varying ink/solution rheology (purely viscous behavior and viscoelastic behavior), process parameters (die-lip/face geometry), wetting/surface energies of die/substrate, and other factors as defined by the collaboration's examples.

FY 2020 Plans

Core Projects

The core program tasks that were initiated in FY 2019 will continue by conducting further research on some of the work completed. ANL will perform battery and fuel cell nanofiber property optimization through characterization of material concentration, doping effect, and thermal treatment conditions such as polymer calcination, metal ion oxidation, phase formation and transformation, and microstructure change. Nanofiber material property optimization will be obtained through in-situ characterization at the ANL APS, which conduct simultaneous structural and chemical analysis during nanofiber annealing and calcination. A new nanofiber-based ion-exchange membrane will be developed using a co-electrospinning method to address the issues of functional moiety aggregation and poor membrane porosity control associated with the current electrodeionization membranes.

ORNL will perform relevant ink studies, e.g. rheology, surface tension, and zeta potential to support multi-layer coating of PEMFC electrodes with bilayer cathodes (produced with dual slot-die coating). Studies will be performed on GDE coatings for photoelectrochemical hydrogen production.

Coordination with ORNL, LBNL, and NREL on ink modeling to enable simultaneous multi-layer coating will provide data and contribute to model validation. ORNL will continue to collaborate with ANL on USAXS and complete the small-angle neutron scattering ink study. General purpose SANS experiments at ORNL on cathode ink colloidal stability will be completed. Simultaneous multi-layer coating studies will be performed with different particle sizes and pore-size distributions exploring coating physics and parametric effects. ORNL will continue to coordinate (provide data and contribute to model validation) with SNL and NREL on multi-layer coating modeling to understand flow interaction of multiple simultaneous wet ink layers, and collaboration will continue between ORNL and ANL on X-ray computed tomography as well as completing TEM at ORNL for morphology of coated functional layers. Detailed drying protocol studies will be performed with the 9-zone (infrared and convective air) ORNL drying oven and the two-stage NREL drying oven as a function of line speed and temperature ramping to address applications for PEMFC cathodes and PEM electrodes.

NREL will pursue widely applicable multi-layer coating development and process window understandings, in coordination with ORNL, with a focus on slide die coating. NREL will continue to receive coated samples from ORNL and, with these materials as well as materials coated at NREL, will fabricate cells and perform in

situ device testing as necessary to understand the impact of ink and process parameters on performance. Coordination will continue with LBNL and SNL on the development of particle- and continuum-scale models for these inks and coatings. NREL will perform small-scale ES processing studies, and coordinate with ANL on exploration of R2R ES of target formulations. Metrology development for further process efficiency improvement and in-line material and device manufacturing that leads to further improvement in scalability and efficiency will continue. Development of multi-layer membrane thickness imaging diagnostics will continue and scoping work for a multi-layer functional layer (i.e. heterogeneous, non-transparent layers where optical interference is not likely measurable) diagnostic, e.g. for ES/porous structures, will begin.

LBNL's initial model development work in FY 2019 for drying coatings suggested that there is a deep lack of understanding about the physics for the concentrated dispersion systems that are the focus of this Collaboration's efforts. For this reason, LBNL has proposed to design and construct novel setups for experiments that will provide needed insight into dispersion mixing and drying, which LBNL will later summarize in the form of mathematical models, as previously planned. While models for specific experimental samples will be developed, LBNL's efforts are meant more generally to develop a methodology for taking experimental observations and subsequently creating models for new dispersion compositions. Experiments will start in FY 2020 with a focus on component-level interactions and future work will combine sample processing and coating drying setups in conjunction with a range of analytical tools.

Component-level interactions will be initially explored in dilute mixtures by combining customized computer-controlled mixers, a computer-controlled pump, custom control software, a temperature bath, and a particle size analyzer for rapid measurements of particle size distribution evolution. By varying mixing and pumping parameters as well as dispersion composition, LBNL seeks to estimate component association strength and agglomeration rates. This information might be supplemented by similar experiments using techniques such as Fourier-transform infrared or Raman spectroscopy that are expected to show the degree of polymer adsorption, possibly in more concentrated dispersions. LBNL then expects to summarize this component interaction information in the form of a mathematical model of mixing.

The experimental setup for coating and drying is planned to mimic the R2R environment, but with small samples, allowing the setup to be readily combined with various analytical tools; for example, it will be portable for transport between the laboratory and the LBNL ALS. An enclosed coating and drying "table" with a controllable atmosphere will be fabricated. Initial plans are to perform experiments for doctor blading and possibly spray coating. The setup will be designed for rapid restoration of the initial state for subsequent experiments. Outside of the ALS, cameras and/or a profilometer will be used to monitor drying film height. Computer control of substrate tension, coating, and heating should also aid in reproducibility. Experimental inputs and outputs will be used to guide development of LBNL's drying coating models. As remote control will be necessary for work in ALS hutches, which is expected to initially be most readily performed for battery materials, these functions are being implemented by leveraging funding from the DOE Vehicle Technologies office. Experiments at the ALS could include X-ray diffraction (XRD) to monitor polymer crystallization during film drying and/or X-ray radiography/tomography to monitor spatial distribution of high-Z material.

SNL will complete a three-layer test case for the NREL slide-coating trials on membrane electrode assembly candidate constructions. This will require working closely with the NREL team to determine factor space of options and reduce the number of trials. Limits of operability with respect to a select parameter set will be determined and a complete user-interface will demonstrate following features: parameterization – web-speed, slide angle, layer(s) film thicknesses, vacuum pressure, rheology/layer selection, user-specified parameter continuations, continuously updated visual of finite element model mesh for indications of mesh distortion, and automated remeshing and remapping. SNL will also complete and validate a single-, two-, and three-layer drying model accounting for binder, solvent, and active particulate component from the polymer electrolyte membrane (PEM) exemplar. The hope is that proper instrumentation can be added to NREL and ORNL

drying ovens to help with validation of the model (temperature vs. time in the coating, etc.). At a minimum, the planned work from the drying table being developed at LBNL with SNL-assistance will be used for validation.

Other Collaboration efforts may include expanded predictive modeling and simulation, advanced flexible electronics and opto-electronics, and advanced CO₂ conversion electrodes. The Collaboration laboratories will coordinate to define and develop an industry stakeholder council (or similar activity approved by AMO) to include companies such as Saint-Gobain, FLEXcon, and Eastman Kodak as examples. The goal is to organize and hold an R2R stakeholder technical meeting to gather information on current R2R technology needs and barriers in the areas of study of the multi-lab collaboration.

CRADA projects

Efforts for the CRADA projects with agreements negotiated in FY 2018 continued through FY 2019 to meet contractual and programmatic requirements. This includes the following efforts:

- Fisker, Inc. - Fisker, Inc. partnered with LBNL and ORNL to demonstrate all-solid-state batteries based on LLZO separators and cathode scaffolds that will allow scaling a freeze casting process to the pilot level at ORNL. This project completed in May 2019.
- Navitas Systems, Inc. - Navitas Systems, Inc. partnered with ORNL and NREL to demonstrate R2R production of an advanced separator for lithium ion batteries.
- SolarWindow Technologies, Inc. – SolarWindow Technologies, Inc. partnered with NREL and ANL to demonstrate diffractive multiplexing for high-throughput R2R laser patterning of flexible organic PV modules.
- Nel Hydrogen/Proton OnSite - Proton OnSite will partner with NREL, ORNL and ANL to research R2R manufacturing of advanced (low loading, direct coated onto membrane) electrolysis anodes for low-cost hydrogen production. This project remained in the approval process at the end of FY 2019. The project is expected to start early in FY 2020.

Potential New Efforts

ANL ES

- R2R demonstration of ES recipes developed by ORNL and NREL
- Tool development for process efficiency improvement: in-line ES and annealing
- Demonstrate devices for battery, fuel cell, and ion-exchange membrane applications
- Perform in-situ APS experiments to accelerate material and process optimization
- Feasibility study on R2R printed electronics

NREL Multilayer Coatings

- Understand the miscibility of adjacent layers in multi-layer coatings during coating and drying
- Determine the impact of interfacial tension
- Determine the impact of particle size, viscosity, drying time, etc. on interlayer diffusion during drying
- Determine the impact of relative volatility of solvents between adjacent layers
- Study the effects of shear rate and time of deformation during coating on resulting microstructure in weakly agglomerated systems
- Evaluate the possible range of thicknesses for two-layer and three-layer slide die coatings based on die design and flow conditions

- Model interparticle interactions and resulting macro properties (e.g. rheology) in inks, based on constituent properties
- Demonstrate novel multi-layer structures in specific applications that have the same or improved performance and reduced manufacturing cost by reducing process steps, CAPEX, energy consumption, floor space

Technology Transfer Paths

For the core program tasks, technology will be transferred through collaboration with industry and companies with CRADA contracts and the DOE team will work closely with any companies to ensure technologies are accepted for commercialization. Various aspects of the R2R AMM program were presented at conferences, symposia, peer reviews and during direct contact with industry and the commercial sector. Specific research was reported in technical journals and through patent applications.

The models and simulations will be extended to encompass not only materials discovery, but also to accelerate materials synthesis and fabrication applicable to industry. This effort leverages the R2R processes and technologies at ORNL, the engineering expertise and research facilities such as the APS and the Materials Engineering Research Facility (MERF) at ANL, and the metrology, R2R processing, and device fabrication and testing capabilities at NREL, in conjunction with the materials design computational efforts of SNL and LBNL. SNL will also conduct training courses for the modeling and simulation tools that will be open to industry, national lab, and academic partners.

Results

Novel R2R Deposition System Based on ES Technology and Advanced/In Situ Characterization and Testing (ANL Lead Laboratory)

R2R ES Platform Development

The overall goal is to develop a R2R ES platform that is applicable to a truly vast range of materials, such as functionalized membranes and ion transport media for fabrication of water filtration membranes, fuel cell membranes, and battery electrodes. One of the subtasks was the identification of the best-of-practice R2R modules and its configuration relative to the ES modules.

Comparative studies of various R2R configurations and designs were conducted, with the focus on the positions of the R2R modules relative to the ES modules. Two popular configurations were investigated. One is bottom-up spinning as illustrated in Figure 2 (a) and the other is top-down spinning as illustrated in Figure 2 (b). With the bottom-up spinning, the moving substrate (R2R module) is facing down to the spinnerets; therefore, the microjets and in turn nanofibers generated from the spinning process are projected upward from the spinnerets towards the substrate. Hence, droplets from the needle tips will not contaminate the nanofiber products. On the other hand, with a top-down spinning geometry, the precursor droplets at the spinneret tip can fall down to the existing nanofibers, damaging nanofiber structures. Based on the above consideration, bottom-up configuration was selected for R2R ES development.

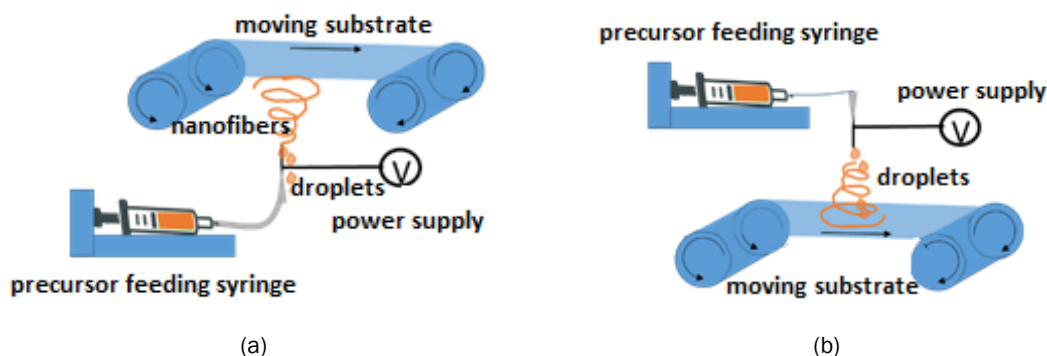


Figure 2 ES configurations of (a) bottom-up spinning where nanofibers are projected upward and (b) top-down spinning where droplets fall onto the already-made nanofiber products under gravity. Source: ANL

The ES R2R module with down-facing web, wind-unwind system, and 56 needle spinnerets shown in Figure 3 was implemented at the ANL MERF. The web size can reach 0.55 m x 30 m (width x length). In addition to forward moving, the web also does a rocking motion, which improves the fiber spatial distribution on the web. Simultaneous spinning of PVDF nanofibers by 56 needle spinnerets on the moving web was demonstrated to validate the R2R function of the module.

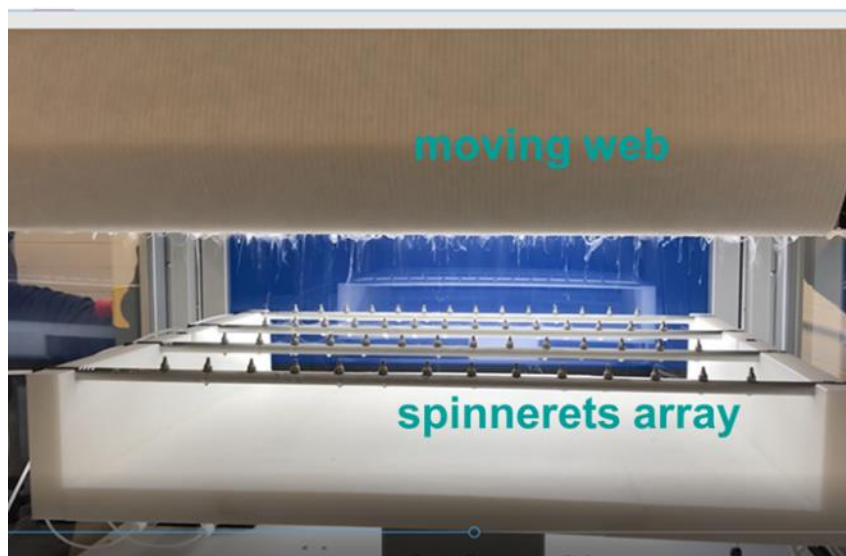


Figure 3 A picture of the ES process for the R2R ES system implemented at the ANL MERF, which shows simultaneous fiber deposition from 56 needles on a moving web. Source: ANL

Efforts continued for transfer the lab-scale ES recipes to the R2R module and demonstrate scalable nanofiber and membrane fabrication by R2R ES. Because of the different configurations between the lab-scale and the R2R ES equipment, differences in operational conditions for the two systems were expected. Thus, operation parameter optimization for the R2R process was necessary. This was addressed by R2R fabrication of LLZO nanofibers where changes were made to the precursor solution formulation and the ES tool operation conditions. During this demonstration, a new co-solvent system which facilitated more rapid evaporation was developed. In lab-scale spinning of LLZO precursor fibers, N,N-dimethylformamide (DMF) and glacial acetic acid were used as solvents. For R2R ES of LLZO, isopropyl alcohol (IPA) was added to the DMF-acetic acid solutions to increase the solvent evaporation rate. IPA to DMF-acetic acid ratios of 0-45 wt% were examined. In general, the fibers produced from precursors containing IPA displayed more desirable fiber morphologies at a wide range of conditions over those that contained only DMF and glacial acetic acid. As shown in Figure 4, the diameter of the fibers increased significantly with the IPA weight percentage (and thus evaporation rate of solvent) until the IPA amount reached 45 wt% where electrospun ribbons instead of fibers were obtained.

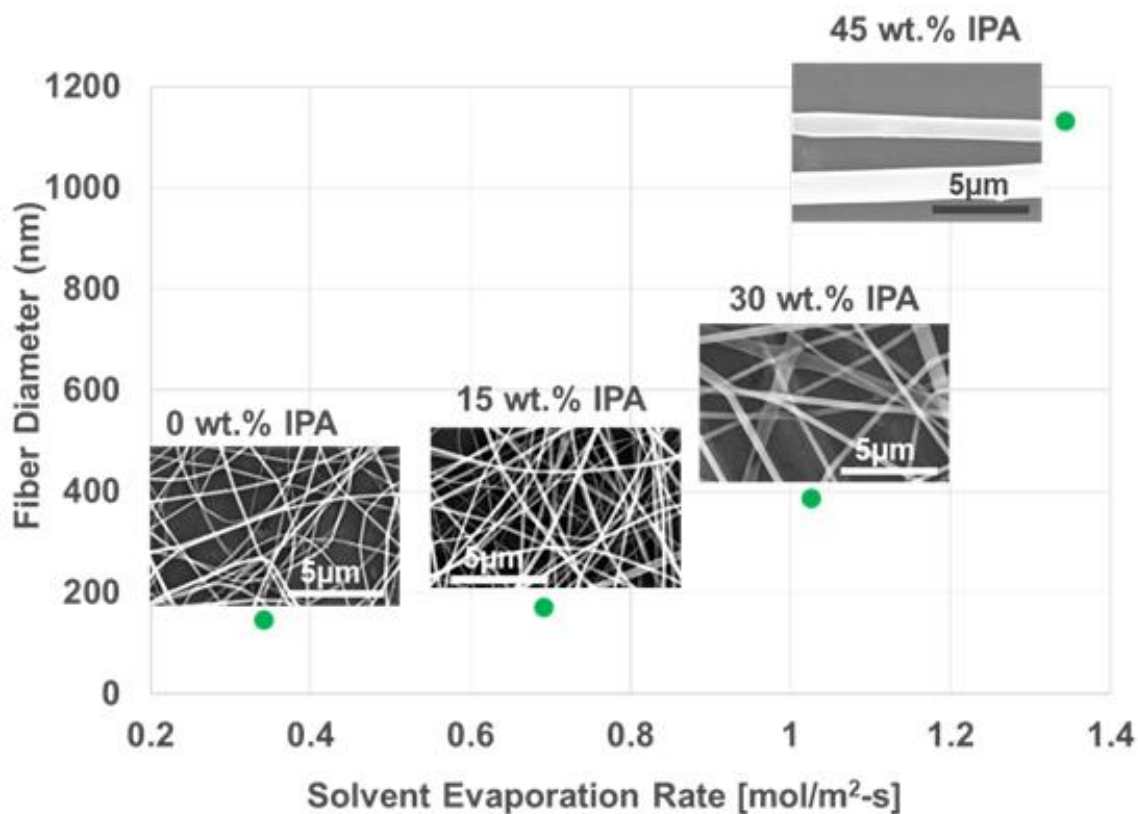


Figure 4 Fiber diameter as a function of evaporation rate for different concentrations of IPA in solution. Source: ANL

In addition to solvent evaporation rate, optimization of the solvent viscosity, ES voltage, and the spinneret-web distance was performed using the Design of Experiment depicted in Figure 5. The optimized recipe was produced at scale as shown in Figure 6 to validate R2R ES production of electrospun battery materials.

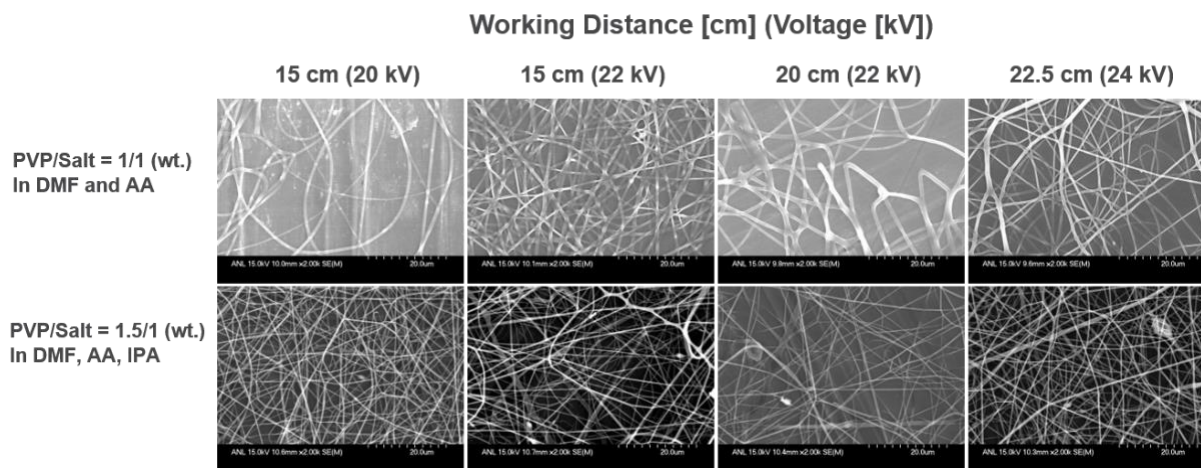


Figure 5 Comparison of fibers produced from precursors with and without IPA at different voltages and working distances for R2R ES process optimization. Source: ANL

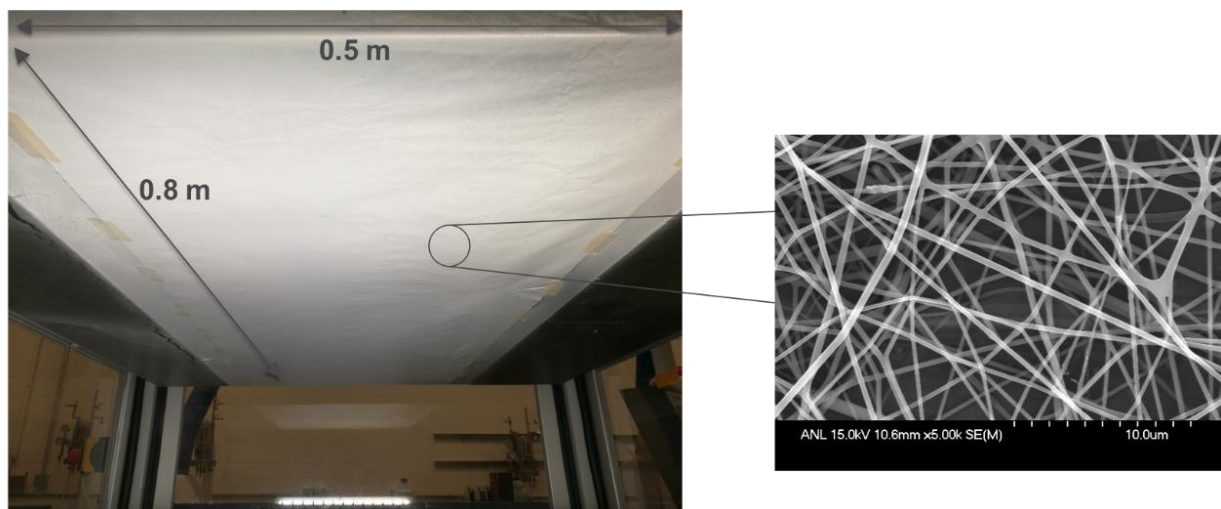


Figure 6 LLZO precursor nanofibers deposited on an aluminum web at scale using R2R ES module. Source: ANL

Advanced Materials and ES Recipe Development

Design work to develop material systems and ES processes for fabrication of battery electrolyte and fuel cell electrodes was performed collaboratively amongst ANL, ORNL, and NREL on the existing in-house benchtop ES tools. Based on discussion by each lab's teams, ANL and ORNL teams focused on advanced materials and recipes applicable to ES processes for solid lithium battery applications. Both teams developed the same electrolyte materials with each team optimizing a different set of process parameters to accelerate the development process. ANL and NREL teams developed fuel cell materials where the ANL team focused on solid oxide fuel cell applications while the NREL team focused on low-temperature polymer fuel cell applications. The two teams shared the results regularly throughout the development process. These efforts can expand the application domains of ES fuel cell materials.

ANL chose LLZO and LSCF as the representative battery and oxide fuel cell materials, respectively. ES recipes of LLZO and LSCF were developed through several iterations of ES experiments. For the LLZO, process optimization was performed to improve nanofiber quality, such as morphology and diameter distribution. Figure 7 shows an example of ES process optimization for LLZO precursor nanofiber from scanning electron microscope (SEM) images. The influence of applied voltage on the nanofiber morphology was clearly observed – higher voltage leading to larger nanofiber diameter distribution.

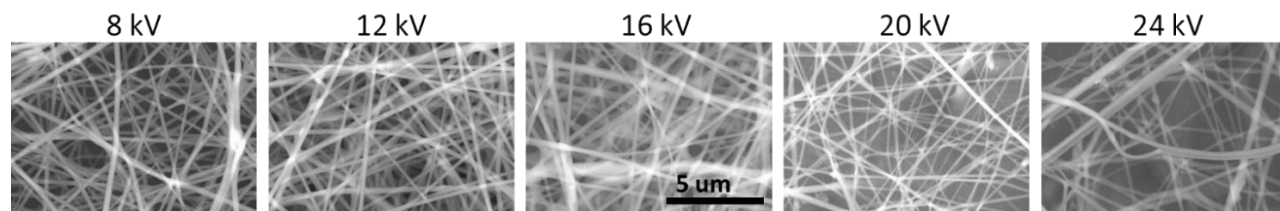


Figure 7 SEM images of the as-spun LLZO polymer precursor nanofibers that were synthesized under the different voltages shown. Source: ANL

Other fabrication parameters, such as working distance and precursor solution viscosity, were also examined to achieve feasible process window. Figure 8 shows an SEM image of LLZO fibers after optimization. Average fiber diameters of 220 nm were observed with a narrow diameter distribution of 12%.

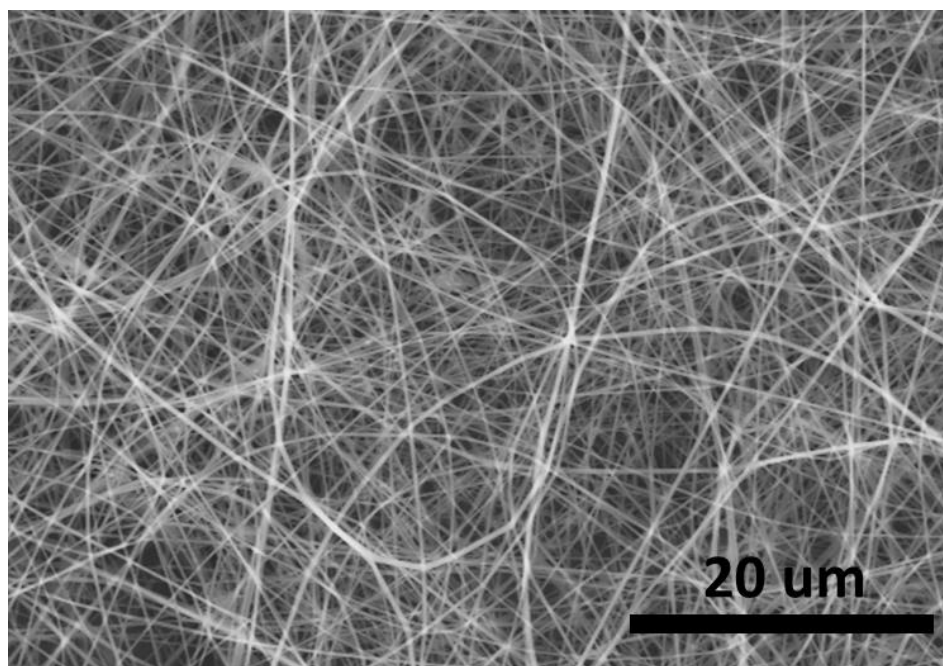


Figure 8 SEM images of as-spun LLZO polymer precursor nanofibers fabricated with optimum ES conditions. Source: ANL

Similarly, ES recipe and process development for LSCF were performed. Figure 9 shows the SEM images of LSCF precursor fibers synthesized at various voltages from 8 kV to 24 kV, where the 12 kV voltage provided the most uniform fiber morphologies and was considered as the optimal working voltage.

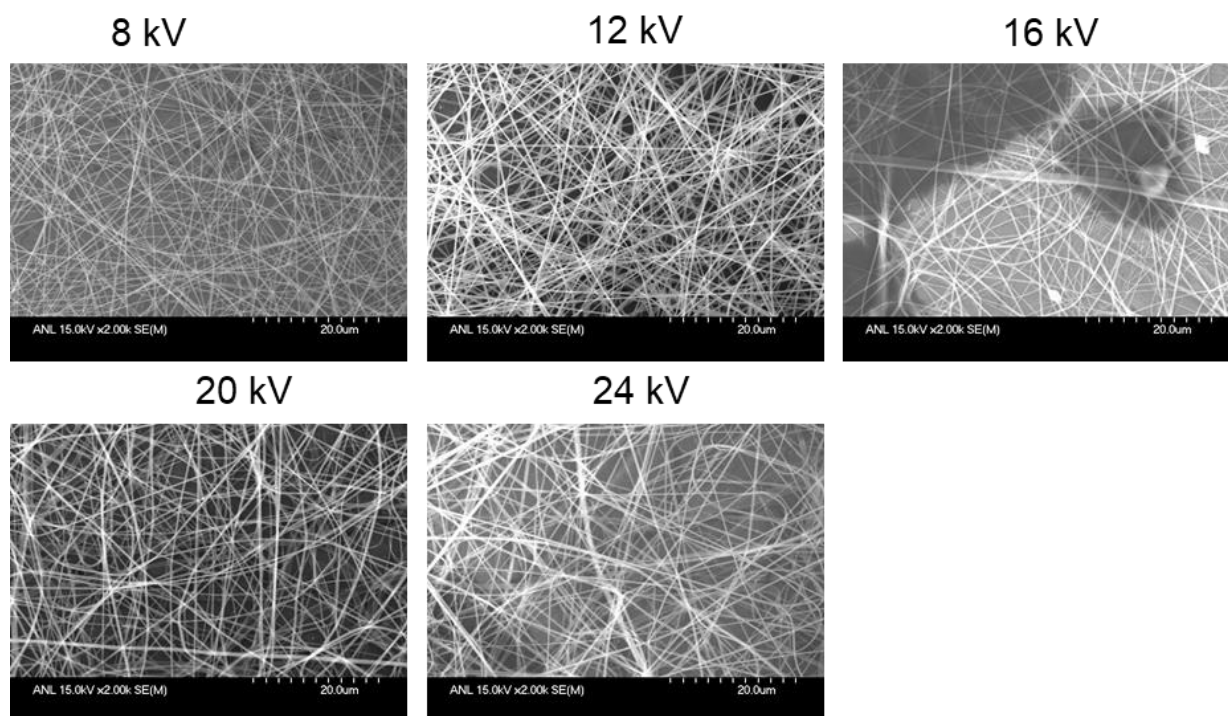


Figure 9 SEM images of LSCF precursor nanofibers fabricated at different voltages. Source: ANL

In-situ X-ray Study of the ES Process

In order to accelerate process optimization, a synchrotron-based in-situ SAXS study of ES was conducted. A compact ES unit that adapts to beamline configuration and dimensions was built and validated at the 12-ID-B beamline of the APS. Figure 10 (a) shows a photo of the ES unit mounted at the beamline station. Nanofibers that were generated at the beamline during the in-situ SAXS experiments were observed by high-resolution camera and shown in Figure 10 (b). A thin layer of electrospun fibers deposited within 30 seconds growth time were successfully detected.

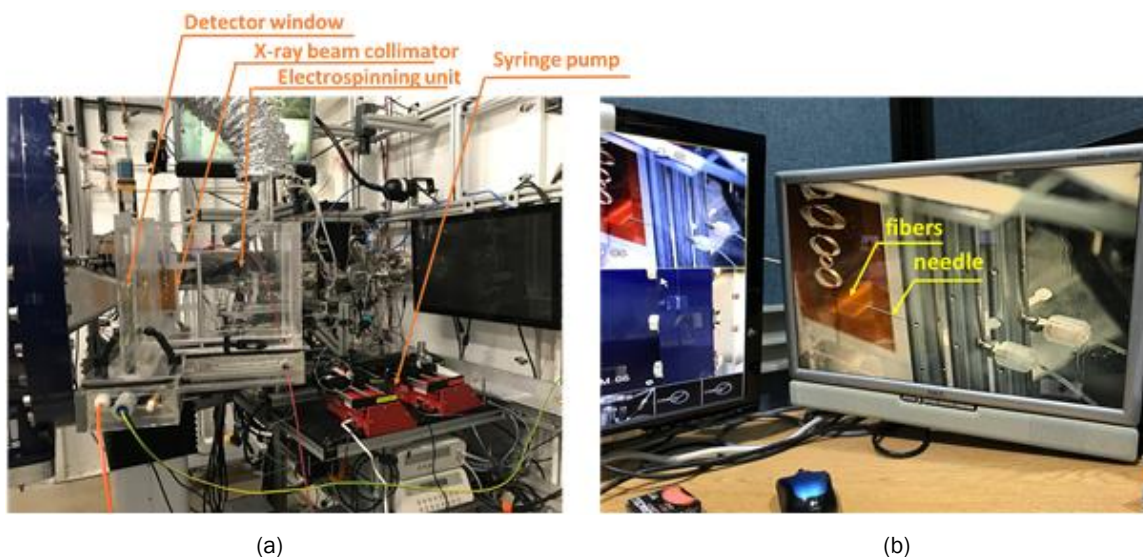
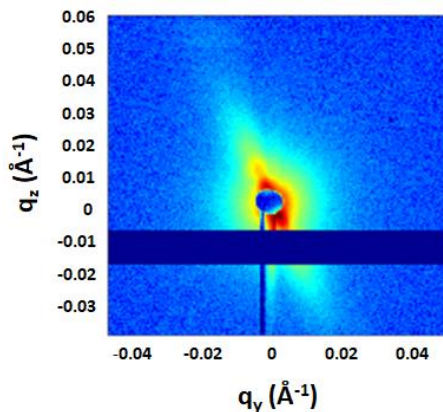
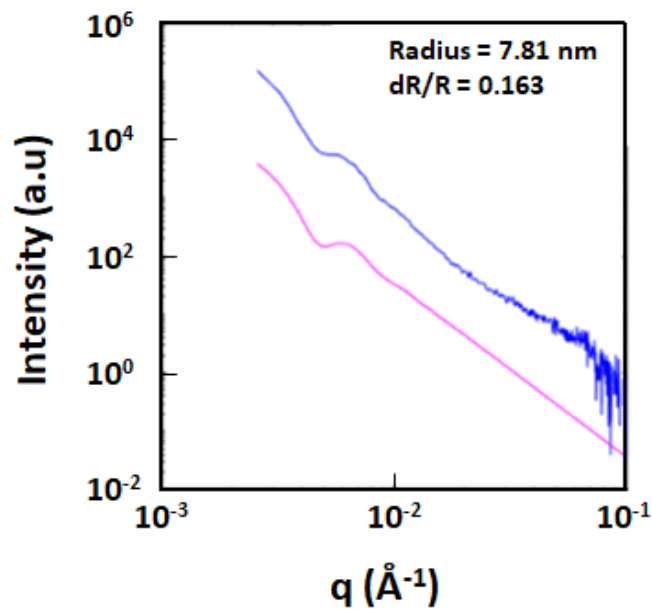


Figure 10 (a) ES unit mounted at 12-ID-B beamline of APS for in-situ SAXS study and (b) generation of FeNi polymer precursor nanofibers recorded by a high-resolution camera at the beamline. Source: ANL

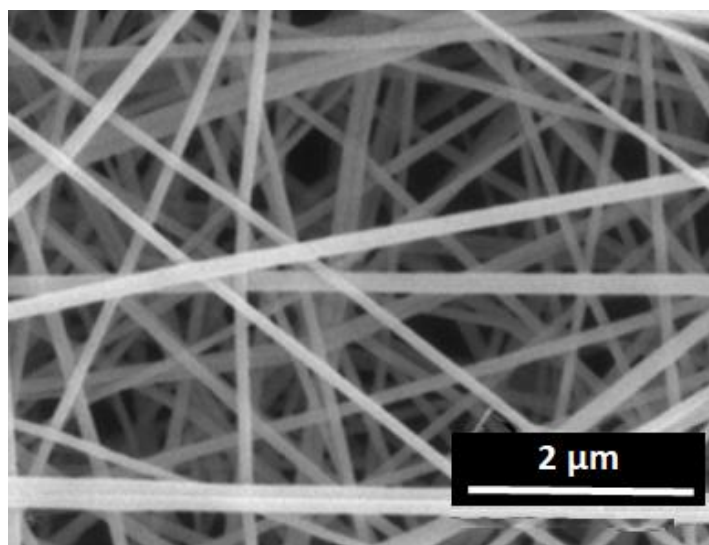
For the first APS experiment, FeNi was used as a baseline material to evaluate SAXS data quality because its ES process has been well studied by the team in the past. Figure 11 (a) shows measured SAXS data of FeNi nanofibers. Figure 11 (b) provides the simulated intensity vs. scattering vector ($I(q)$ - q) plot. The simulation matches well with the measured $I(q)$ - q plot. In addition, the average nanofiber diameter (78 nm) extracted from the $I(q)$ - q plot is consistent with what measured by SEM imaging shown in Figure 11 (c). This result indicates that SAXS is effective for electrospun nanofiber characterization. With this validation, a wide range of ES conditions related to LLZO precursor nanofiber fabrication was examined using in-situ SAXS measurements to accelerate ES process optimization.



(a)



(b)



(c)

Figure 11 (a) 2D-SAXS data of FeNi nanofibers, (b) intensity vs. scattering vector ($I(q)$ - q) plots obtained from 2D-SAXS data (blue) and simulation (purple) and (c) SEM image of the studied nanofibers. Source: ANL

Fabrication Toward Prototype Components and Devices

Post-ES thermal treatment of LLZO polymer precursor fibers was investigated in preparation for LLZO electrolyte device fabrication. A number of annealing temperatures in the range of 600-900 °C were tested to achieve desirable c-LLZO. Figure 12 shows the TEM images and X-ray profile of the LLZO fibers annealed at 700 °C. The fibers showed good crystallinity and an X-ray pattern that is consistent with that of a cubic crystal structure.

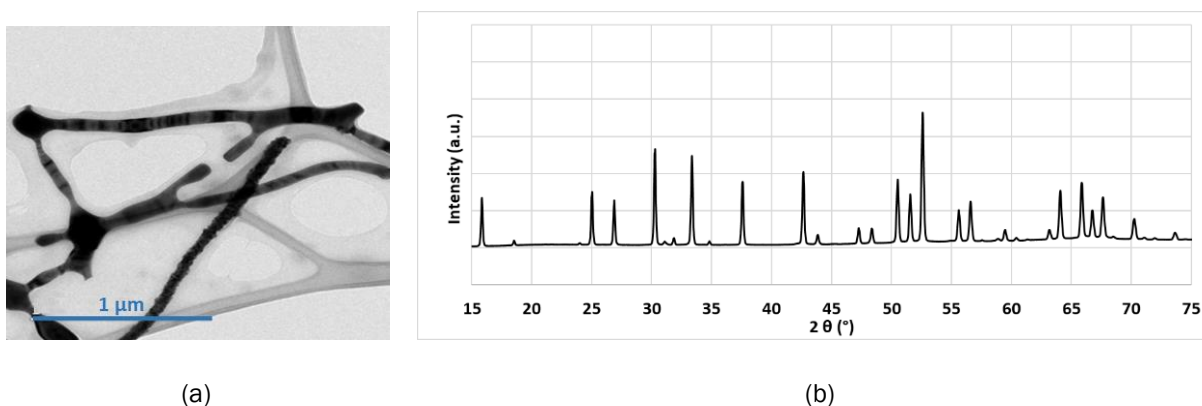


Figure 12 (a) TEM image and (b) X-ray profile of LLZO fibers after 700 °C annealing. Source: ANL

In addition to the fuel cell and battery materials, the PVDF-based polymer fibers were also developed for water filtration membrane applications. Figure 13 shows the pictures of the polymer membranes viewed from top and side.

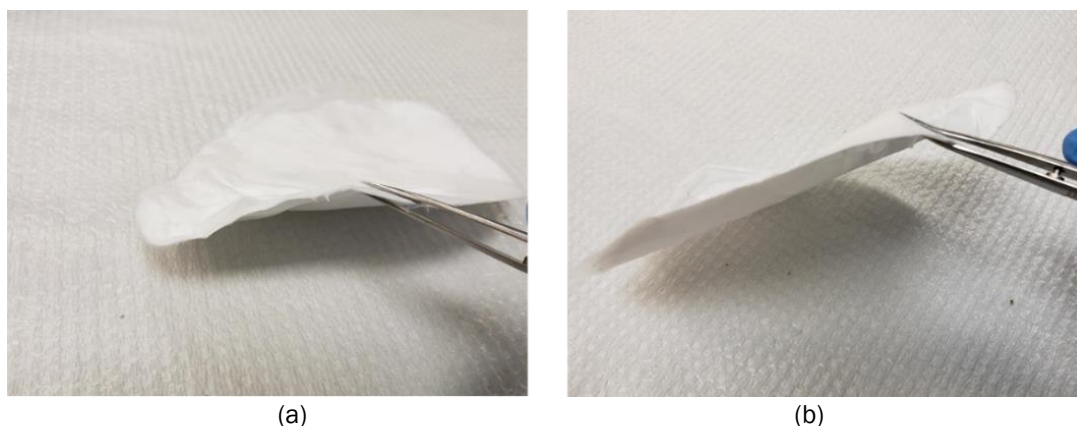


Figure 13 PVDF-based polymer nonwoven structure for water filtration membrane application viewed from (a) top and (b) side. Source: ANL

Advanced Ink and Membrane Characterization

Capabilities at ANL were used for USAXS characterizations of inks under different ultrasonic and shear mixing conditions. The overall goal was for ANL to provide support to NREL during the development of catalyst-ionomer-solvent ink compositions and processing techniques for efficient R2R fabrication of GDEs. The collaborative effort focused on optimizing cell performance and cell lifetime and minimizing ink processing time and cost by using USAXS to analyze the ink agglomerate structure during the mixing process. The specific purpose of the USAXS experiments was to study the ink microstructure evolution as a function of ink composition, ink mixing method, and time. These data complemented the rheology and performance data from NREL for inks and membrane-electrode assemblies. USAXS data was acquired and analyzed for more than 20 catalyst-ionomer inks with different dispersion formulations (25wt% IrO_x-0.2 ionomer-to-carbon ratio, ionomer only, Pt-high surface-area carbon (HSC), Pt Vulcan, etc.) and solvent compositions. A manuscript titled “The Impact of Catalyst Ink Dispersing Methodology on Fuel Cell Performance Using In-situ X-ray Scattering” was published in ACS Applied Energy Materials (see Key Publications at end of report). The formulations of all the inks studied are shown in Table I.

Table I List of USAXS-SAXS Samples

	Label	Dispersion Formulation	Solvent
1	H1	1.5wt%Pt-HSC-0 I/C (no ionomer)	10/90 nPA/H ₂ O
2	H2	1.5wt%Pt-HSC-0 I/C (no ionomer)	50/50 nPA/H ₂ O
3	H3	1.5wt%Pt-HSC-0 I/C (no ionomer)	75/25 nPA/H ₂ O
4	H4	1.5wt%Pt-HSC-0 I/C (no ionomer)	90/10 nPA/H ₂ O
5	HAI	1.5wt%Pt-HSC-0.9 I/C (PFAEM)	75/25 nPA/H ₂ O
6	HI1	1.5wt%Pt-HSC-0.9 I/C	10/90 nPA/H ₂ O
7	HI2	1.5wt%Pt-HSC-0.9 I/C	25/75 nPA/H ₂ O
8	HI3	1.5wt%Pt-HSC-0.9 I/C	50/50 nPA/H ₂ O
9	HI4	1.5wt%Pt-HSC-0.9 I/C	75/25 nPA/H ₂ O
10	HI5	1.5wt%Pt-HSC-0.9 I/C	90/10 nPA/H ₂ O
11	IR1	25wt% IrO _x -0 IC (no ionomer)	50/50 nPA/H ₂ O
12	IR2	25wt% IrO _x -0.2 I/C	50/50 nPA/H ₂ O
13	N1	2.5wt% NafionD2020 (ionomer only)	10/90 nPA/H ₂ O
14	N2	2.5wt% NafionD2020 (ionomer only)	25/75 nPA/H ₂ O
15	N3	2.5wt% NafionD2020 (ionomer only)	50/50 nPA/H ₂ O
16	N4	2.5wt% NafionD2020 (ionomer only)	75/25 nPA/H ₂ O
17	N5	2.5wt% NafionD2020 (ionomer only)	90/10 nPA/H ₂ O
18	V1	5wt%Pt-VULCAN-0 I/C (no ionomer)	10/90 nPA/H ₂ O
19	V2	5wt%Pt-VULCAN-0 I/C (no ionomer)	50/50 nPA/H ₂ O
20	V3	5wt%Pt-VULCAN-0 I/C (no ionomer)	90/10 nPA/H ₂ O
21	VI1	5wt%Pt-VULCAN-0.5 I/C	10/90 nPA/H ₂ O
22	VI2	5wt%Pt-VULCAN-0.5 I/C	25/75 nPA/H ₂ O
23	VI3	5wt%Pt-VULCAN-0.5 I/C	50/50 nPA/H ₂ O
24	VI4	5wt%Pt-VULCAN-0.5 I/C	75/25 nPA/H ₂ O
25	VI5	5wt%Pt-VULCAN-0.5 I/C	90/10 nPA/H ₂ O

Iridium oxohydroxide (IrO_x) catalyst ink studies

IrO_x catalyst inks with and without ionomer were characterized using USAXS to determine the impact of ionomer on the catalyst agglomerate size. The analysis results for the IrO_x USAXS data, using global unified fit, are shown in Figure 14. The unified fitting results for the IrO_x ink without ionomer shows a larger radius of gyration of the primary particles and a larger power law slope compared to those from the IrO_x ink with ionomer. A decrease in the power law slope is generally correlated with a lower population of agglomerates as the aggregates are uniformly distributed in the catalyst ink. This indicates that there is a reduction in the agglomerate size with the addition of ionomer, which correlates with the rheological behavior showing that the unsupported catalyst ink is stabilized against agglomeration by ionomer.

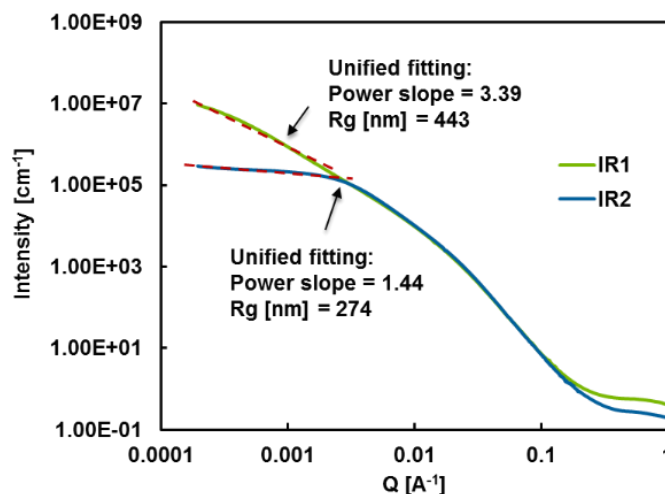
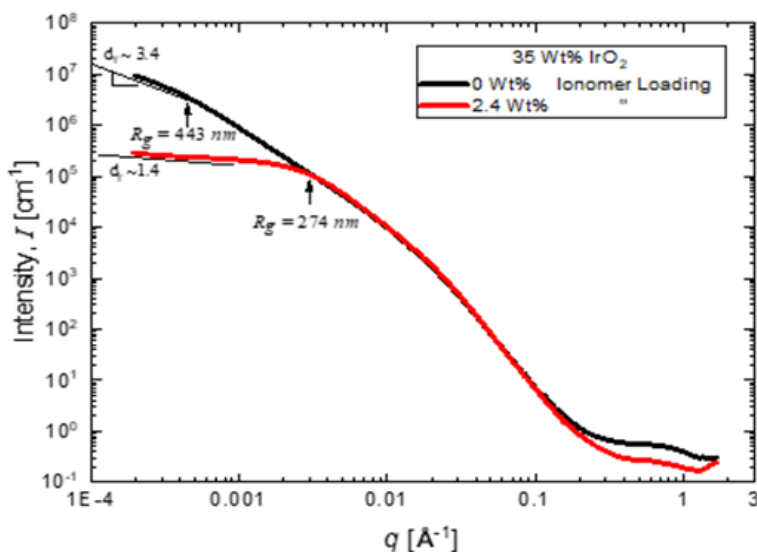
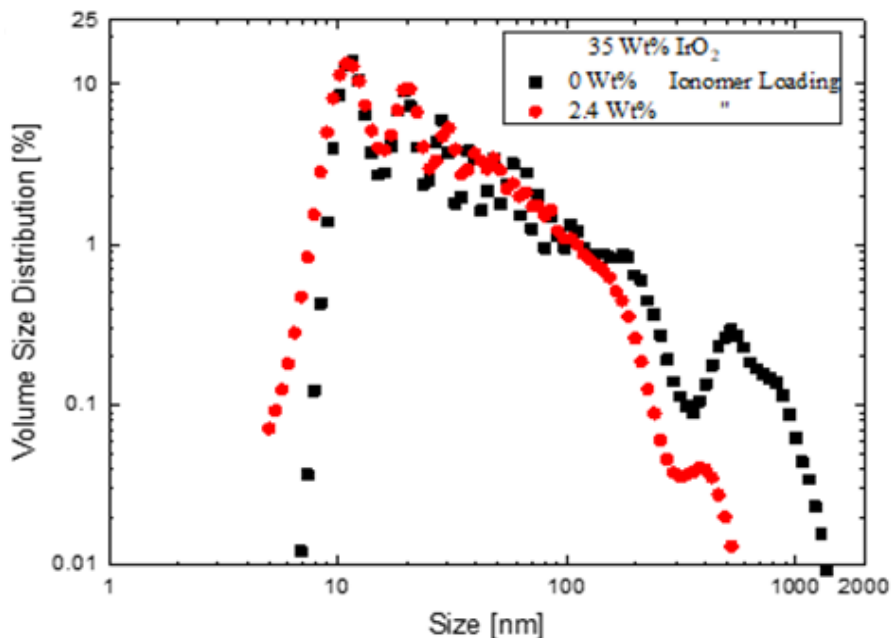


Figure 14 USAXS profiles and fitting results for IrO_x inks with and without ionomer. IR2: 25wt% IrO_x, 0.2 Ionomer/Catalyst (I/C). IR1: 25wt% IrO_x, 0 I/C. Source: ANL

The effects of ionomer loading and catalyst concentration on the microstructure of iridium oxide (IrO₂) catalyst-Nafion ionomer-solvent inks were investigated. The rheological observations were verified by zeta potential, dynamic light scattering measurements and USAXS. As shown in the USAXS data of Figure 15 (a), the low- q intensity and the fractal dimension (d_f) values are lower with ionomer ($d_f \sim 1.4$) compared to without ionomer ($d_f \sim 3.4$). The mass fractal dimension d_f from $I(q) \sim q^{-d}$ power-law fit to low- q data and the radius of gyration R_g at lower- q region from Guinier fit to the data are also shown in the plots. These data indicate a less agglomerated structure of dispersions with ionomer compared to the dispersions without ionomer. The corresponding volume size distributions are shown in Figure 15 (b). Without ionomer there is a sizeable population from 300 nm to over 1000 nm. With the addition of ionomer this population decreases substantially, with a maximum size just over 500 nm. These results corroborate the rheological analysis and indicate a reduction in the volume fraction of IrO₂ agglomerates with the addition of ionomer, which results from electro-steric stabilization of the particles.



(a)



(b)

Figure 15 (a) USAXS scattering curves for 35wt% IrO₂ dispersions both without and with ionomer (2.4 wt%) in the inks. (b) The corresponding volume size distribution of the inks without and with ionomer. Source: ANL

Pt/C catalyst ink studies

USAXS data were taken on Pt/Vulcan and Pt/HSC-ionomer-solvent inks and ionomer-solvent dispersions described in Table I. This data series investigated the effect of solvent and ionomer on the agglomerate-aggregate structure-rheology correlation for ionomer, Pt/Vulcan, and Pt/HSC inks. Figure 16 shows the USAXS scattering curves for 2.5wt% Nafion ionomer solutions that were used to investigate the effect of solvent ratio. As can be seen in Figure 16, the structure of the ionomer solution is governed by the ratio of n-propanol (nPA) and water in the solvent. The two peaks evident in the USAXS profiles generally correspond to the Teflon-like backbone matrix peaks at $>0.3 \text{ \AA}^{-1}$ knee and a sharp constructive interference peak due to the clustering/alignment of the ionomer clusters or rods at $\sim 0.03 \text{ \AA}^{-1}$. The curved region between the two peaks is associated with scattering from the individual clusters/rods. This scattering maximum is most pronounced for ionomer in high dielectric constant solvents, such as water, due to the increase in electrostatic repulsions between the ionomer clusters/rods versus lower dielectric constant solvents, such as nPA. The scattering maximum sharpens, and its intensity increases from nPA-rich to water-rich solutions, indicating an increase in association of the ionomer clusters/rods. Association or formation agglomerates of ionomer rods has been proposed to affect the ability of the ionomer to break up carbon agglomerates. A summary of the results of the fitting of the USAXS data for these dispersions is shown in Table II.

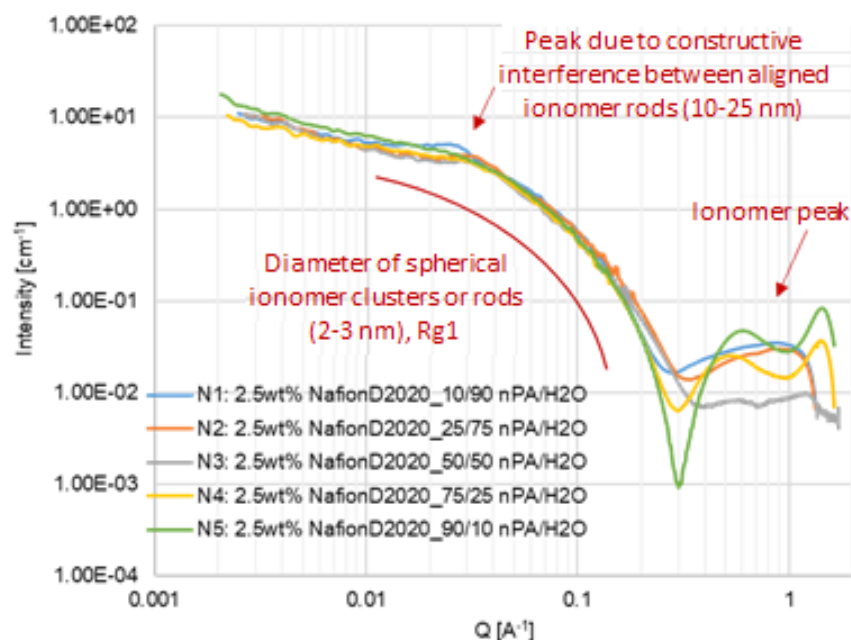


Figure 16 USAXS results for 2.5wt% Nafion ionomer solution for N1: 10/90 nPA/ H₂O, N2: 25/75 nPA/H₂O, N3: 50/50 nPA/H₂O, N4: 75/25 nPA/H₂O, and N5: 90/10 nPA/H₂O dispersions listed in Table 1. Source: ANL

Table II Unified Fitting Results of 2.5wt% Nafion Ionomer Solutions

Sample No.	Spacing between ionomer rods/clusters [nm]	Rg1 [nm]	Porod slope
N1	21.1	3.81	2.8
N2	17.8	3.26	2.63
N3	16.5	3.21	2.21
N4	n/a	3.25	2
N5	n/a	3.11	2.02

The USAXS data for the Pt/Vulcan-ionomer-solvent inks from Table 1 are shown in Figure 17. The data were fit in three scattering regions associated with the Pt nanoparticles (Rg1), the Pt/Vulcan aggregates (Rg2), and with the Pt/Vulcan agglomerates (P3). A summary of the fitting results is given in Table III. The scattering intensities in the intermediate Q region (Rg2, aggregate region) increase with increasing nPA content and the slope (P) in the low q region, which is proportional to the degree of agglomeration, decreases with increasing nPA content. This indicates that nPA is a more suitable solvent for breaking up the Pt/Vulcan catalyst agglomerates in the presence of ionomer. There was no clear trend with nPA contents for the inks without ionomer. These inks had fewer aggregates compared to the inks with the ionomer. This indicates that ionomer is needed to effectively break up the Pt/Vulcan agglomerates and disperse the Pt/Vulcan aggregates.

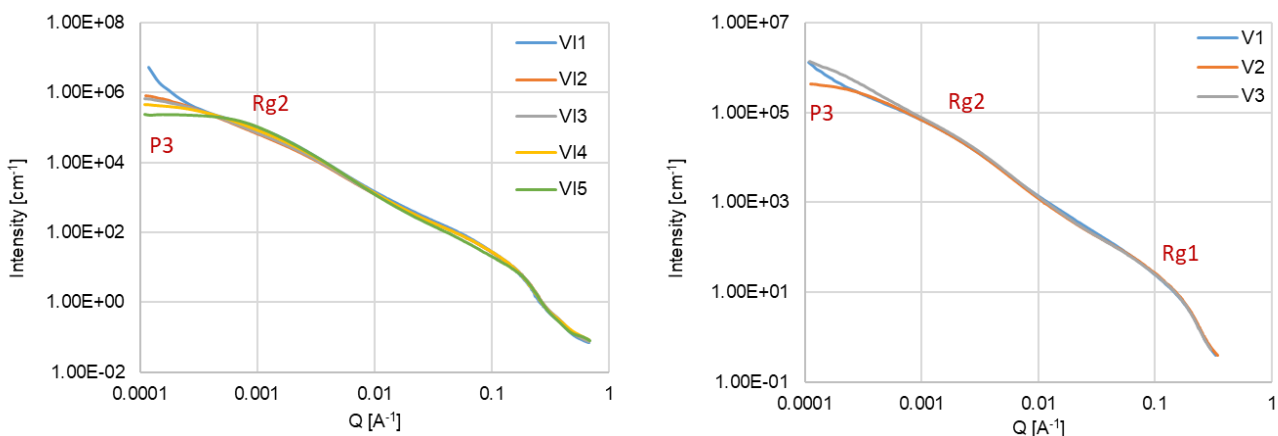


Figure 17 USAXS profiles for Pt/Vulcan-ionomer-solvent inks as a function of solvent mixture and ionomer. Source: ANL

Table III Sample List and Unified Fitting Results of Pt/Vulcan Inks

Sample No.	Sample Composition	Solvent	Rg1 [nm]	Rg2 [nm]	P3
VI1	5wt%Pt-VULCAN-0.5 IC	10/90 nPA/H ₂ O	2.6	114.4	3.45
VI2	5wt%Pt-VULCAN-0.5 IC	25/75 nPA/H ₂ O	2.5	205.7	1.57
VI3	5wt%Pt-VULCAN-0.5 IC	50/50 nPA/H ₂ O	2.4	202.3	1.48
VI4	5wt%Pt-VULCAN-0.5 IC	75/25 nPA/H ₂ O	2.1	207.4	1.12
VI5	5wt%Pt-VULCAN-0.5 IC	90/10 nPA/H ₂ O	1.6	325.8	1
V1	5wt%Pt-VULCAN-0 IC (no ionomer)	10/90 nPA/H ₂ O	2.3	60.7	2.56
V2	5wt%Pt-VULCAN-0 IC (no ionomer)	50/50 nPA/H ₂ O	2.4	214.6	1.2
V3	5wt%Pt-VULCAN-0 IC (no ionomer)	90/10 nPA/H ₂ O	2.4	196.2	2.11

Colloidal Chemistry, Surfactant Research, Slurry Processing, Deposition and Drying/Curing Methods (ORNL Lead Laboratory)

Colloidal Chemistry and Slurry Processing

ORNL performed relevant ink studies to determine rheology, surface tension and zeta potential for materials used for multi-layer coatings. Carbon (C) particles coated with Pt catalyst (46.5% for Pt/C) were received from Tanaka. The particle size was measured using SEM, and the particle surface chemistry was assessed using energy dispersive X-ray spectroscopy (EDS) and XPS. The SEM images of the particles are shown in Figure 18. The average C primary particle size is approximately 50 nm.

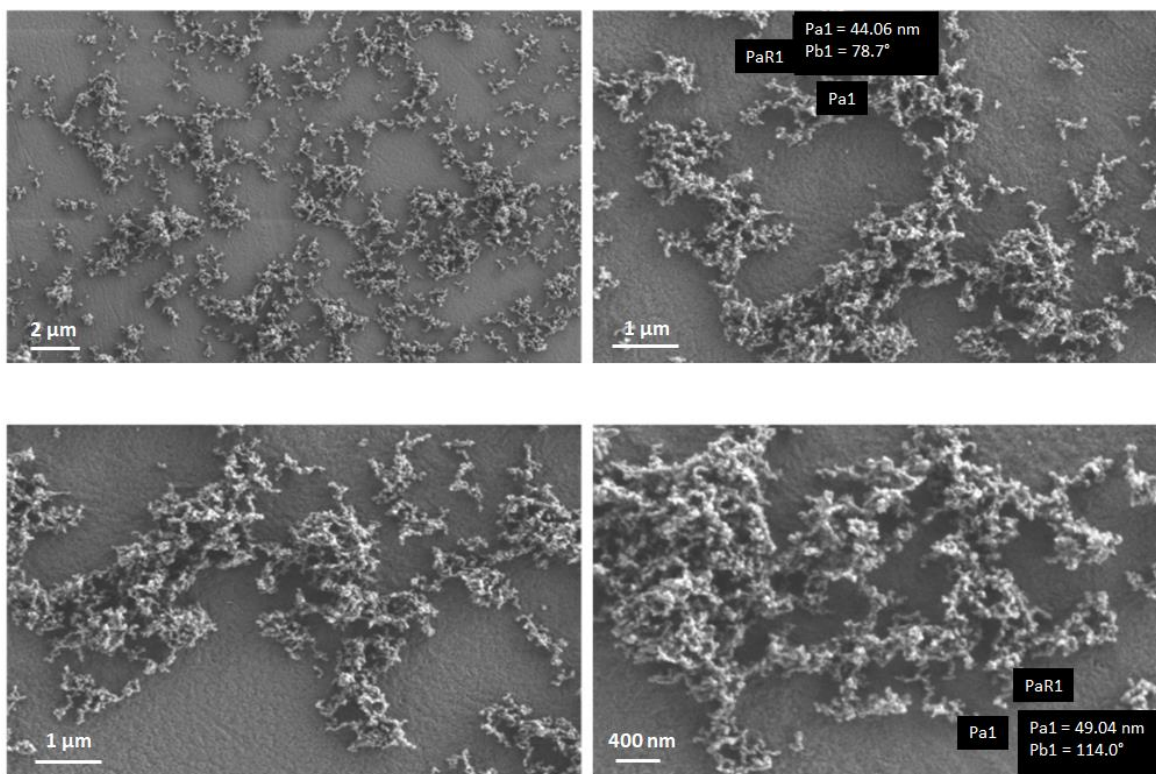


Figure 18 SEM images of the carbon particles coated with Pt catalyst; carbon primary particle size is approximately 50 nm. Source: ORNL

The element analysis was performed using EDS measurements as shown for the area in Figure 19 (a) and the element maps are shown in Figure 19 (b) for Pt and Figure 2 (c) for carbon. The measurements showed a uniform distribution of Pt on the surface of the carbon particles.

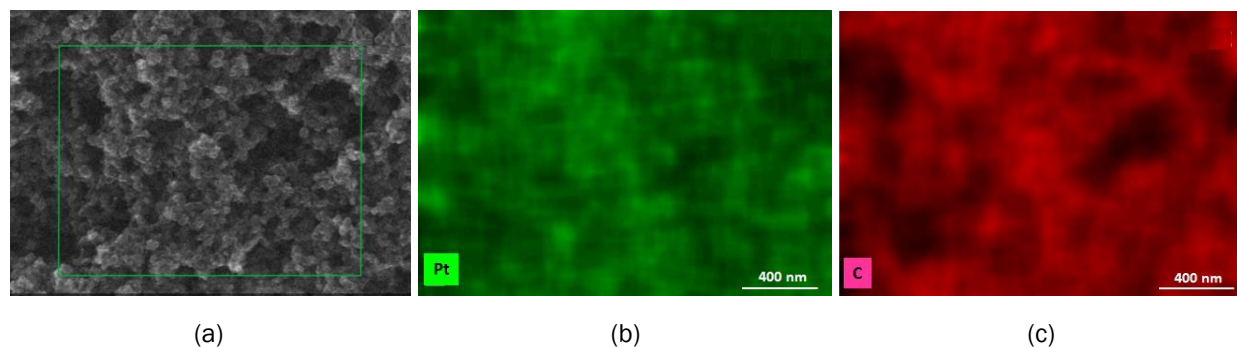


Figure 19 (a) Area where EDS measurements were taken and the element maps for (b) platinum and (c) carbon atoms on the surface of the coated particles. Source: ORNL

XPS analysis was performed on the Pt/C powder to calculate the element atomic percent (at%) on the surface of the particles. The powder was dispersed onto double-sided tape fixed to a glass slide. After inserting the sample into the XPS analysis chamber, a wide energy range survey scan was acquired to determine all elements present. The measurement results and the fitting analysis of the spectra are summarized in Figures 20 (a) and (b) respectively. Along with C and Pt, O was observed as well as a near-trace amount of nitrogen. The line shape of the C 1s indicates that the carbon is primarily graphitic in nature (sp²). The Pt 4f was primarily metallic, but a small doublet assigned to Pt-oxide (likely PtO₂) was needed to get a good peak fit. The Pt content is 5.5 at% according to the spectra analysis in Figure 20 (b).

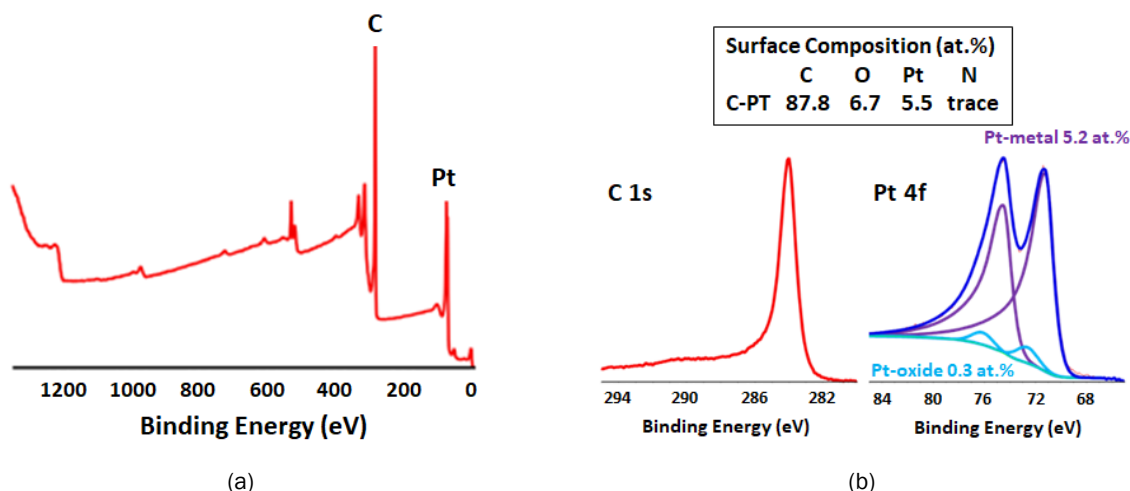


Figure 20 (a) Survey XPS spectrum of the Pt/C particles and (b) XPS core data analysis and the element at% on the surface of the particles. Source: ORNL

Zeta potential measurements were performed on colloidal suspensions of the Pt/C particles dispersed in mixtures of water and IPA at various pH values. The surface potential of the particles was measured in order to optimize the dispersion during slurry processing. A representative plot of these zeta potentials at different pH values is shown in Figure 21.

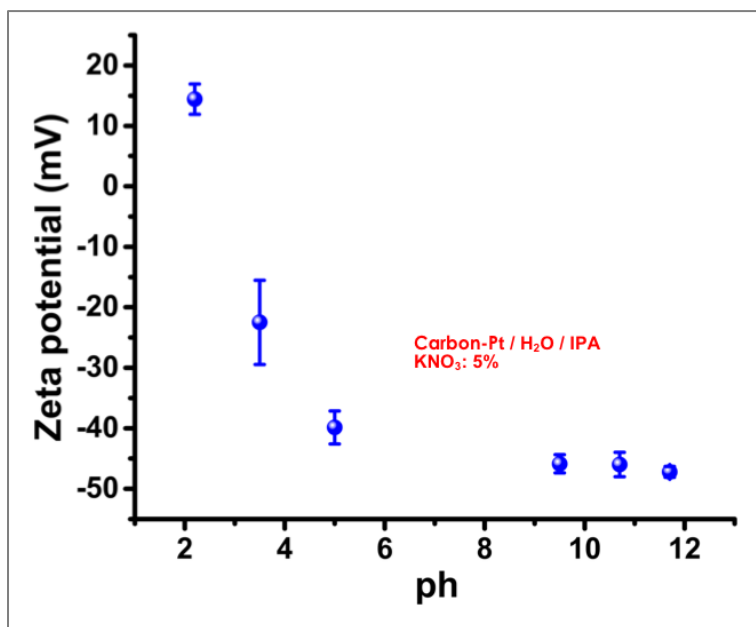


Figure 21 Zeta potential measurements of Pt/C particles dispersed in water having 5% KNO₃. Source: ORNL

Zeta potential measurements were also performed on colloidal suspensions of Pt/C particles dispersed in water, IPA, and Nafion D2020. A representative plot of the zeta potential variation at different IPA vol% is shown in Figure 22. The zeta potential decreases when the IPA content is increased. Slurries based on optimum particle dispersion conditions will be formulated and their rheological properties will be measured in upcoming work.

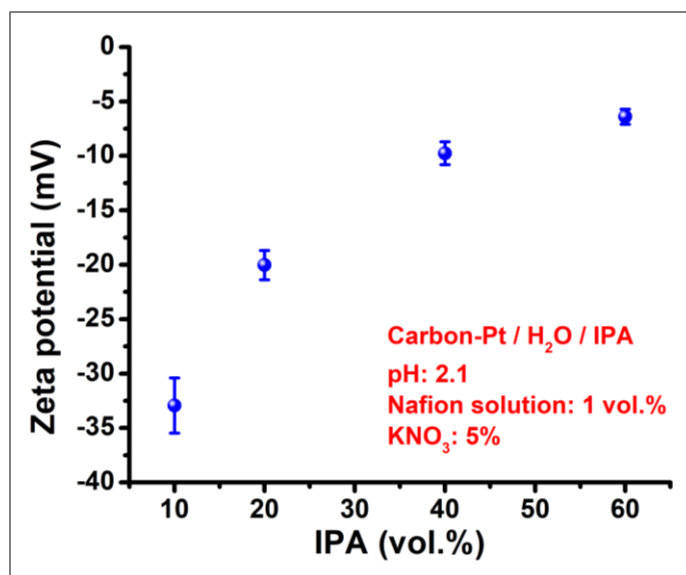


Figure 22 Zeta potential measurements of Pt/C particles dispersed in water, IPA and Nafion. Source: ORNL

Deposition and Drying/Curing

NREL and ORNL consulted on coating methodologies, such as combined gravure and slot-die and dual slot-die, and key parameters to achieve deposition of an ionomer overlayer on a PEMFC cathode. ORNL's objective was to either complete the ionomer overlayer deposition step at the same time as the cathode electrocatalyst layer or eliminate the need for it altogether. Technical drawings of the ORNL pilot slot-die coating head were supplied to SNL for implementation into the coating deposition physics model. A spinoff from one of the CRADA projects was that the design for pattern gravure rollers was completed. ORNL and NREL also agreed on separator and coating materials for the patterned coatings; however, the formulations for the ceramic coatings need to be redesigned due to poor wetting of the separator.

It is desirable from a high-volume manufacturing standpoint to minimize the amount of organic solvent used in the PEMFC inks and maximize the solids loading. The former goal reduces the amount of solvent that must be recovered (i.e. through vacuum distillation, etc.), and the latter goal reduces the total thermal budget and dryer length needed to remove water and organic solvent from the coated ink. The conventional spraying approach typically uses solids loadings of 0.1-0.3 wt% to avoid nozzle clogging, but the AMO R2R Collaboration is attempting to increase this level by two orders of magnitude for slot-die and gravure coating. Certain challenges that arise when increasing the solids loading are re-optimization of the ink mixing protocol and preventing agglomeration of ionomer and secondary catalyst particles. High-shear mixing and adjustment of the formulation chemistry through surfactant addition or solvent composition modification may be necessary to implement these much higher ink solids loadings.

ORNL prepared slurries of 8, 10, and 12 wt% Pt/C particles for rheological measurements. The 12 wt% slurry was not homogeneous, and the particles were agglomerated due to the high particle content. The viscosity and the storage modulus of the 8 wt% and 10 wt% slurries as a function of the shear rate and angular frequency are shown in Figures 23 (a) and (b), respectively. The 8 wt% slurry has lower viscosity and was easier to process.

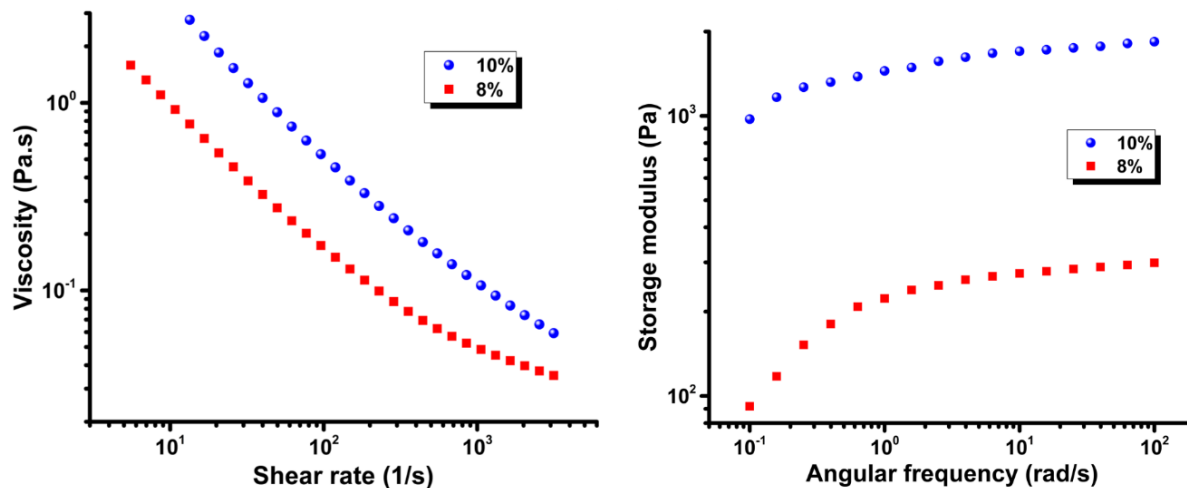


Figure 23 Rheological properties of the slurries with 8 wt% and 10 wt% Pt/C content. Source: ORNL

GDEs were coated with the 8 wt% and 10 wt% slurry formulations and their surface structure and chemistry were characterized. The coatings were applied using a doctor-blade technique. SEM images of the coating cross-section with the 8 wt% formulation are shown in Figure 24. The catalyst coating layer can be clearly seen on the surface of the GDE substrate. The thickness of the coating is approximately 25-50 μm . The element map according to the EDS analysis is shown in Figure 25. The Pt/C particles are restricted on the surface of the coating and did not diffuse into the GDE substrate.

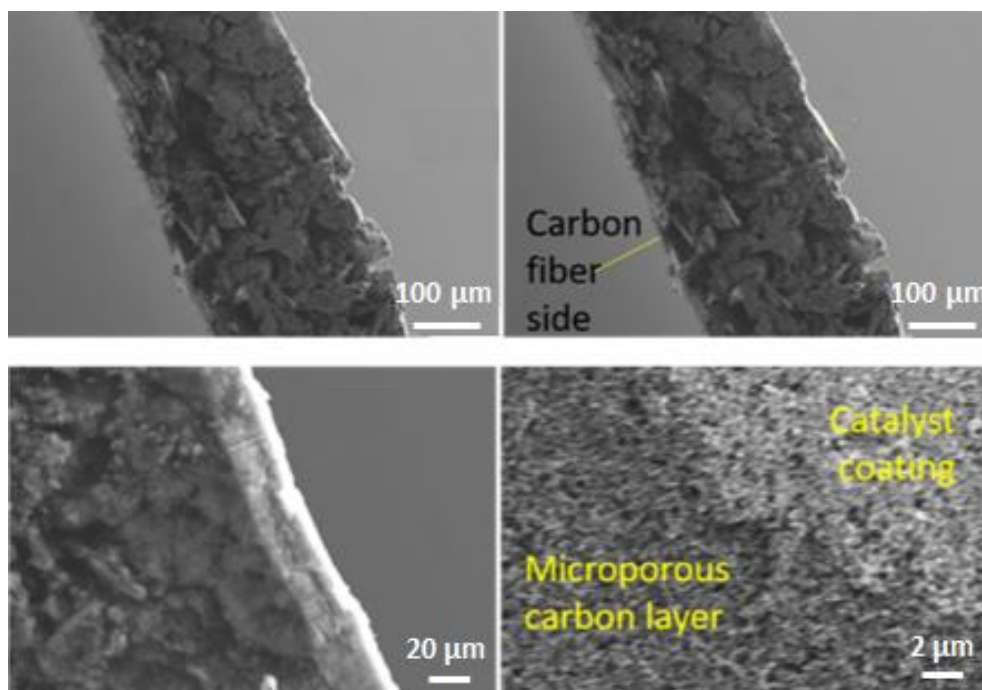


Figure 24 SEM cross-section images of the GDE coated with 8 wt% slurry formulation at different magnifications. Source: ORNL

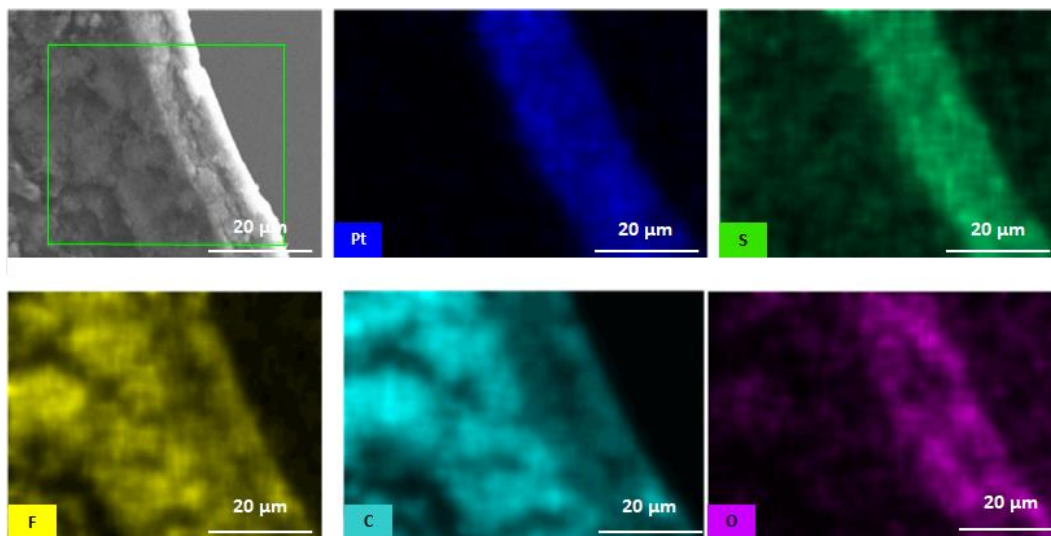


Figure 25 The area where EDS measurements were taken and the element maps according to EDS analysis of the 8 wt% coating on the GDE substrate. Source: ORNL

Optical microscope images of the coating's surface for the 8 and 10wt% slurry formulations are shown in Figure 26. For comparison, the images were obtained under the same magnification. Streaks were formed on the surface of both coatings during the drying process. However, the streaks are less pronounced in the 8 wt% coating.

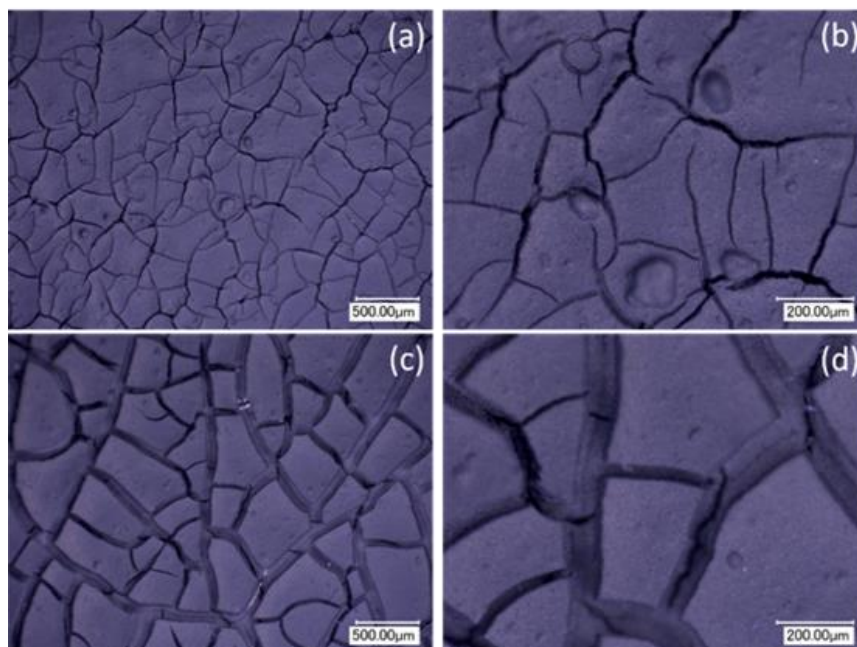


Figure 26 Optical microscope images of the coatings based on (a) and (b) for the 8 wt% and (c) and (d) 10 wt% formulations. Source: ORNL

The thicknesses of the coatings were also measured using confocal microscope techniques. The measured thicknesses of both coatings were approximately 25-50 μm which is in good agreement with the SEM cross-section measurements. Representative images of the surface profile according to the optical microscope are shown in Figure 27.

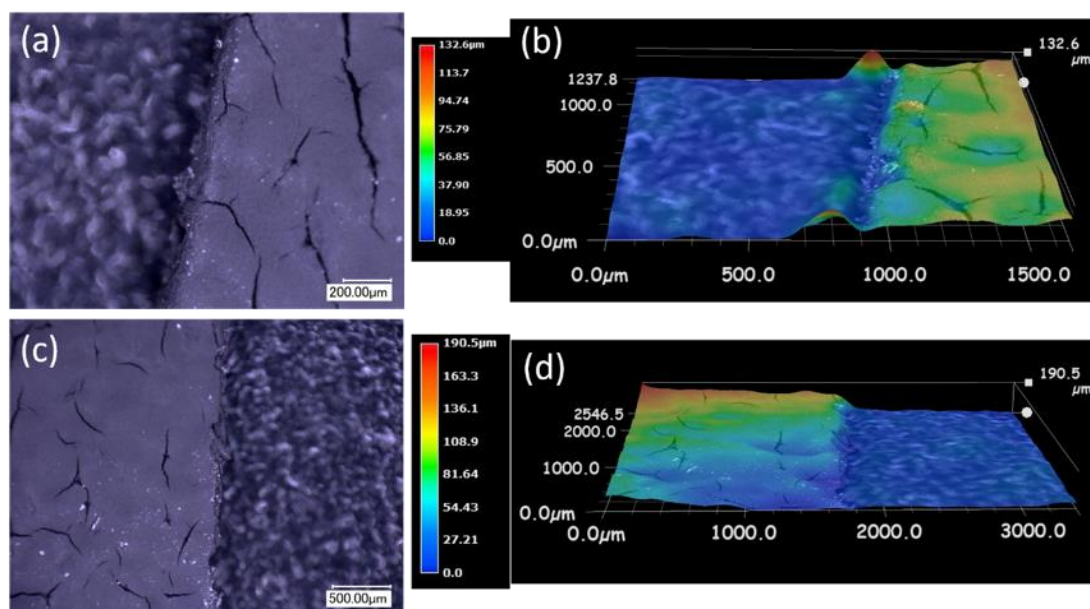


Figure 27 Thickness profile measurements for the (a) and (b) 8 wt% and (c) and (d) 10 wt% coatings. Source: ORNL

Atomic force microscopy (AFM) measurements were performed on the surface of the coatings to measure the size of the particle agglomerates. The size of the surface features on the 10 wt% coating was higher than the limits of the AFM instrument and the surface features of that coating were not measured. The surface of the 8 wt% coating was smoother. The surface tomography under an optical microscope is shown in Figure 28 (a) and the representative surface topography according to AFM imaging is shown in Figure 28 (b). The size of the individual Pt/C catalyst particles was measured to be 15-20 nm. The size of the surface features was found to vary depending on the size of the particle agglomerates.

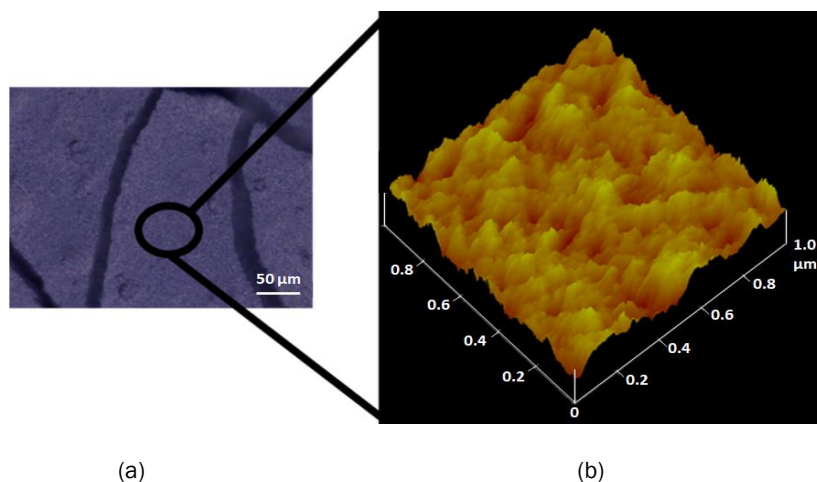


Figure 28 Surface topography of the 8 wt% coating under (a) an optical microscope and (b) according to AFM imaging measurements. Source: ORNL

Surface profiles of areas with well-dispersed and agglomerated particles are shown in Figure 29 and Figure 30, respectively. Areas with well dispersed particles have surface features of a few nanometers, whereas, the size of the particle agglomeration is a few micrometers.

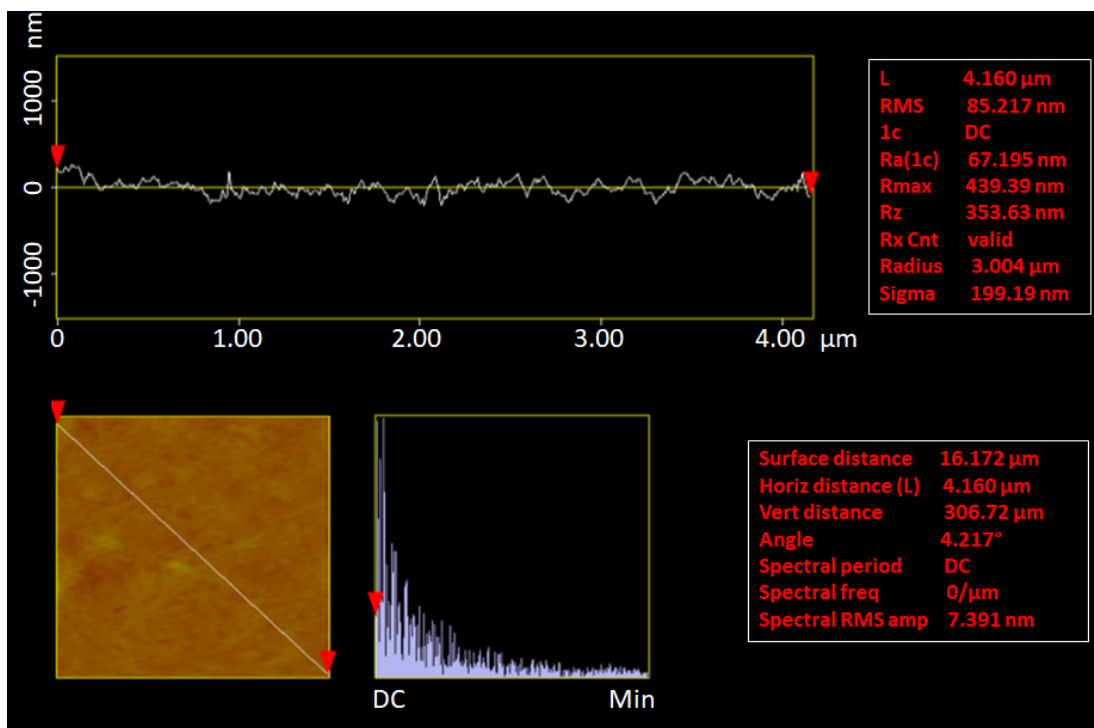


Figure 29 AFM surface profile of an area with well dispersed particles on the surface of the 8 wt% coating. Source: ORNL

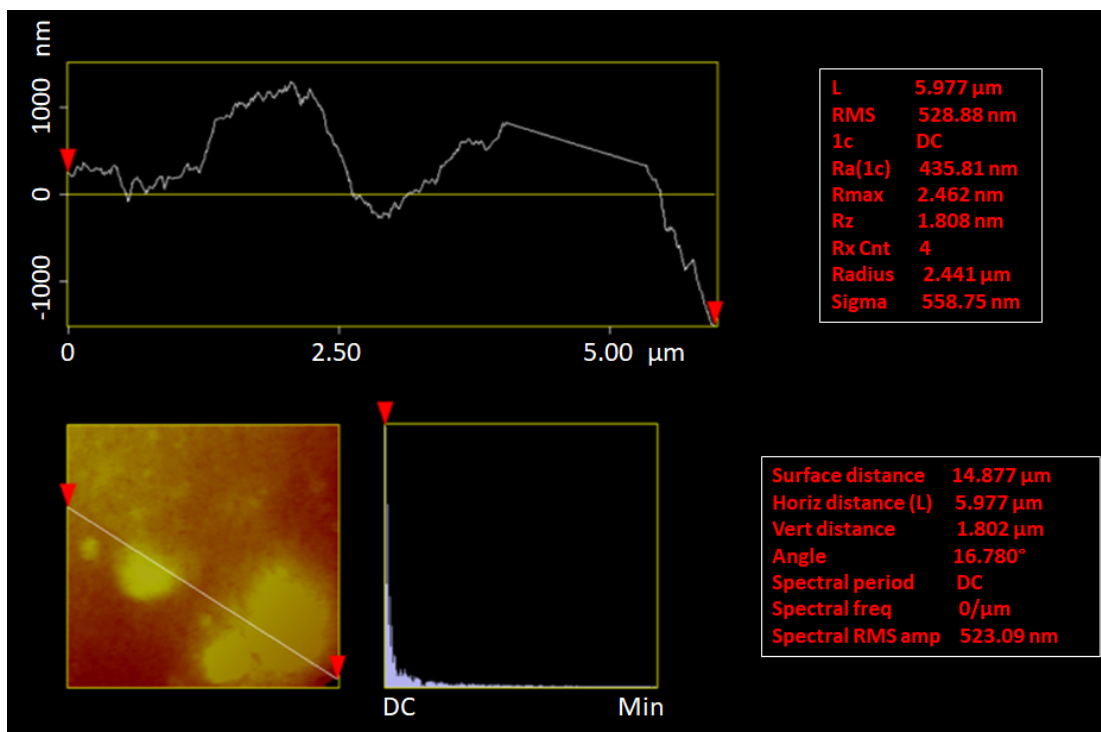


Figure 30 AFM surface profile of an area with particle agglomeration on the surface of the 8 wt% coating. Source: ORNL

A 6 wt% slurry was also used to coat a GDE. The slurry was dilute and diffused through the GDE layer. The 8 wt% slurry was found to give the best results. The formulation was scaled and was used to coat several feet of GDE with a slot-die technique.

The 8 wt% slurry with a 12.16 wt% total solid content was scaled and used to coat a GDE with a slot-die technique. SEM images of the coated GDE are shown in Figure 31. Micrometer size cracks were formed on the surface of the coating during the drying process.

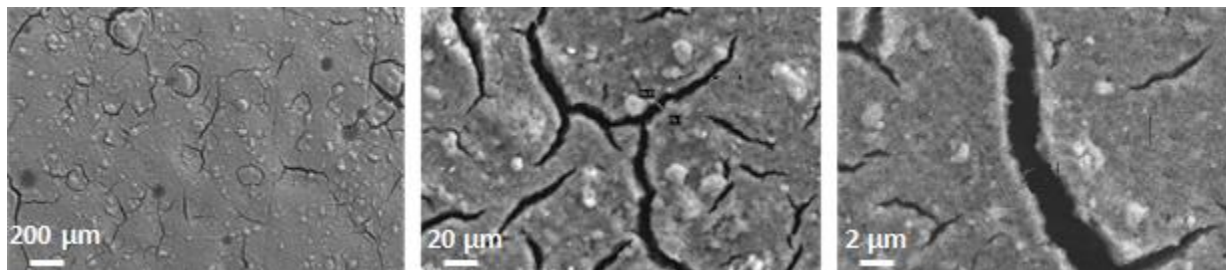


Figure 31 SEM images at different magnifications of the coated GDE using a slot-die technique. Source: ORNL

The thickness of the coating was measured using SEM imaging on the cross-section of the coating as shown in Figure 32. The thickness of the coating was approximately 20 μm which was comparable to the thickness of the coating using a doctor-blade technique. The EDS element map of the cross-section is shown in Figure 33. The Pt/C particles did not diffuse in the GDE; however, Pt was detected only on the top (coated) surface of the GDE.

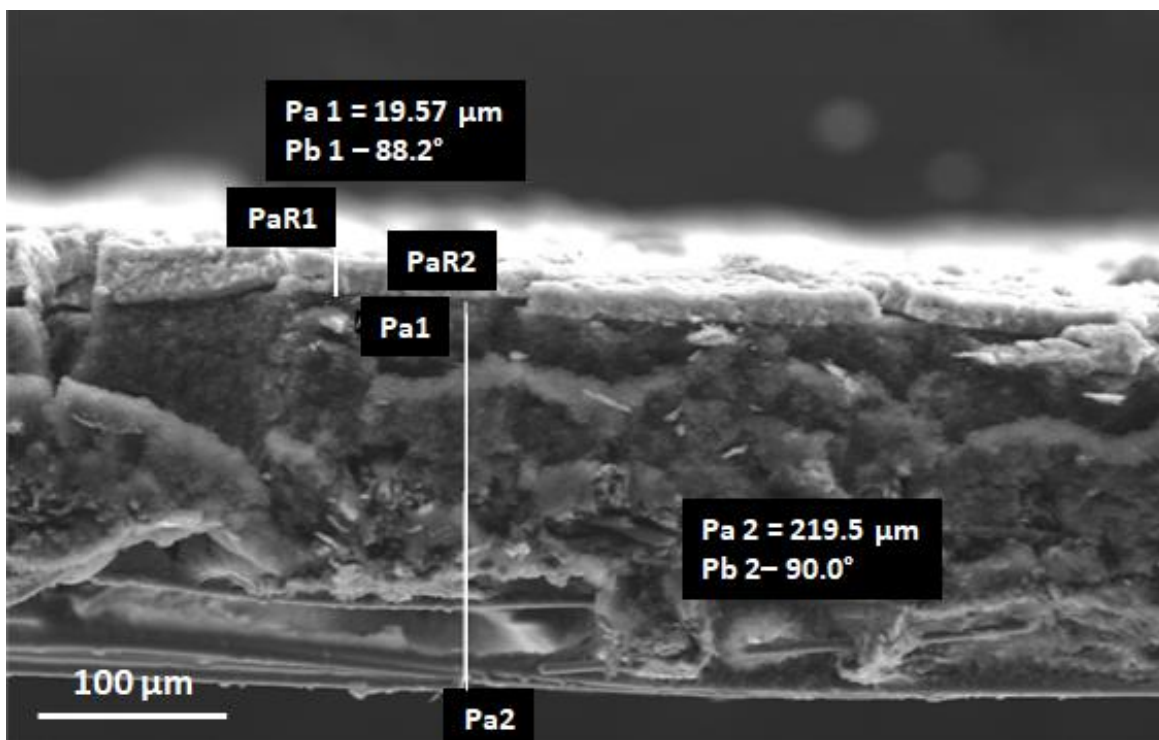


Figure 32 SEM cross-section image of the slot-die coated GDE. Source: ORNL

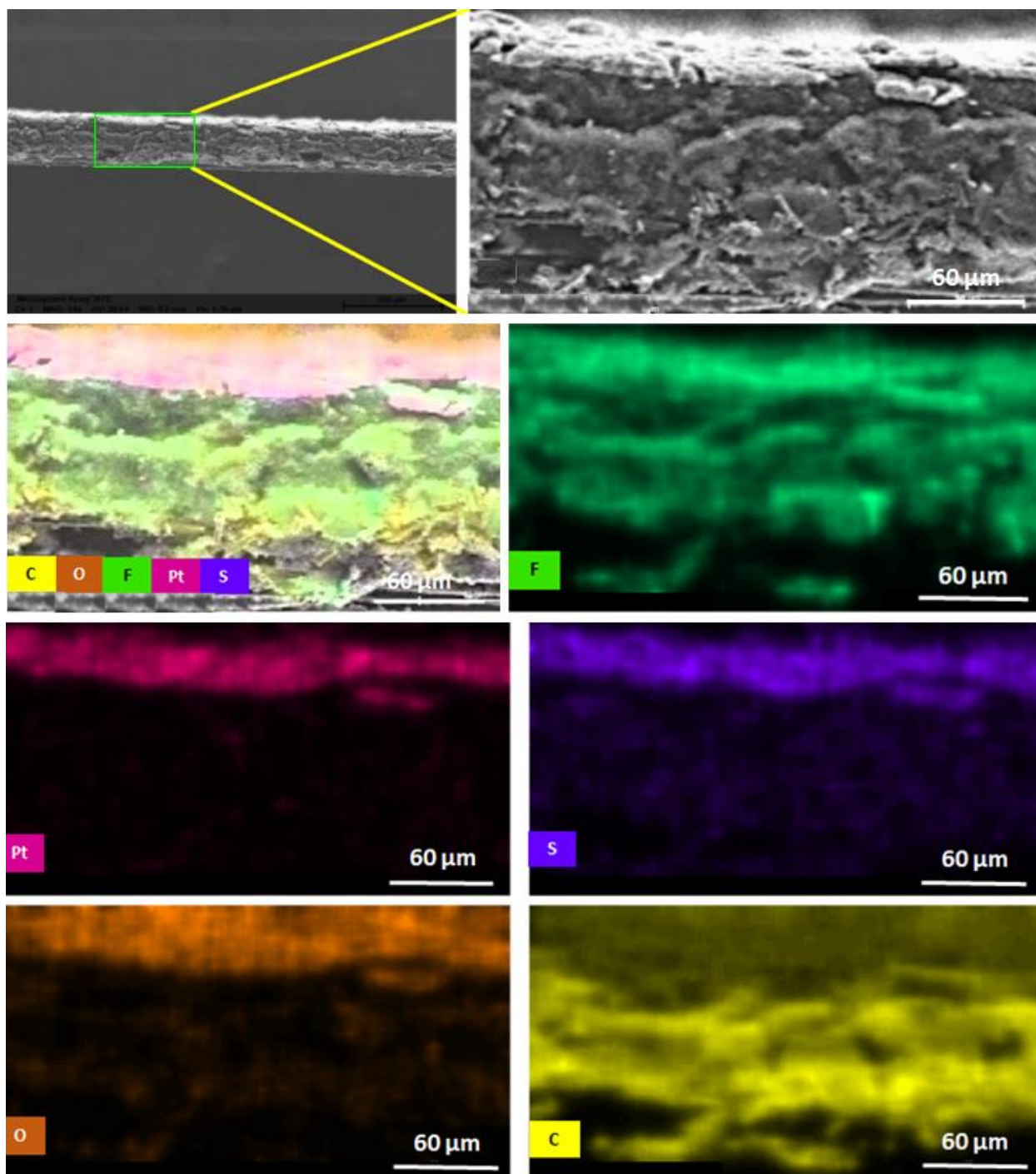


Figure 33 EDS analysis of the cross-section of the slot-die coated GDE. Source: ONRL

ORNL continued to investigate rheological properties by studying the particle agglomeration in the slurry at different high shear mixing conditions. The slurries were used to coat gas diffusion electrodes (GDE). The size of the particle agglomerates was measured on the GDE surface. The slurry composition was 8 wt% in Pt/C particles for a 12.16 wt% of total solids. Mixing at 6,000 revolutions per minute (rpm) for 1.5 hours was not sufficient to deagglomerate the particles. The GDE showed low performance according to the in situ measurements that were performed at NREL. This was attributed to the catalyst particle agglomeration.

The high shear mixing speed was increased to 10,000 rpm and slurries were prepared at different mixing times of 15, 30 and 60 minutes. The slurry composition consisted of 8 g of Pt/C, 56.25 g of deionized water, 19.16 g of Nafion D2020 solution, and 16.59 g of 1-propanol. A doctor blade was used to cast the slurries on the gas diffusion layer. The slurries were dried overnight at room temperature and the resulting coated GDEs are shown in Figure 34. SEM images of the GDE top surface at several magnifications are shown in Figure 35 for the slurry prepared at the mixing conditions of 15 minutes at 10,000 rpm. The size of the particle agglomerates varies from 15 to 80 micrometers.

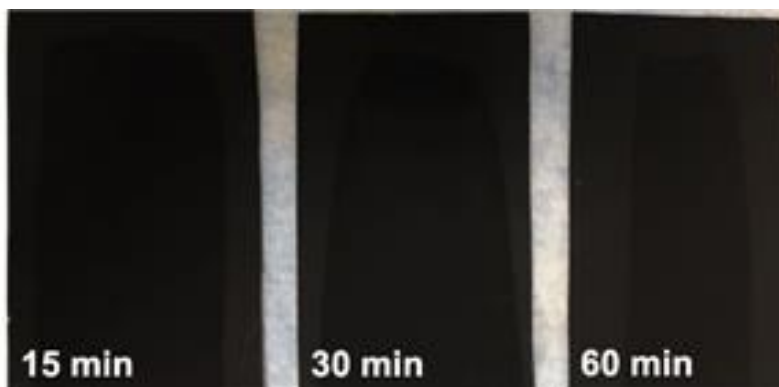
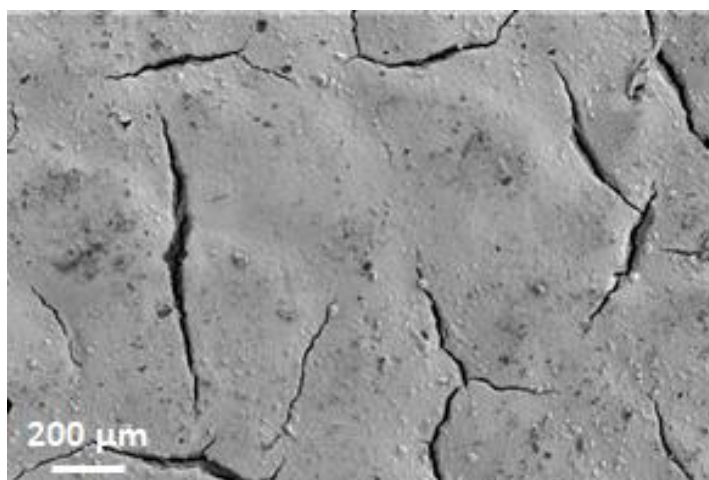
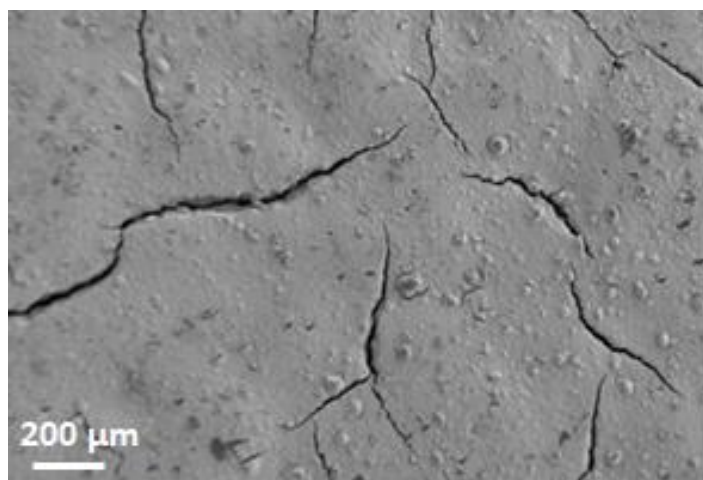


Figure 34 GDEs (4.5 inches x 2.5 inches) coated with slurries prepared at different mixing times. Source: ORNL



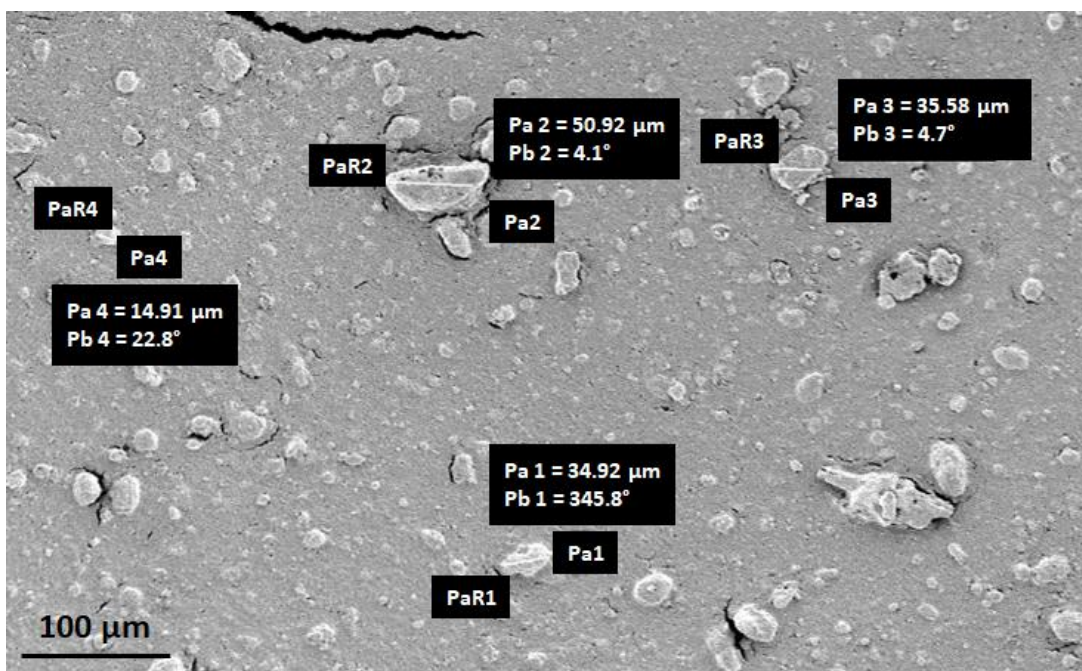
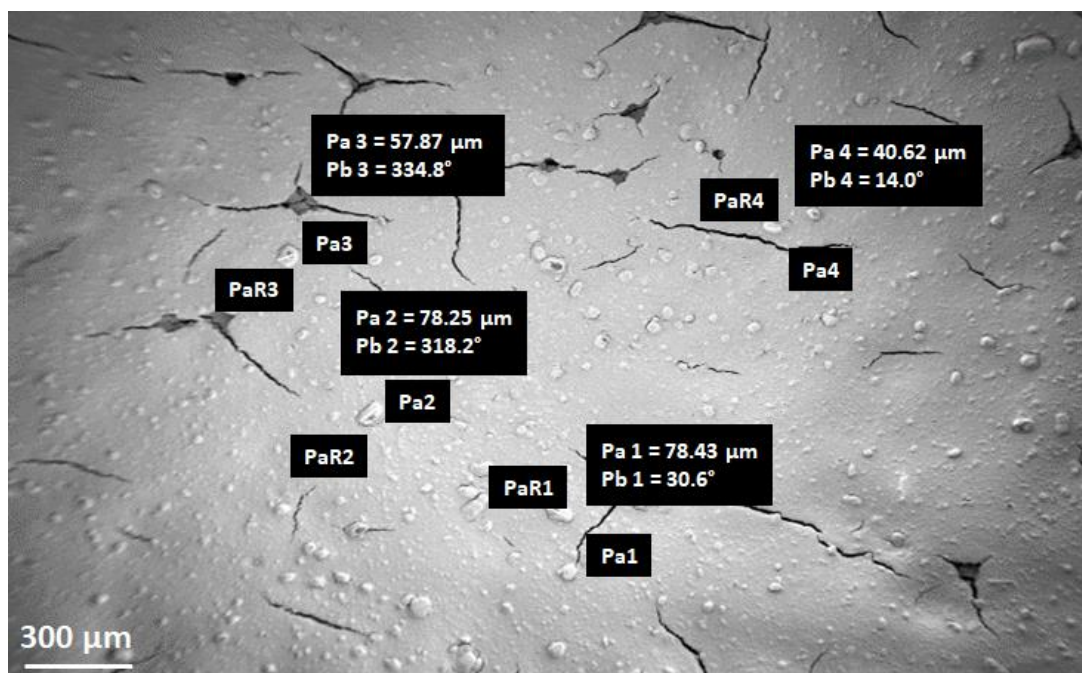
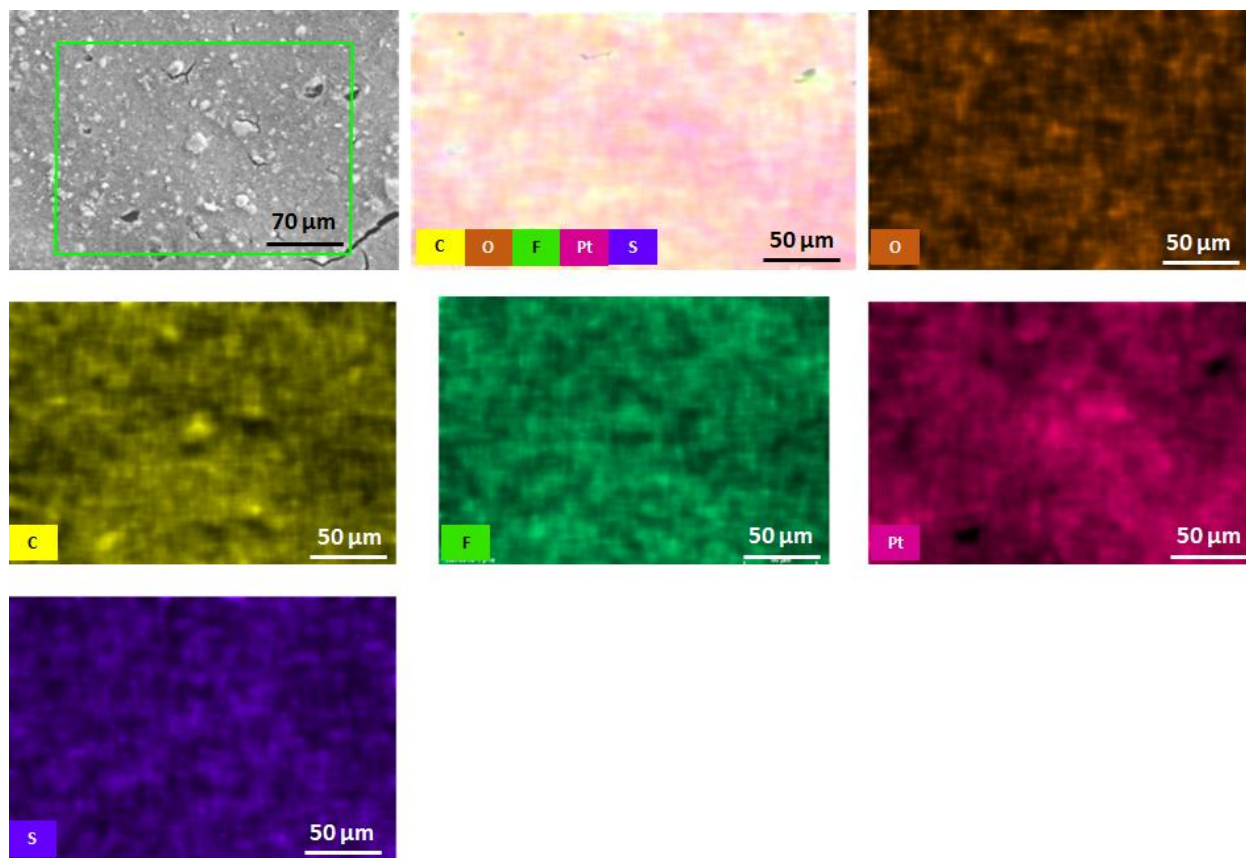
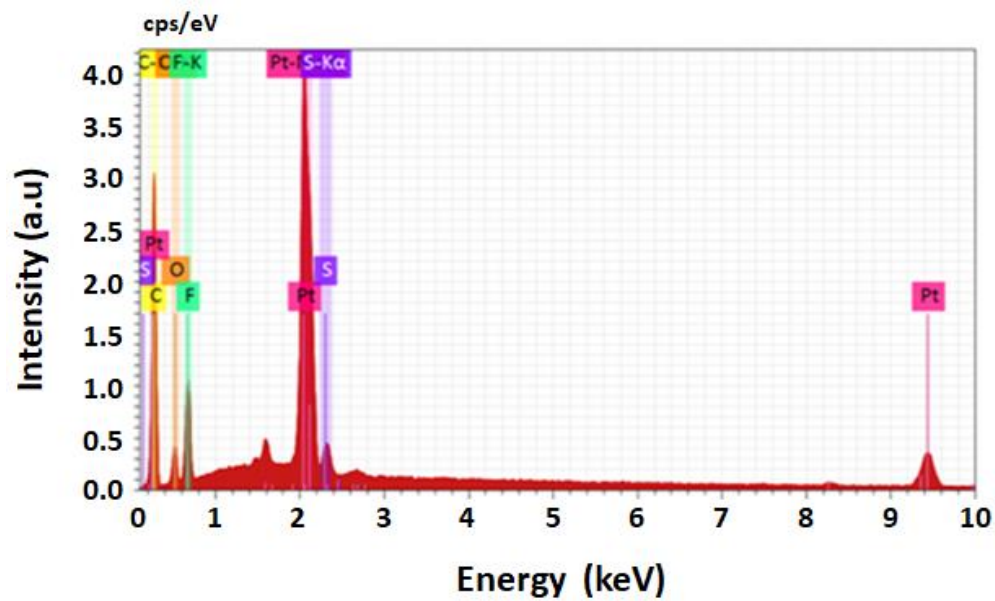


Figure 35 SEM images of the coated GDE for the slurry mixed for 15 min at 10,000 rpm. Source: ORNL

EDS element maps for the are shown in Figure 36 (a) and the element distribution on the GDE surface is uniform according to the EDS analysis shown in Figure 36 (b).



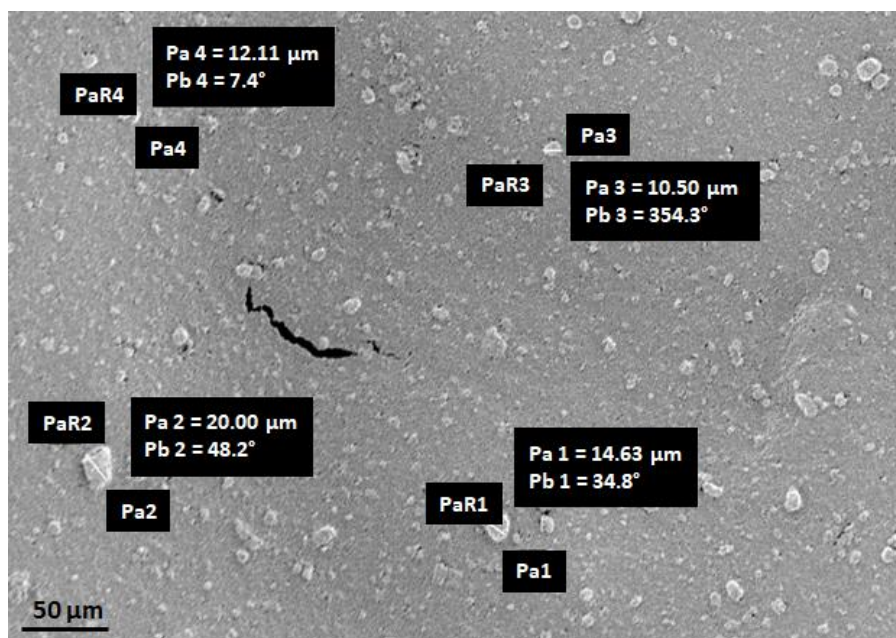
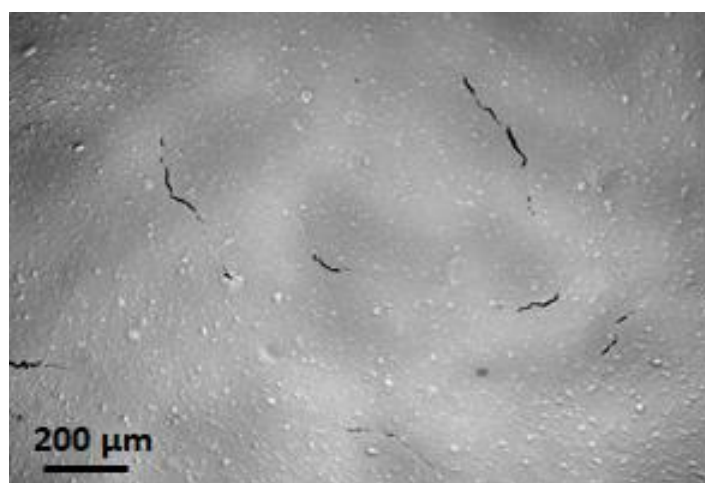
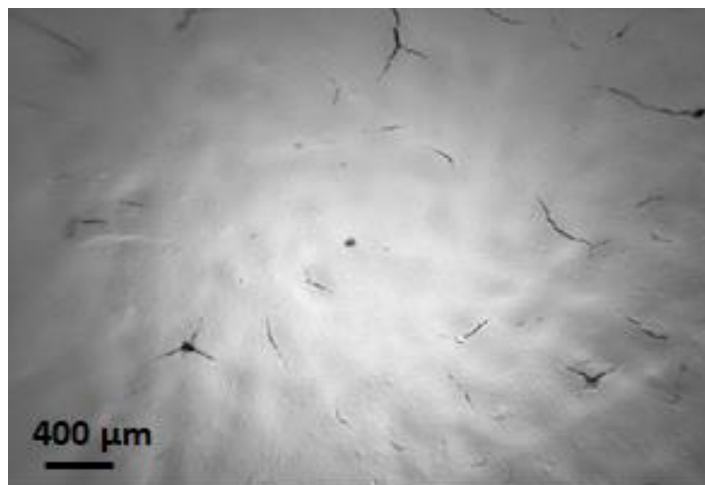
(a)



(b)

Figure 36 (a) EDS element map of the slurry according to (b) the EDS analysis for mixing 15 min at 10,000 rpm. Source: ORNL

SEM images of the GDE surface at several magnifications are shown in Figure 37 for the slurry prepared at the mixing conditions of 30 minutes at 10,000 rpm. The size of the particle agglomerates varies from 12 to 25 micrometers.



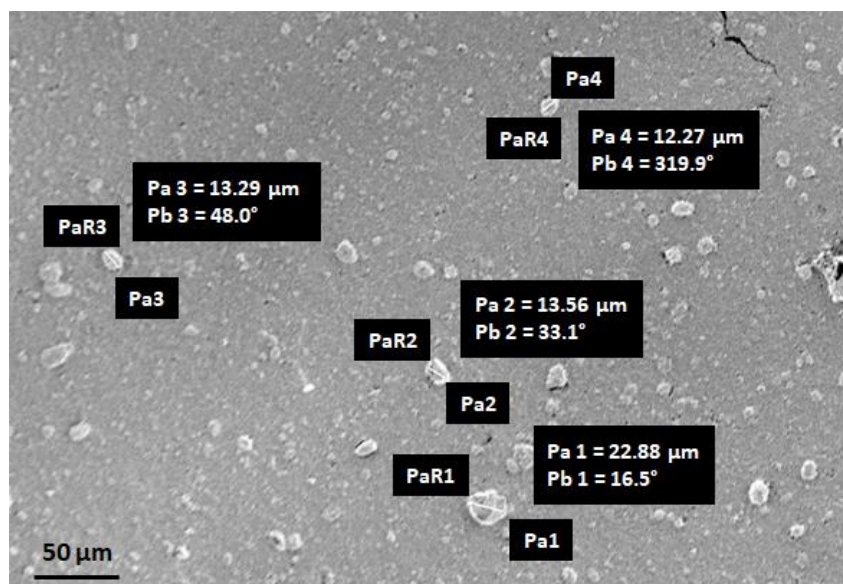
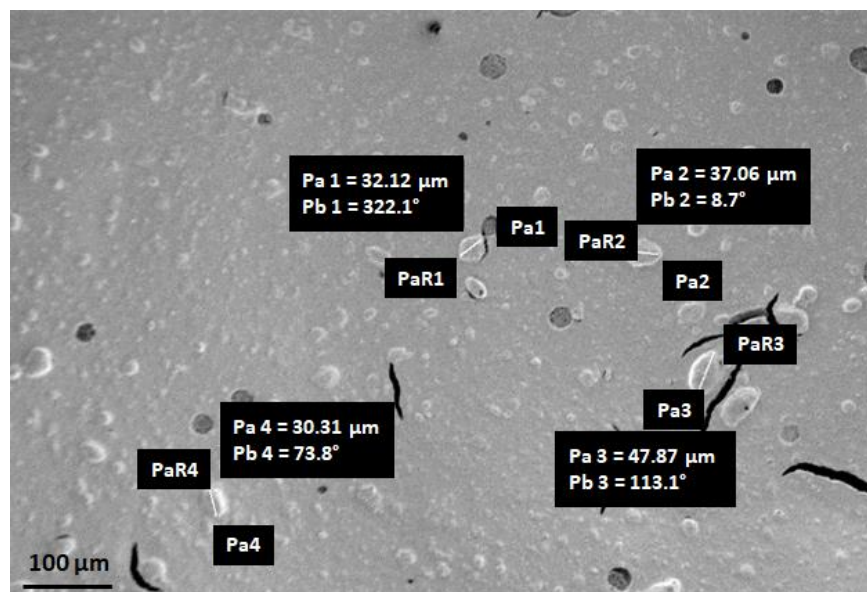
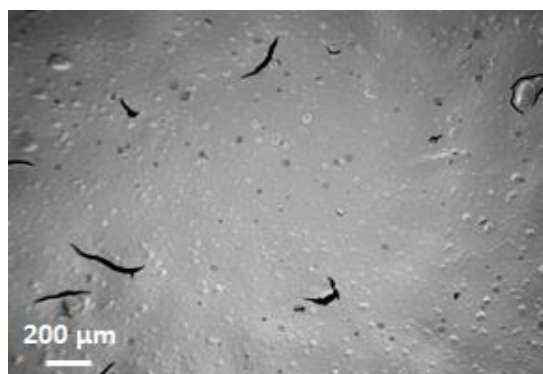


Figure 37 SEM images for the coated GDE slurry mixed for 30 min at 10,000 rpm. Source: ORNL

SEM images of the GDE surface at several magnifications are shown in Figure 38 for the slurry prepared at the mixing conditions of 60 minutes at 10,000 rpm. The size of the particle agglomerates varies from 25 to 50 micrometers.



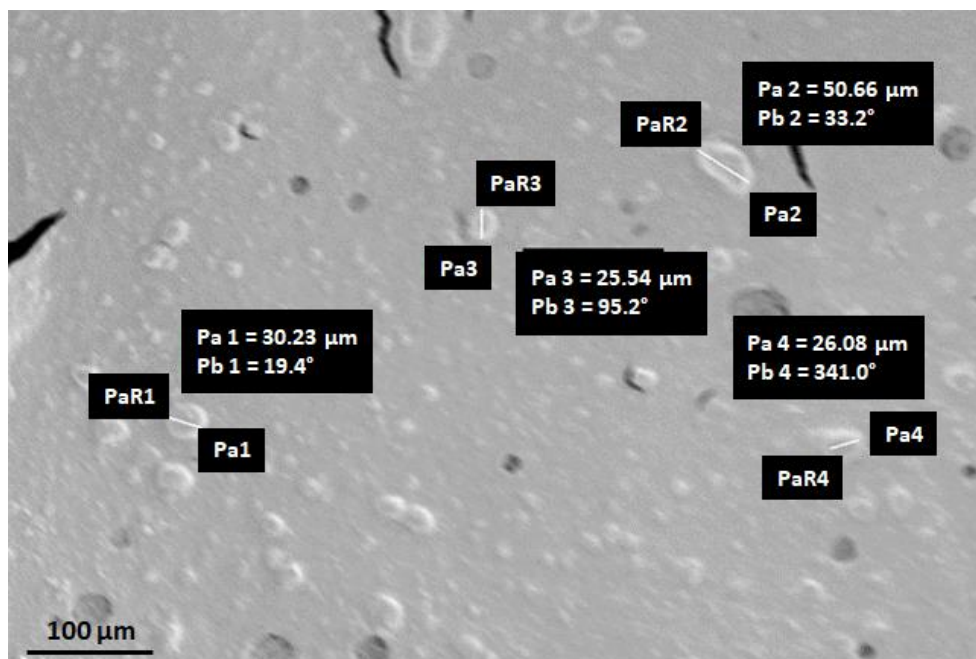


Figure 38 SEM images for the coated GDE slurry mixed for 60 min at 10,000 rpm. Source: ORNL

The mixing for 30 min at 10,000 rpm resulted in smaller size agglomerates. To further reduce the agglomerate size, a more dilute slurry must be synthesized and tested.

ORNL collaborated with NREL and fabricated a GDE with lower Pt loading. The target value was approximately 0.1 mg/cm². To achieve the target value, the slot-die coating parameters were modified. The slurry formulation and coating conditions were as follows for an 8% Pt/C slurry:

Pt/C: 32 g
 Nafion: 76.64 g = solids content = 76.64 g x 0.217 = **16.63 g**
 Water: 225 g
 1-propanol: 66.36 g
 Total Weight = 400 g

Total solid content: Pt/C + solid Nafion = 32 + 16.66 = **48.63 g**
 % of solid content = 48.63/400 = **12.16%**

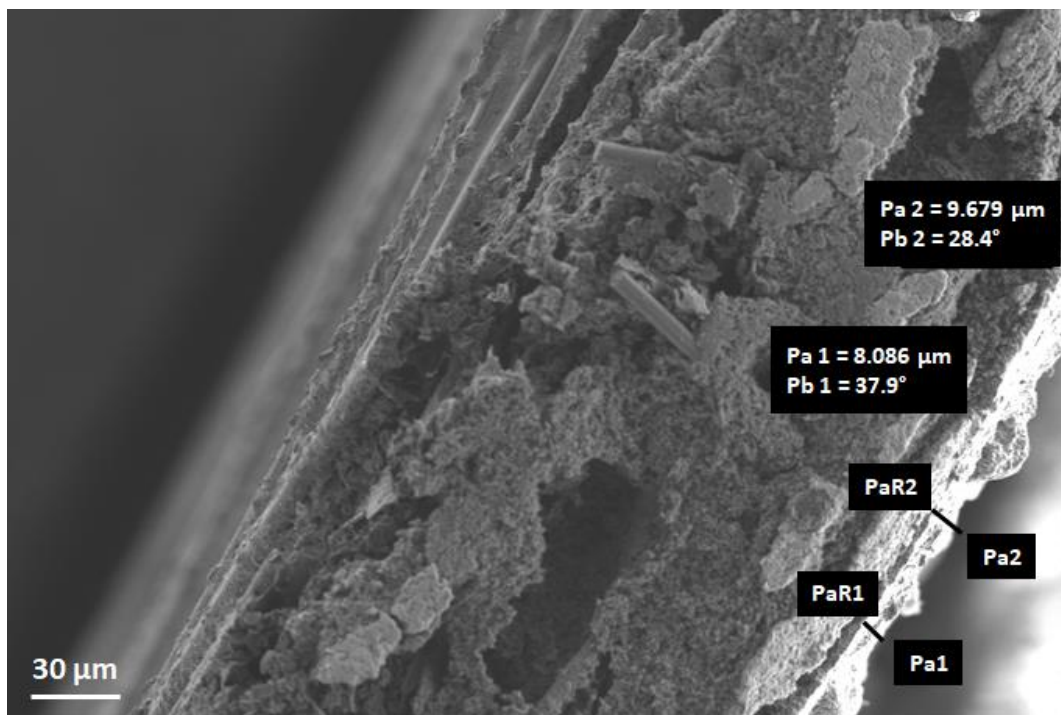
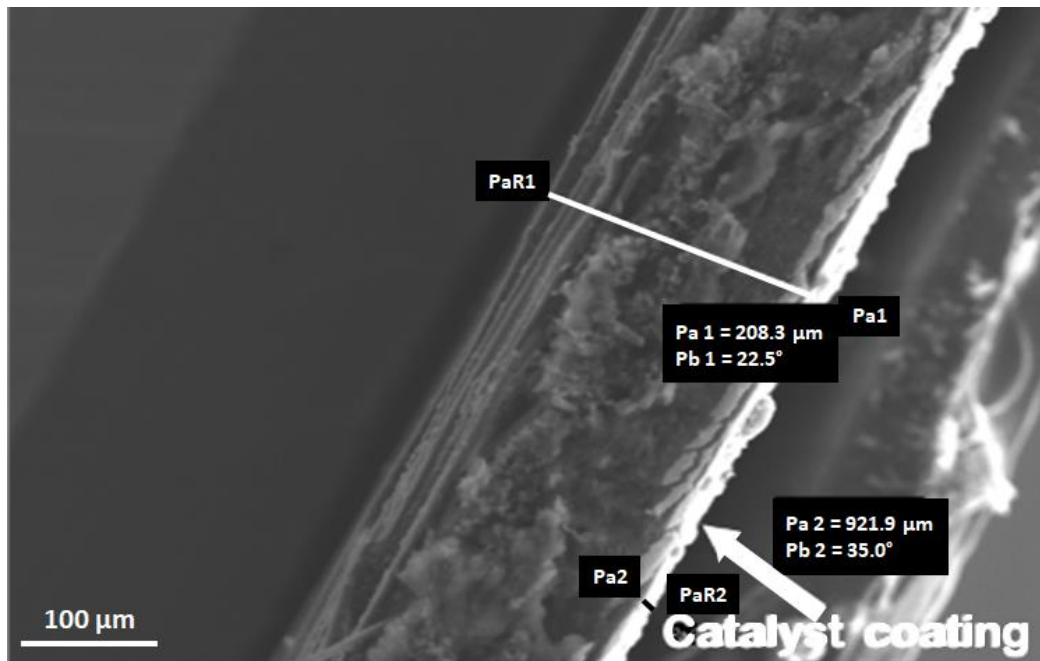
Preparation: Shear mixed by using a small shear mixture in ORNL dry room for 1.5 hours at 6000 rpm

Slot-die coating conditions:

Pump speed (small pump cart) = 20 rpm
 Dynacoat line speed: 3ft/min
 0.584 mg-coating/cm² = **0.179 mg-Pt/cm²**

The Pt loading using this formulation was 0.179 mg/cm² which is very close to the target value. The fabricated GDE was sent to NREL for electrochemical measurements.

SEM images of the GDE cross-section for the GDE with a Pt loading of 0.179 mg/cm² are shown in Figure 39 for different magnifications. The catalyst coating is uniform, and the thickness is 7 to 10 micrometers. The thinner coating resulted in significant lower Pt loading compared to the coating that was prepared earlier (20 micrometers with 0.554 mg-Pt/cm²).



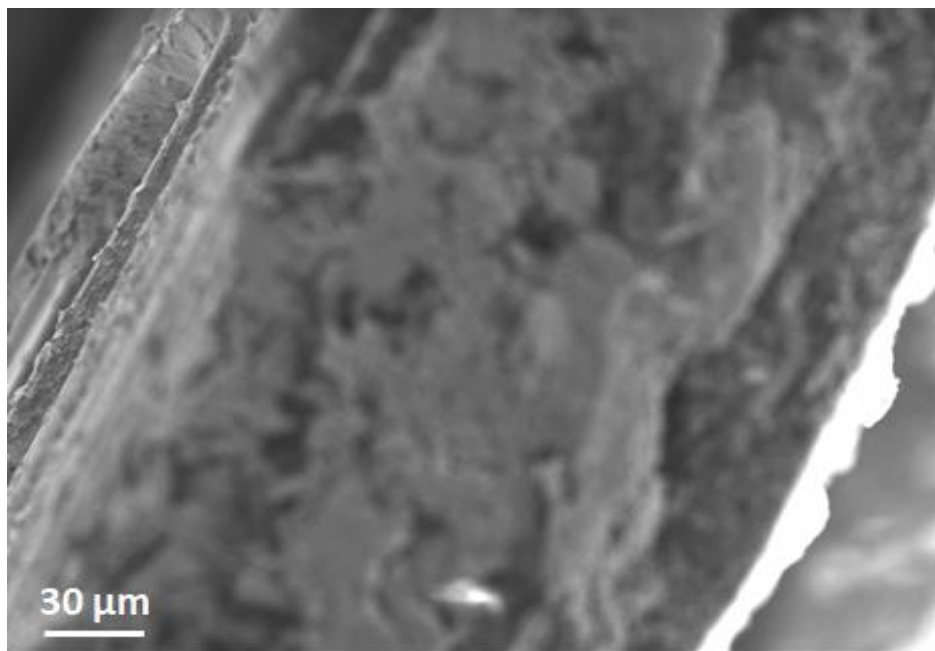


Figure 39 SEM cross section images of the GDE with a Pt loading of 0.179 mg/cm². Source: ORNL

The EDS element analysis of the GDE cross-section is shown in Figure 40. The Pt is mainly in the top coated layer indicating that the Pt/C particles are restricted in the top layer and did not diffuse in the GDE.

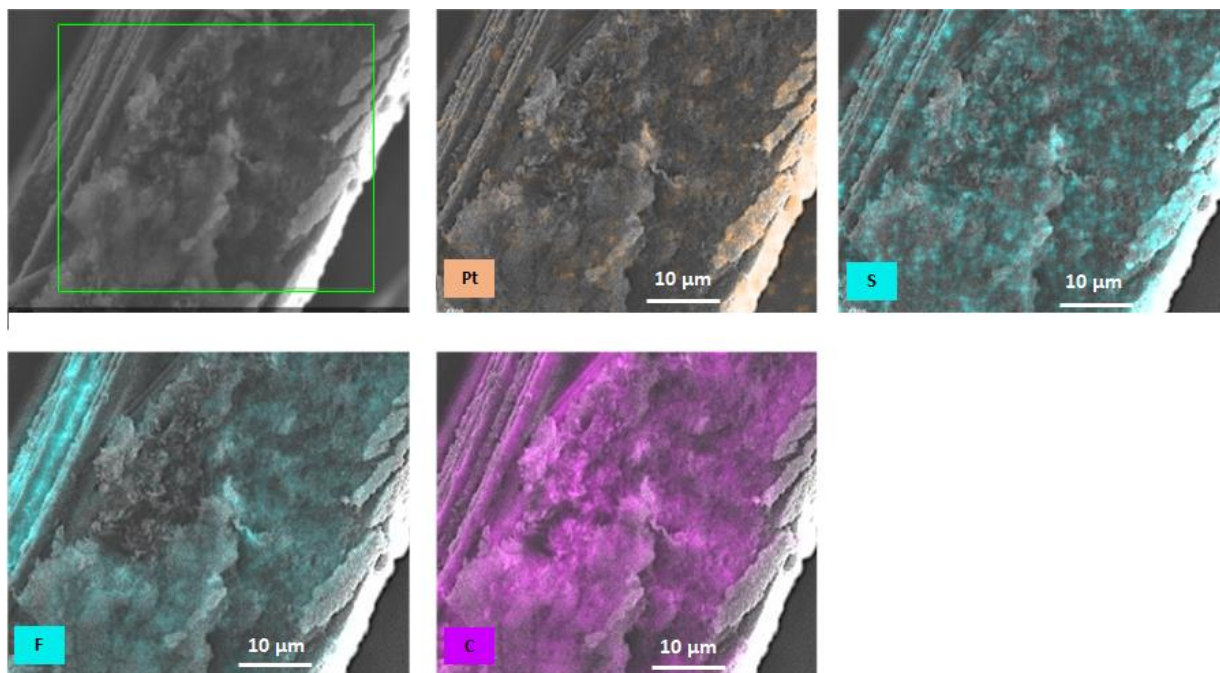


Figure 40 EDS element analysis of GDE cross section with a Pt loading of 0.179 mg/cm². Source: ORNL

SEM images of the coated top surface of the GDE at different magnifications are shown in Figure 41. The particle agglomeration is significant. Electrochemical measurements on the GDE were performed at NREL. The performance was limited by the reduced Pt/C surface area due to the particle agglomeration. To address this issue, ORNL investigated the particle aggregation at different high shear mixing conditions.

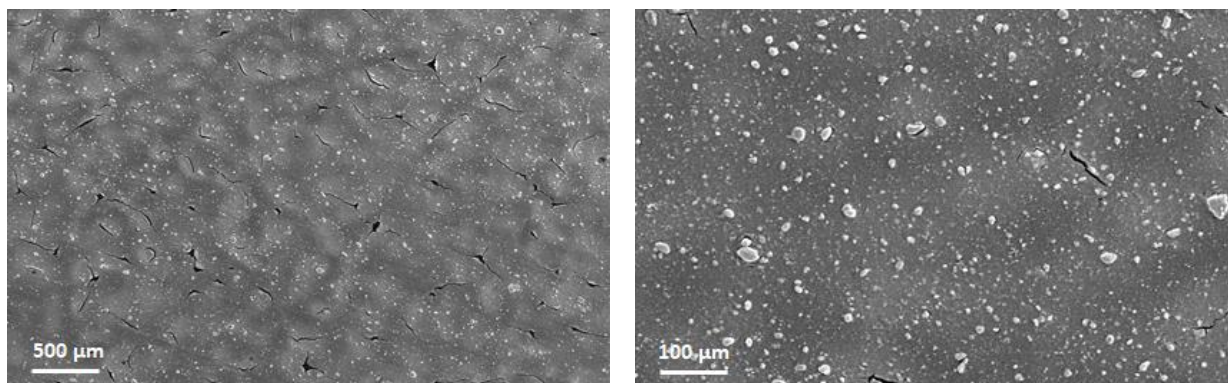


Figure 41 SEM images of the coated GDE showing pronounced particle agglomeration. Source: ORNL

R2R ES Platform Development Support

LLZO nanofibers were electrospun using the experimental setup in Figure 42. LLZO precursors in a stoichiometric ratio were dissolved in aqueous and non-aqueous polymer solutions.

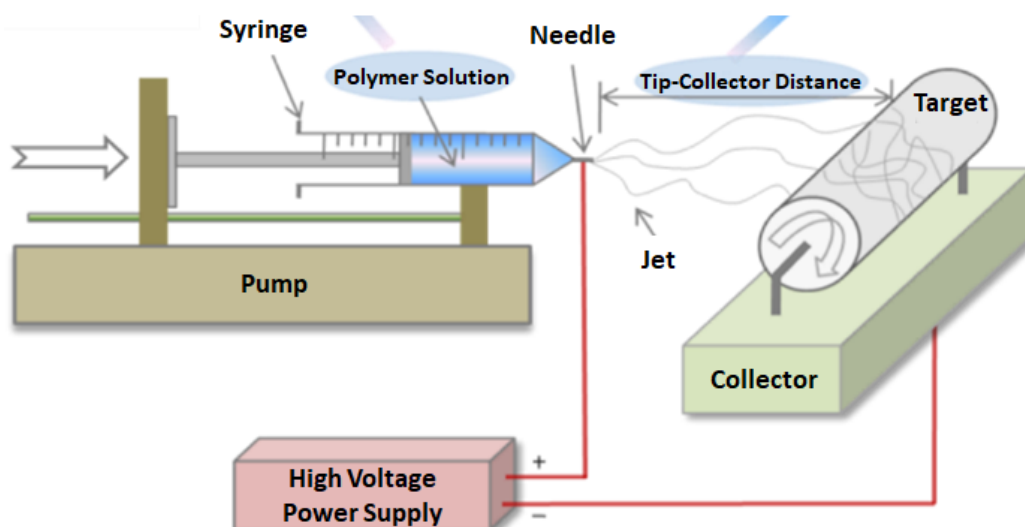


Figure 42 Schematic illustration of the experimental setup used for the nanofiber ES. Source: ORNL.

The recipes that were used for the nanofiber synthesis are described below.

Recipe 1. Fiber synthesis using water and acetic acid

In this recipe, water and acetic acid were used as solvents. No organic solvent such as DMF was employed. A solution was made by dissolving 0.465 g zirconium nitrate, 0.535 g lithium nitrate, and 1.29 g of lanthanum nitrate in 25 mL water. The reactants were mixed overnight, and this solution was named as SOLUTION 1. Then, 1.5 g of polyvinylpyrrolidone (PVP; MW: 1,300,000) was dissolved in 8.5 mL of acetic acid using magnetic stirring overnight, and this solution was named as SOLUTION 2. Equal volumetric amounts of SOLUTION 1 and SOLUTION 2 were mixed for 12 hours before ES (feed rate: 0.16 mL/hour, voltage: 18 kV; distance: 13 cm) on an inhouse ES instrument. The SEM image in Figure 45 shows thin and uniform nanofibers with a diameter 50 to 100 nm.

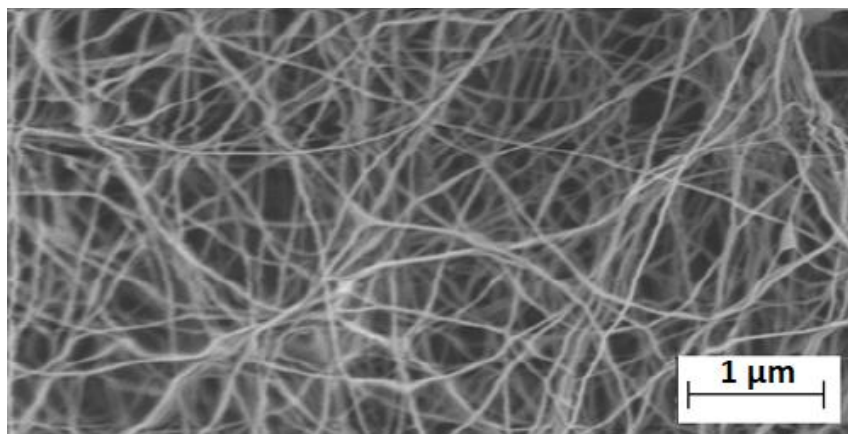


Figure 43 SEM image of electrospun LLZO nanofibers according to recipe 1. Source: ORNL

Recipe 2. Fiber synthesis using DMF and acetic acid

In this recipe, DMF and acetic acid were used as solvents and no water. A solution was made by dissolving 0.665 g zirconium isopropoxide complex, 0.535 g lithium nitrate, and 1.29 g of lanthanum nitrate in 10 mL DMF and 2 mL acetic acid solution. The reactants were mixed overnight. This solution was named SOLUTION 1. Then, 1.5 g of PVP (MW; 1,300,000) was dissolved in 8.5 mL of acetic acid by using magnetic stirring overnight. This solution was named SOLUTION 2. Equal volumetric amounts of SOLUTION 1 and SOLUTION 2 were mixed for 12 hours before ES (feed rate: 0.16 mL/hour, Voltage: 10 kV; distance: 15 cm) on an inhouse ES instrument. The SEM image in Figure 44 shows thicker nanofibers with a larger diameter (100-300 nm).

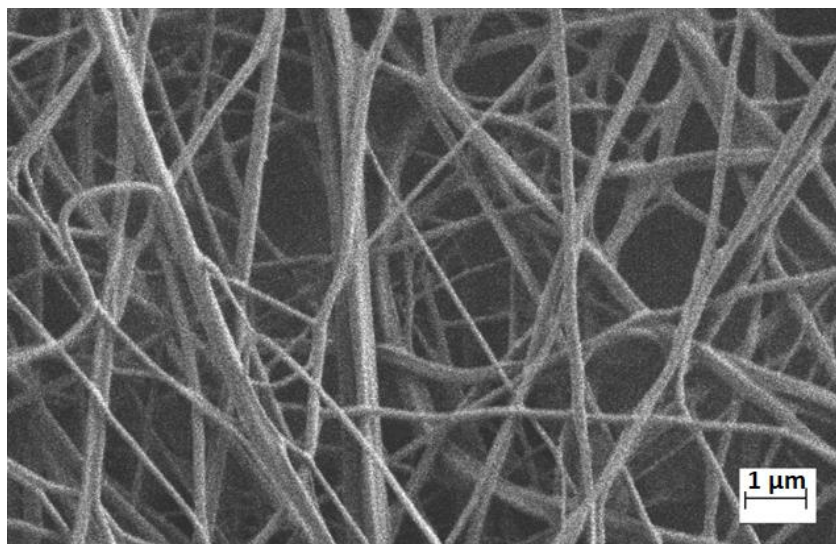


Figure 44 SEM image of electrospun LLZO nanofibers according to recipe 2. Source: ORNL

Recipe 3. Fiber synthesis using DMF and acetic acid at higher feed rate and higher voltage

In this recipe, solutions were prepared using the conditions employed in Recipe 2. However, the solution feed rate (1.38 mL/h) and the applied voltage were very high (18 kV) at a working distance of 15 cm. The obtained fibers were very thick (diameter: 1-5 μm) as shown in Figure 45.

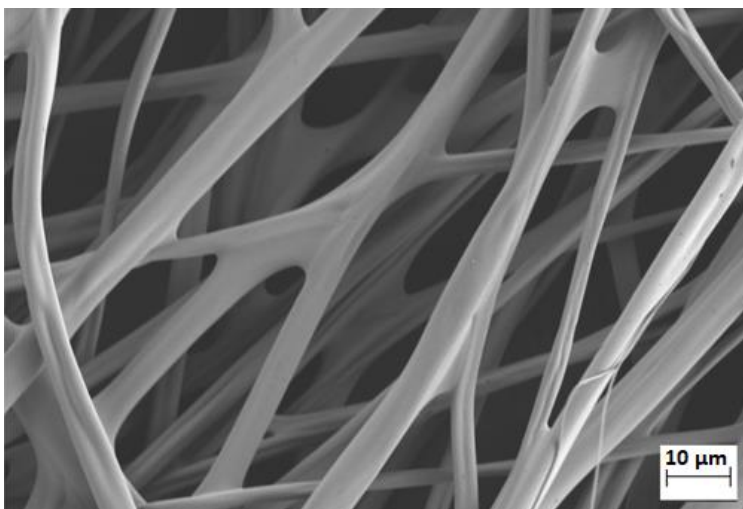


Figure 45 SEM image of electrospun LLZO nanofibers according to recipe 3. Source: ORNL

The aqueous conditions (Recipe 1) provided structurally sound, thin fibers and the use of organic solvents resulted in thicker fibers. The fiber diameter also depends on the feed rate (a higher feed rate provided thicker fibers). The synthesized nanofibers were annealed to remove the polymer phase. XRD measurements were performed to confirm the LLZO crystal structure.

Electrospun LLZO nanofibers were annealed at 700°C for 2 hours and XRD measurements were performed to confirm the LLZO crystal structure. The structure of the annealed fibers was confirmed to be a mixture of cubic and tetragonal phase LLZO. The XRD plot is shown in Figure 46 where the blue squares correspond to the cubic phase and the green squares correspond to the tetragonal phase. A detailed investigation of the LLZO crystal structure as a function of the annealing temperature continued.

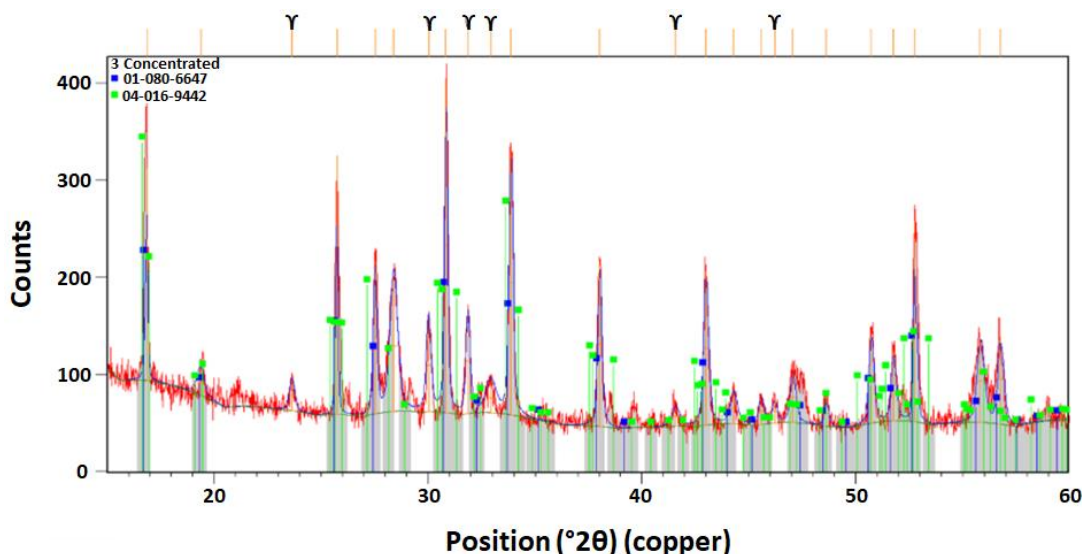


Figure 46 XRD plot of the annealed LLZO nanofibers. Source: ORNL

Polyacrylonitrile (PAN) was dissolved in DMF. The solution was electrospun to produce PAN nanofibers. Two recipes were followed. The experimental conditions are shown below.

Recipe 1:

PAN MW 150,000 was dissolved in DMF (10 wt% solution)

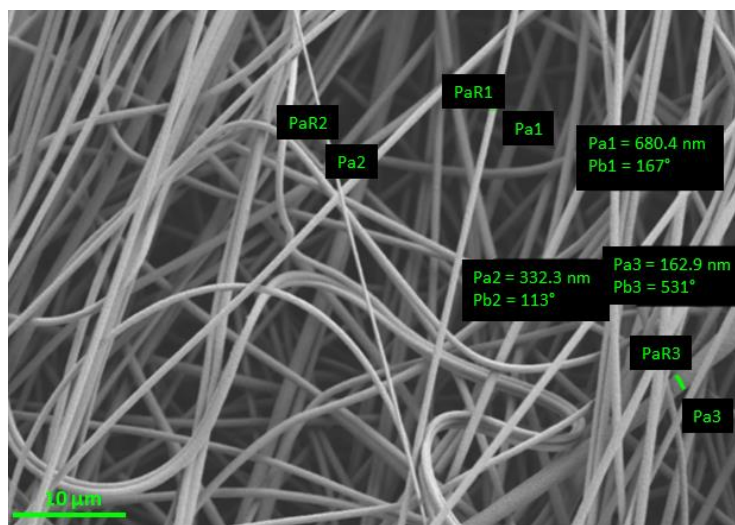
ES conditions: Needle diameter: 0.6 mm, rate 1.0 ml/h, distance: 12 cm, voltage: 18 kV

Recipe 2:

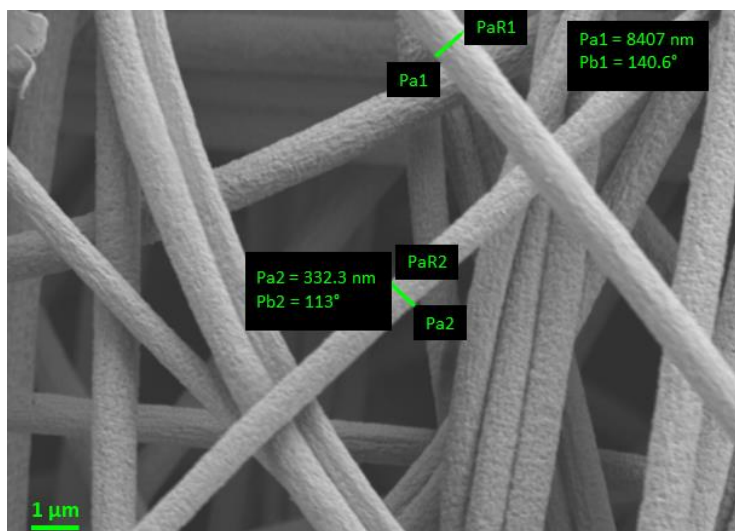
PAN MW 150,000 was dissolved in DMF (7 wt% solution)

ES conditions: Needle diameter: 0.6 mm, rate 0.5 ml/h, distance: 12 cm, voltage: 18 kV

SEM images of the PAN nanofibers are shown in Figure 47 and Figure 48. The fibers produced with the second recipe were thinner and their diameter was approximately 400-500 nm. LLZO and PAN was co-spun at different coaxial configurations and the coaxial fibers were annealed to produce carbon-fiber/LLZO composite and flexible nanofibers.

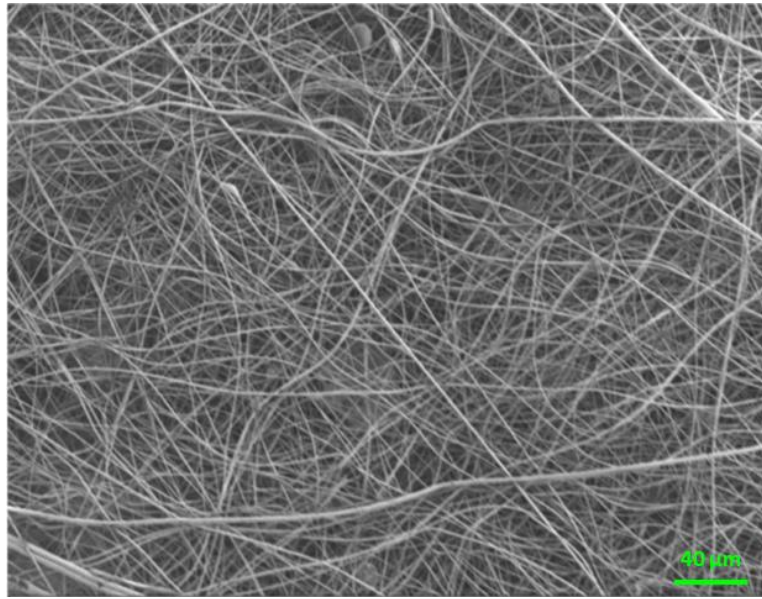


(a)

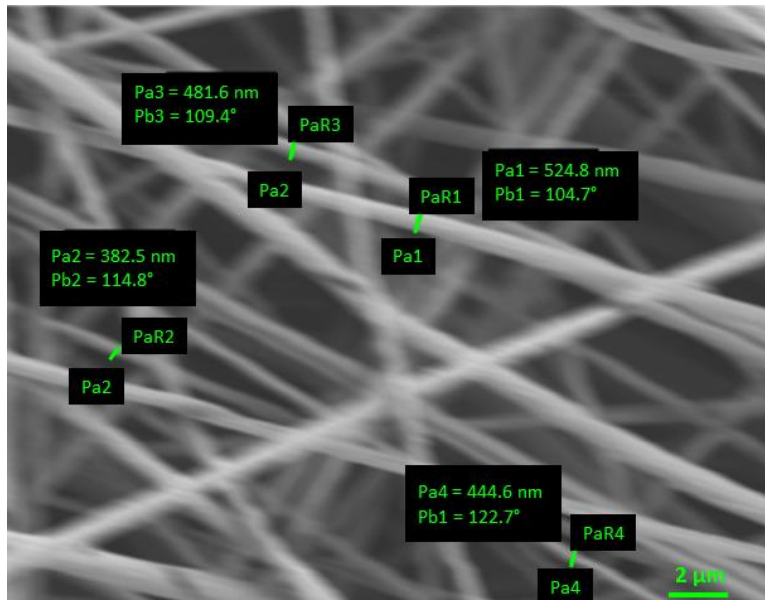


(b)

Figure 47 (a) Electrospun PAN fibers from Recipe 1 and (b) 10X magnification. Source: ORNL



(a)



(b)

Figure 48 (a) Electrospun PAN fibers according to recipe 2 and (b) at 20x magnification. Source: ORNL

ORNL synthesized PAN nanofibers using ES techniques. The PAN nanofibers were carbonized and converted them into carbon nanofibers. The final objective is to synthesize hybrid carbon nanofibers with LLZO. The LLZO nanofibers are very brittle and, therefore, it is difficult to synthesize and scale flexible LLZO nanofiber substrates. The carbon nanofibers can potentially provide a flexible and electrically conductive substrate (mat) that can host the brittle LLZO phase. The experimental setup that was developed by ORNL to carbonize the PAN fibers is shown in Figure 49. Air and argon gas can flow through the tube furnace at controlled flow rates. The annealing temperature and the heating rate can also be controlled. The setup was in a fume hood.

Carbon nanofibers were synthesized in a two-step process (stabilization and carbonization). The experimental parameters are as follows:

- PAN stabilization at 280 °C for 3h (air flow 2 L/min, rate 5 °C/min)
- Carbonization at 700 °C for 1 h and 1100 °C for 1h (argon flow 2 L/min, rate 20 °C/min)

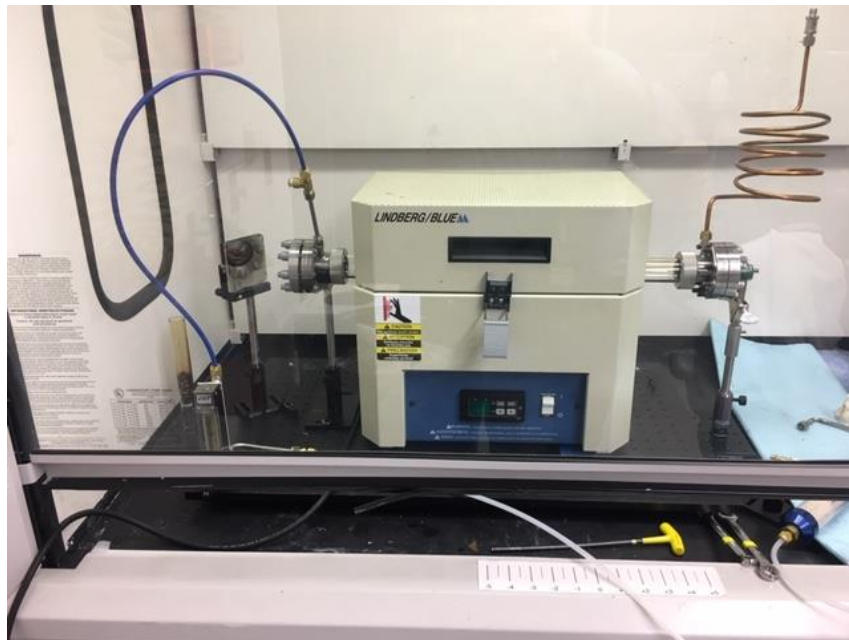
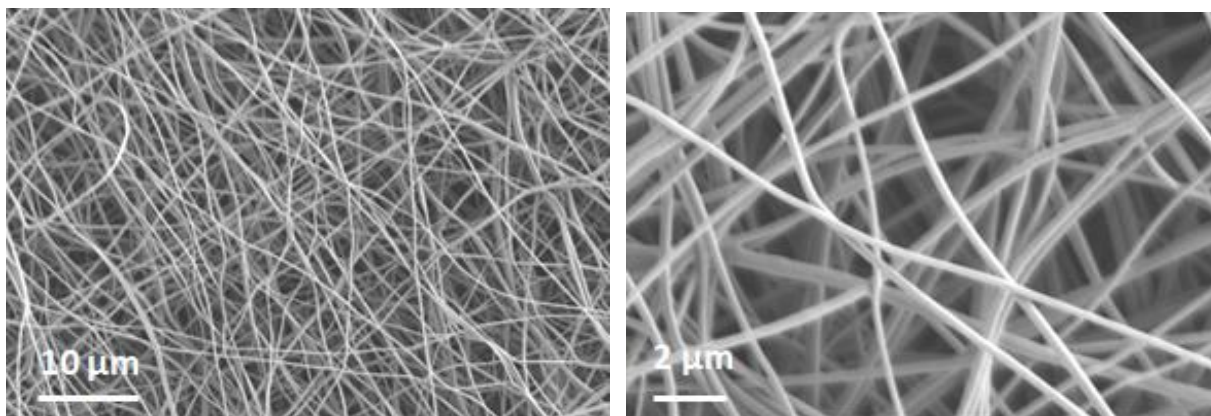


Figure 49 Carbonization setup that was used to carbonize the PAN fibers. Source: ORNL

The synthesized carbon nanofibers are shown in the SEM images in Figure 50. Their thickness is 200-300 nm. The carbon nanofiber mat is flexible and conductive. The two-point resistance is approximately 30 Ohms.



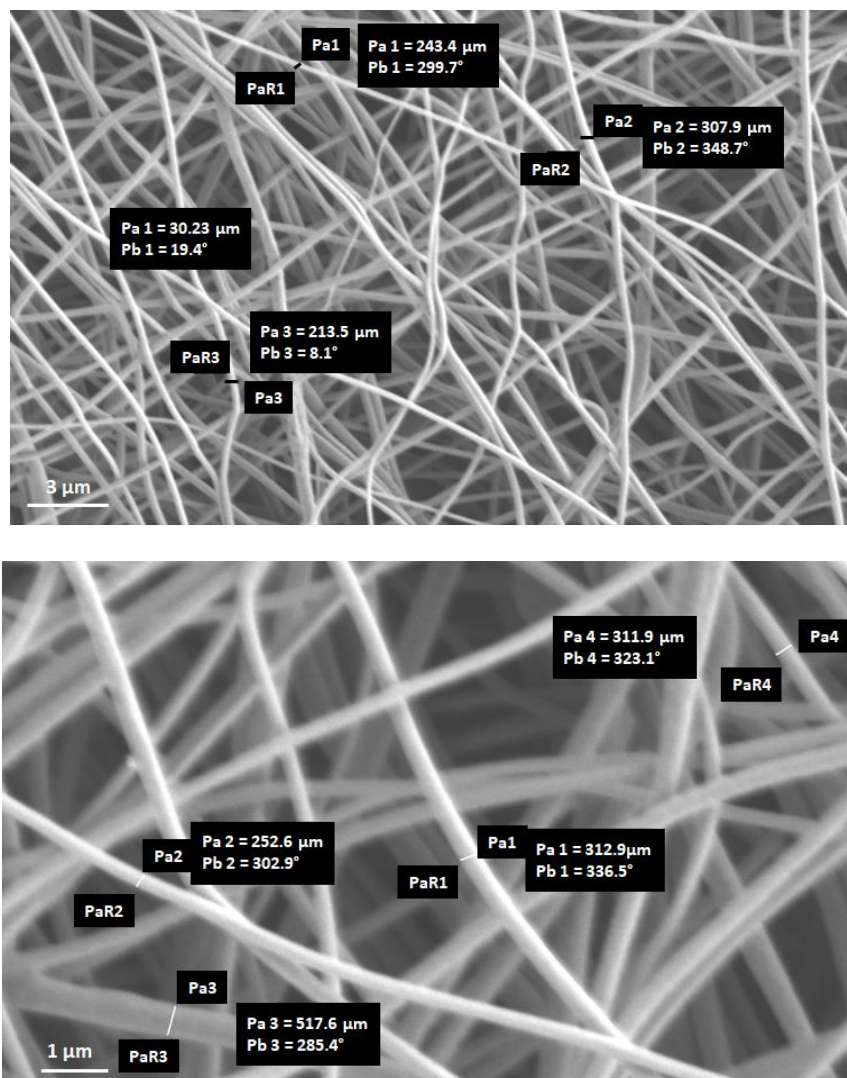


Figure 50 SEM images of the synthesized carbon nanofibers with diameters of 200-300 nm. Source: ORNL

LLZO nanofibers were synthesized in c-LLZO because the cubic phase is several orders of magnitude more conductive than the tetragonal phase. The synthesized LLZO nanofibers were doped with aluminum to stabilize the cubic phase. The sol-gel synthesis and ES parameters are presented below:

Stoichiometry of the sol-gel precursors:

Zirconium propoxide: 2 mmol
 Lithium nitrate: 7.7 mmol
 Lanthanum(III) nitrate hexahydrate: 3 mmol
 Aluminum nitrate nonahydrate: 0.27mmol

ES procedure:

The LLZO precursors were mixed overnight. Then aluminum nitrate nonahydrate was added and mixed for 6h. The polymer solution was added and mixed overnight.

ES conditions: Needle diameter: 0.6 mm, Rate 0.16 ml/h, Voltage: 14 kV, Collector speed: 400 rpm.

SEM images of the Al-LLZO nanofibers after the ES and prior to their annealing are shown in Figure 51. Their thickness is approximately 200 nm.

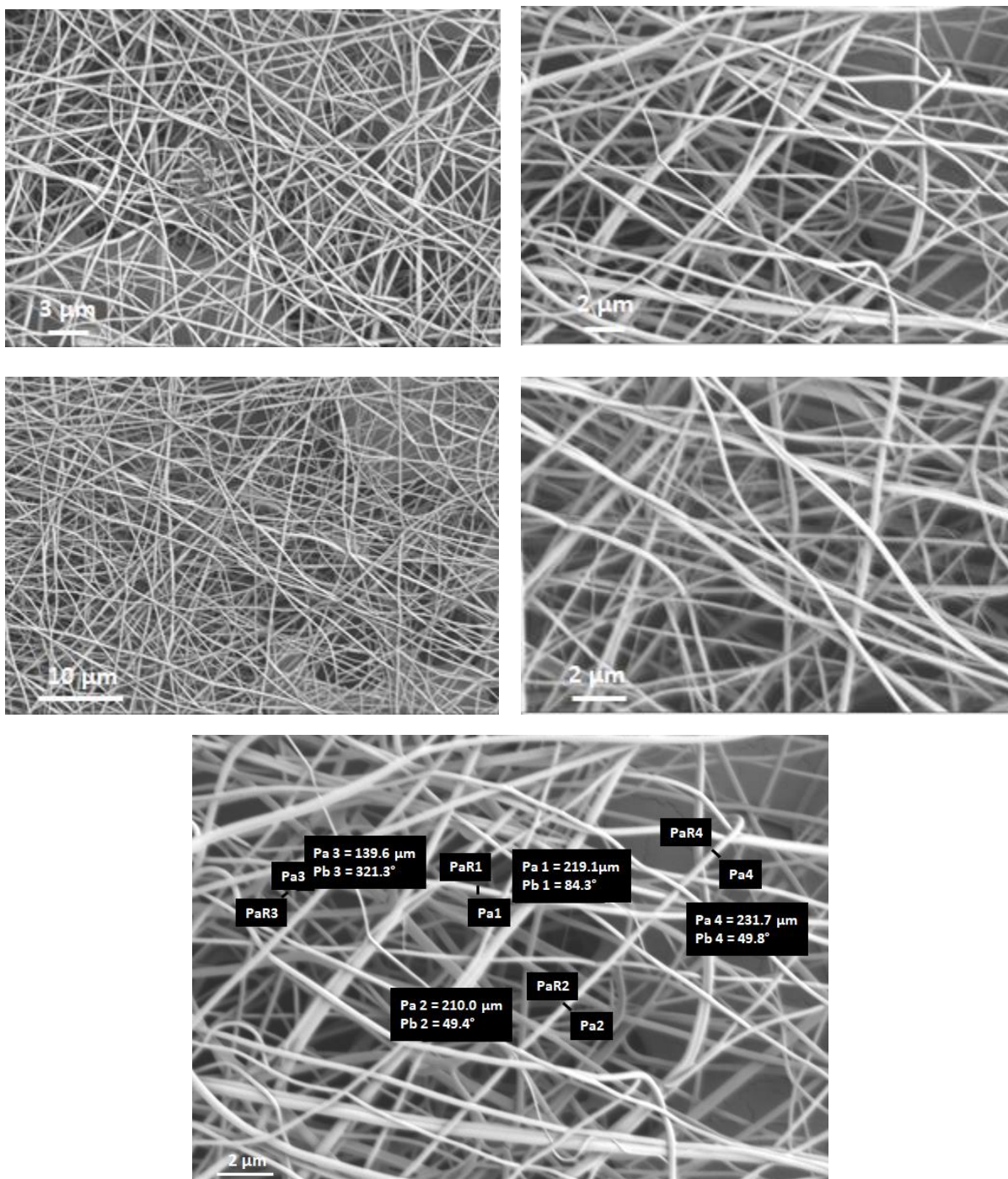
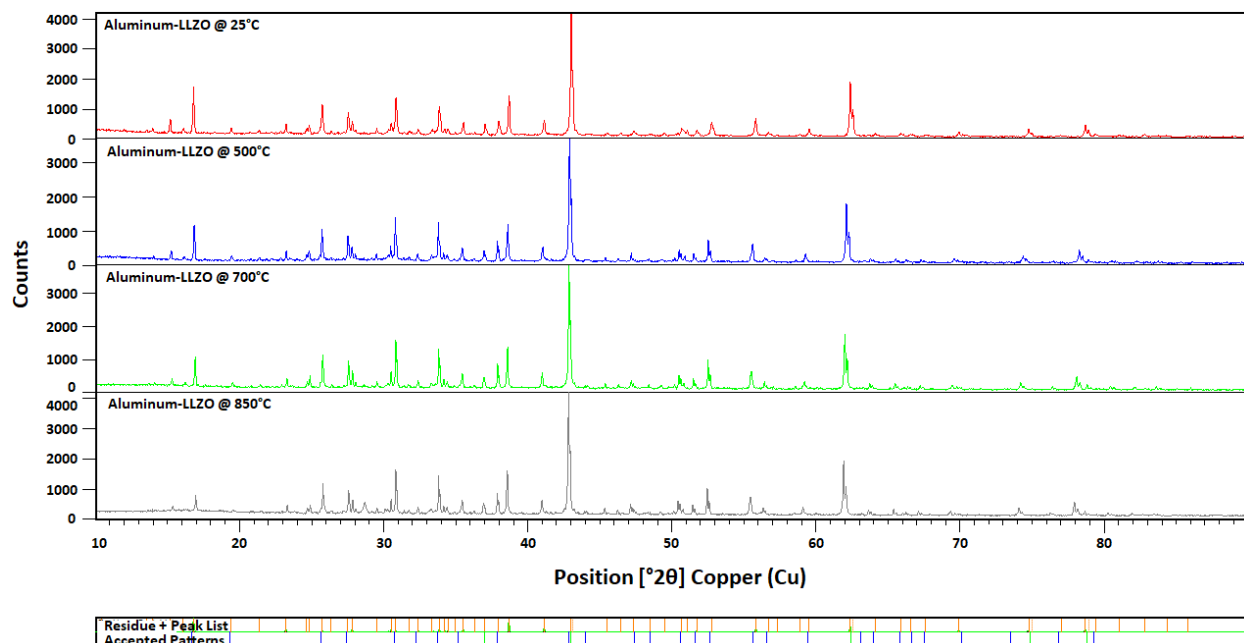


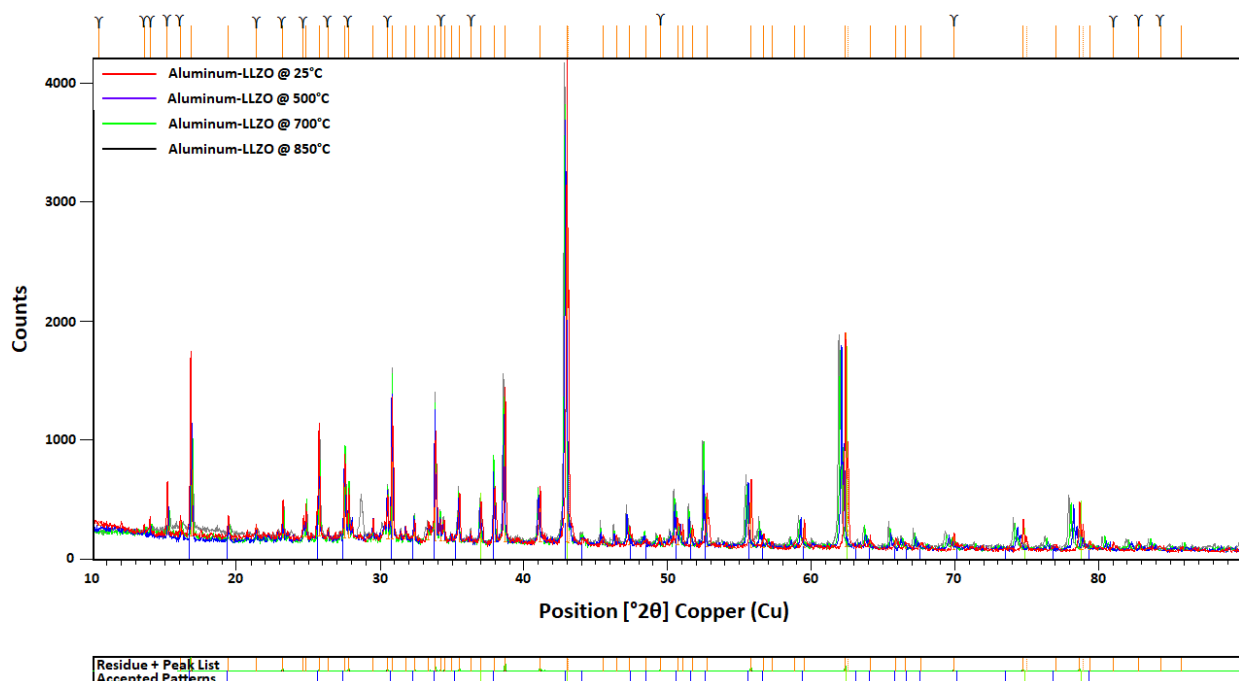
Figure 51 SEM images of the aluminum-LLZO nanofibers prior to their annealing with a diameter of approximately 200 nm. Source: ORNL

The aluminum-LLZO nanofibers were annealed at 700°C for 2 h to remove the polymer (PVP) that was used in the ES experiments. XRD measurements were performed on the aluminum-LLZO powder at several temperatures and the spectra is shown in Figure 52 (a) and the peak assignments are given in Figure 52 (b). The aluminum-LLZO powder was mixed with MgO powder to fill the XRD sample holder. The aluminum-LLZO is in the cubic phase for the measured temperatures of 25°C, 500°C, 700°C and 850°C. Additional peaks

due to impurities or unreacted materials are also present in the spectra. The spectra at different temperatures are overlapped to determine if there are any phase changes. The overlapped spectra are identical. The cubic phase is stable at the measured temperatures.



(a)



(b)

Figure 52 (a) XRD of the aluminum-LLZO powder mixed with MgO powder at several temperatures. (b) Peak assignment where the blue vertical lines correspond to the c-LLZO phase and the green vertical lines correspond to the MgO peaks.

Source: ORNL

Physics and Methodologies for Multilayer Coatings/Deposition; Fabrication and In Situ Testing of Prototype Components and Devices; and Novel Non-Destructive Evaluation, Quality Control and Metrology (NREL Lead Laboratory)

Cutting-Edge Coating and Deposition Science for R2R Applications

NREL performed a literature search, in coordination with SNL, on multilayer slide coatings and developed an initial set of guidelines elucidating required ink and substrate properties as well as process conditions for successful multilayer coating. Given the developed optimization guidelines, shear rheology studies were performed for three target inks to help optimize the inks by varying solids loading and solvent ratio in each ink. Figure 53 shows that, for example, solvent (nPA)-rich inks enable higher viscosity and lower limiting particle concentration, and thus are likely to be beneficial for simultaneous multi-layer coating.

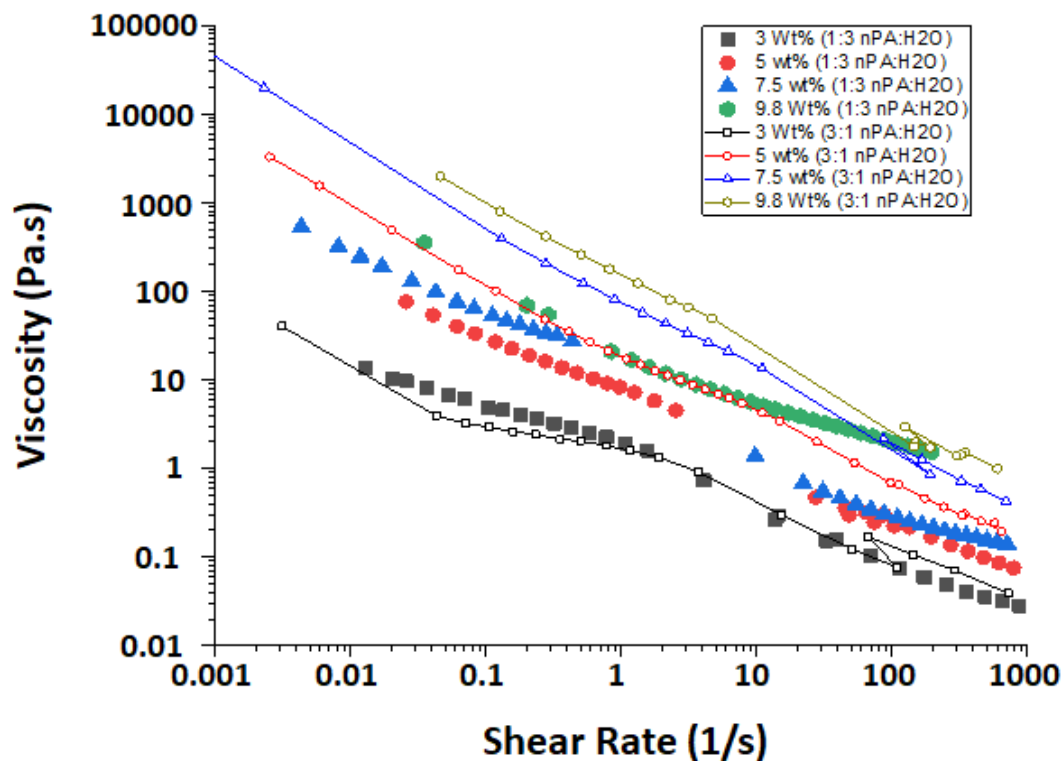


Figure 53 Heterogeneous ink rheology as a function of solids loading and solvent ratio. Source: NREL

The effect of catalyst wt% in ink was also studied to understand the level of flexibility of formulation needed for the developed set of ink guidelines. While the level of shear thinning behavior is different between the two cases, the viscosity is highly dependent on ionomer addition for both the 2 wt%, shown in Figure 54 (a), and 5 wt%, shown in Figure 54 (b), cases. The same result was observed with regards to solvent ratio in the ink (data not shown).

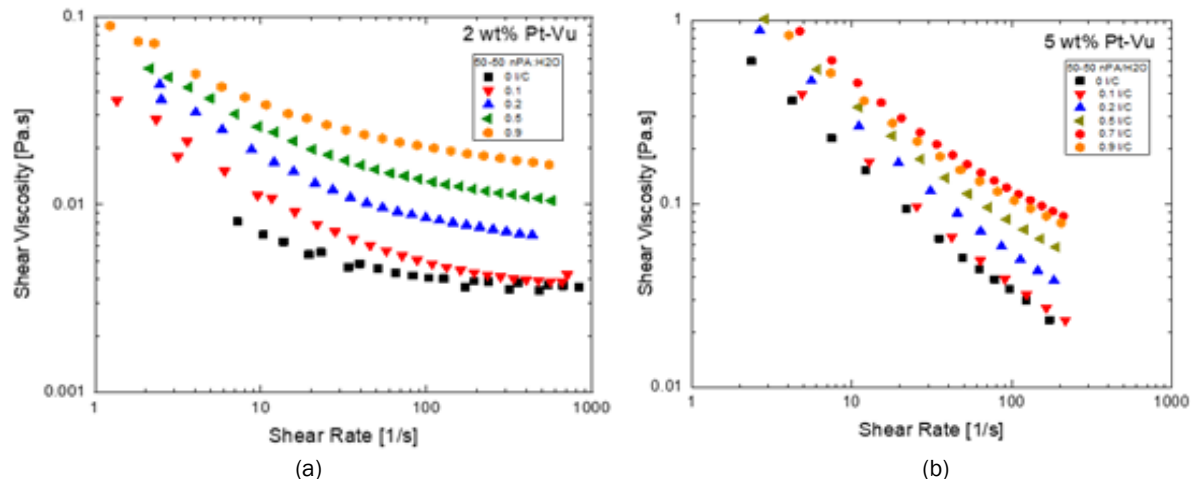


Figure 54 (a) 2 wt% and (b) 5 wt% catalyst ink rheology as a function of ionomer addition for 50:50 water-to-nPA solvent ratio. Source: NREL

Also based on the literature review, an initial empirical model was developed to begin to predict single- and multiple-layer wet thicknesses as a function of bottom layer (the layer in contact with the slide and the substrate) ink properties. This initial model enabled prediction of process windows for simultaneous coatings, taking into consideration ink properties. Figure 55 shows a process window analysis for a two-layer construction (i.e. membrane plus one electrode). Total dry thickness is plotted against total flow rate through the die, as a function of the angle of inclination of the slide. The total thickness is reasonable for the target membrane and one electrode. This empirical model also assisted coordination with SNL on parameters and focus areas for the slide die computational modeling effort.

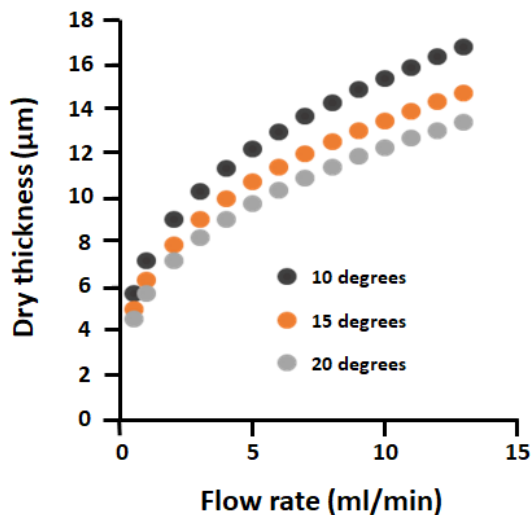


Figure 55 Results of empirical process window model for total dry thickness (assuming 5 wt% solids solutions) of a two-layer slide die coating as a function of flow rate. Source: NREL

The analytical multilayer slide coating process window model was further extended to include estimation of wet thickness for each coated layer. Figure 56 shows an analysis indicating, for the case of a 15-degree slide die incline, that the intended dry thicknesses of the three-layer target electrochemical cell configuration are solvable within the model, i.e. data should be within the process window.

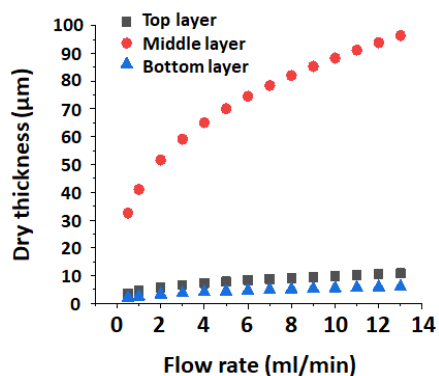


Figure 56 Target dry thickness validation of three-layer configuration using analytical slide die model. Source: NREL

To inform the analytical slide die model, an empirical model of the heterogeneous top and bottom layer inks was developed for the initial target construction using a Box-Behnken statistical design. The model includes ink solvent ratio, catalyst weight fraction, and ionomer-to-carbon ratio as factors, and density, surface tension and viscosity as the parameters of the model. For the catalyst on HSC support ink (the intended top layer), Figure 57 (a) and Figure 57 (b) show contour plots of the factor impacts for density and viscosity, respectively. The actual measurement data as well as the full quadratic model of the ink properties was provided to SNL for use in their slide die continuum model development and validation.

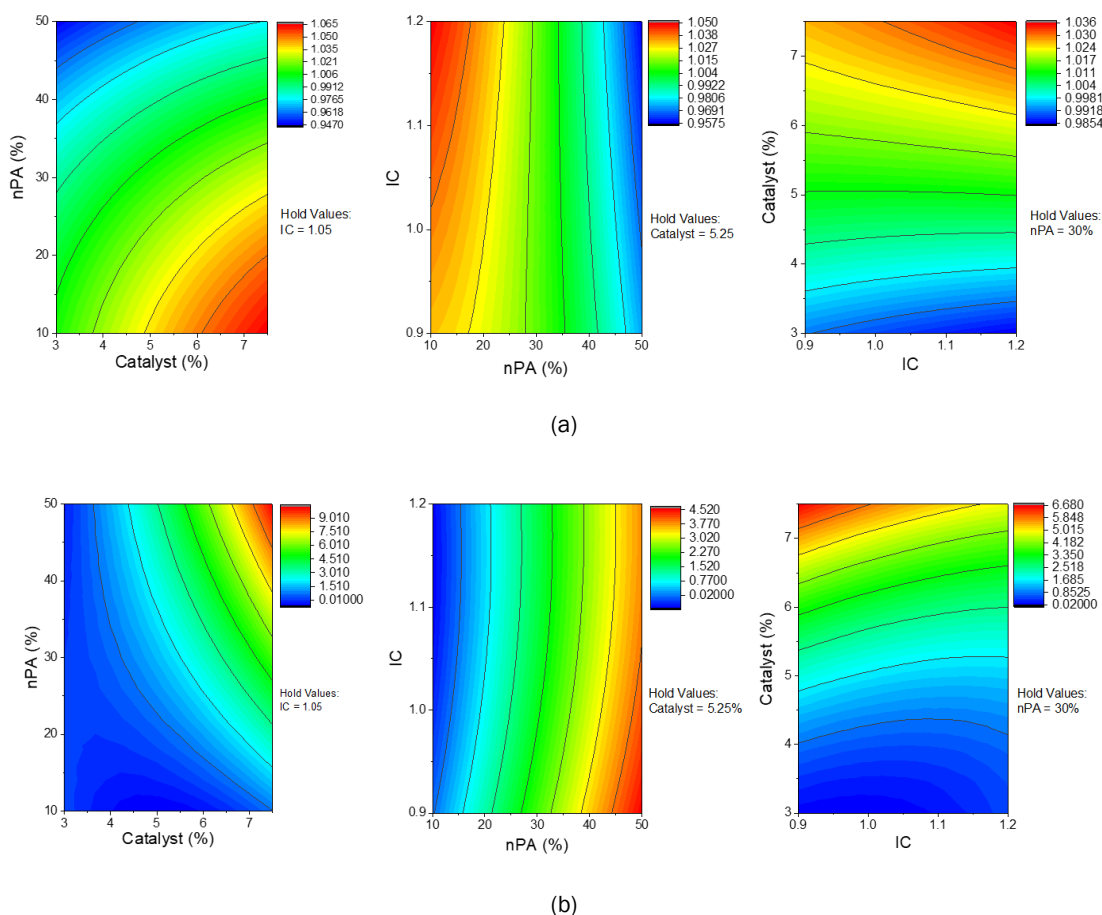
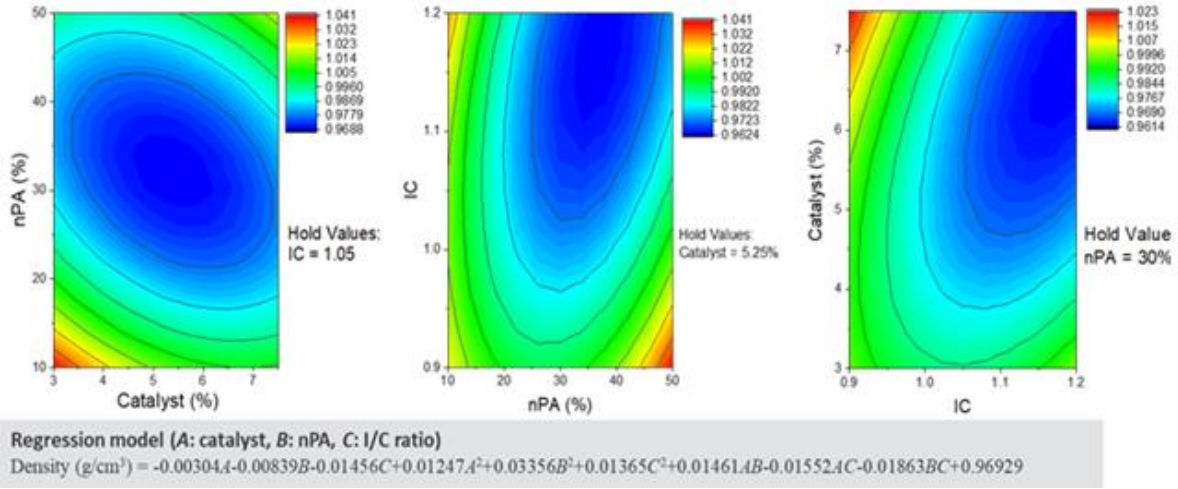
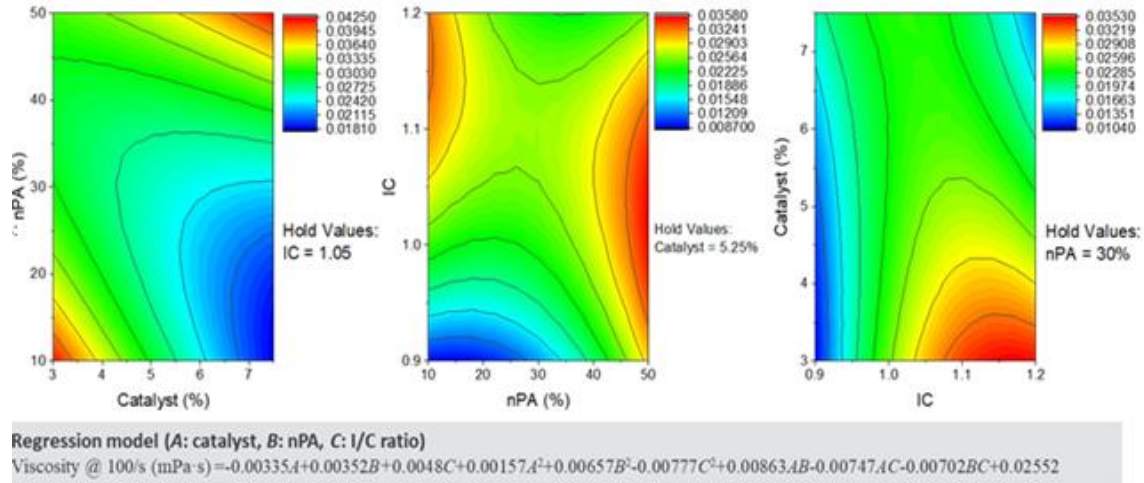


Figure 57 Factor impact contour plots for (a) the density and (b) the viscosity of the top layer ink. Source: NREL

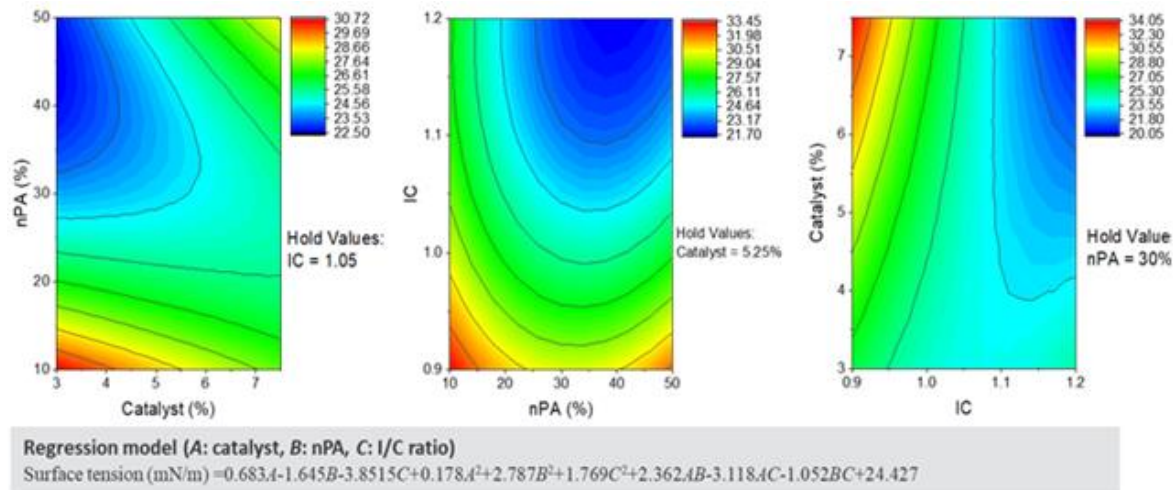
NREL also completed the empirical full-quadratic model for our target Pt/low-surface-area-carbon support (LSC) inks, based on a Box-Behnken design, and provided the model to SNL for further predictive modeling of our 2L and 3L slide die target structures. Figure 58 shows Pt/LSC quadratic model outputs for ink density, surface tension, and viscosity at shear rates of 1/s and 100/s.



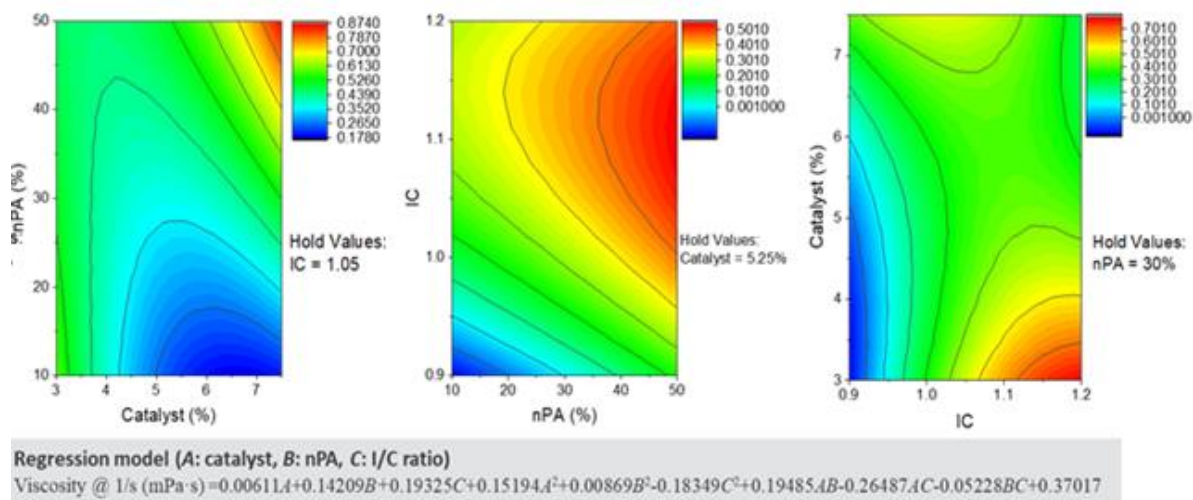
(a)



(b)



(c)



(d)

Figure 58 Pt/LSC quadratic model outputs for (a) ink density, (b) viscosity at shear rates of 1/s, (c) surface tension and (d) viscosity at shear rates of 100/s. Source: NREL

NREL performed blade coatings of single-layer membranes to support the initial target multi-layer coating construction (three-layer: electrode-membrane-electrode). The objective was to understand the efficacy of coated ionomer layers with respect to membrane functionality, in particular (initially), proton conductivity. Figure 59 (a) shows the estimated and measured dry thickness of the coated membranes as a function of the coating gap and the resulting proton conductivity for Nafion 211 and four test samples in Figure 59 (b). The thicknesses are within the intended range for several electrochemical applications. The conductivities of the cast membranes are within a reasonable range of the commercially available comparator case (Nafion).

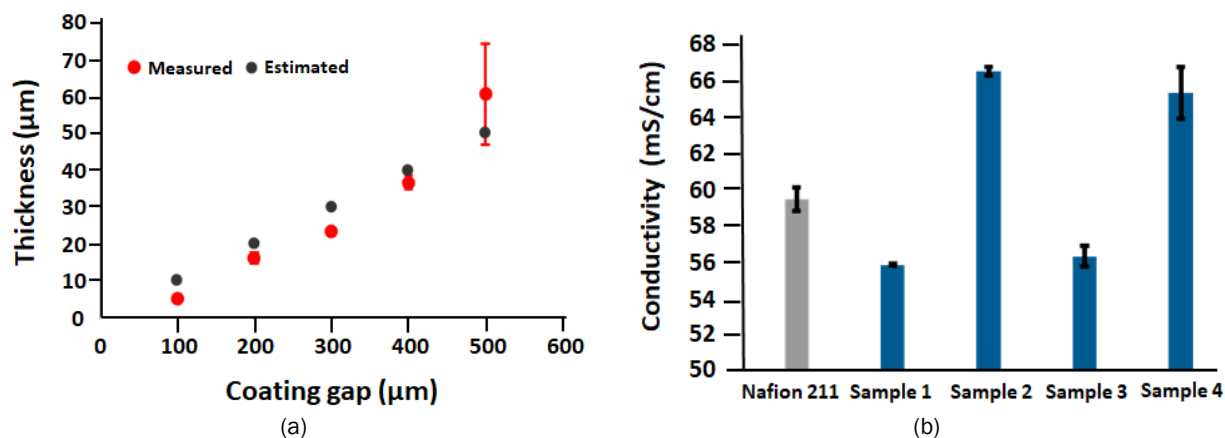


Figure 59 (a) Cast membrane thickness as a function of coating gap and (b) proton conductivity of the cast membranes compared to a commercially available membrane. Source: NREL

To support the understanding of the potential implication of simultaneous two- and three-layer coatings on the performance of the target electrochemical cell construction, multilayer structures were simulated using ultrasonic spray coating. As described above, these are combinations of heterogeneous particle-polymer layers and polymer-only layers, as depicted in Figure 60 (a) for the intended 3-layer and two permutations of 2-layer structures, and in Figure 60 (b) the standard individual-layer constructions. Both two- and three-layer simulated multilayer structures were sprayed; however, issues with uniform spraying of the membrane (D2020 ionomer) layer were encountered, but were resolved, and in situ testing of the simulated multilayer structures was initiated.

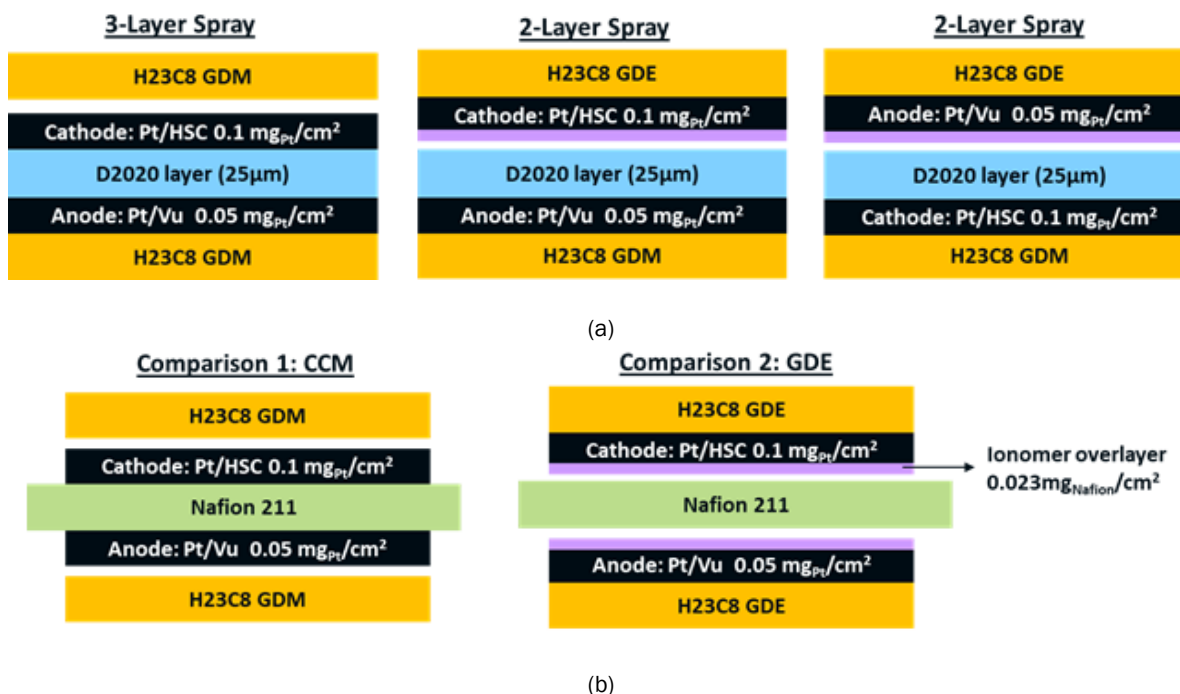


Figure 60 (a) Simulated multilayer structures via ultrasonic spray and (b) standard individual-layer structures. Source: NREL

In further preparation for initial slide die startup as well as broad application-agnostic process window studies, NREL initiated the formulation of “dummy inks” with widely tunable properties. Figures 61 (a) and (b) show that, with either carbon-only inks or polyethylene oxide (PEO) inks respectively, we can reasonably well

mimic the rheology of the much more expensive Pt catalyst and ionomer inks. This effort will also be beneficial as it will allow the use of much less expensive particles and polymers in the startup efforts.

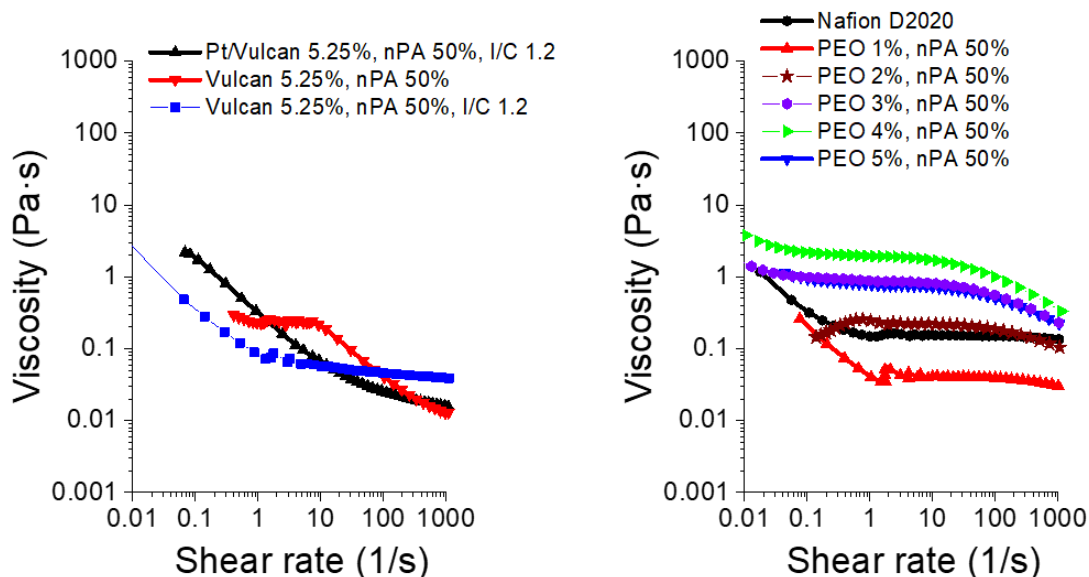


Figure 61 (a) Dummy ink rheology for catalyst ink and (b) ionomer solution (actual target inks in black). Source: NREL

During FY 2019, drawings for multilayer slide die equipment from U.S. supplier Allied Die were received and approved with significant design input from SNL. NREL proceeded to procure the slide die that is shown in the computer-aided design drawing in Figure 62. Delivery of the slide die was not expected until early in FY 2020. Simultaneously, the design and build of a cart to support the die when not in use (it weighs ~90 lbs.) and to lift it into the coating station was initiated. It was anticipated that a modified commercially-available heavy-duty cart would be used.

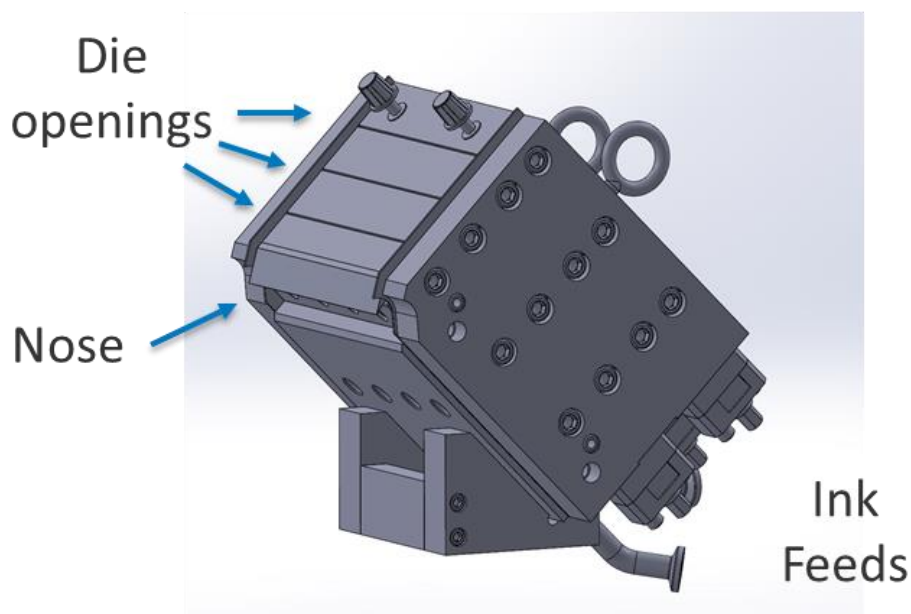


Figure 62 Computer-aided design drawing of 3-layer slide die from Allied Die. Source: NREL

In coordination with the ES focus area at ANL, NREL held several internal technical-review and planning meetings, leading to the development of an initial experimental plan which included the following three research areas: (1) a study of slurry properties and behaviors as a function of composition, (2) a study of ES process parameters to understand process windows for different slurries of interest, and (3) an application-based study that was initially focused on fabrication of electrospun PEM fuel cell electrodes using standard platinum-carbon catalysts to understand how process conditions relate to device performance. Within area (1) above, NREL performed initial rheology studies of ES slurries using PAA as the carrier polymer (a widely used ES carrier material). Two types of PAA slurries were studied – ionomer-only slurries, and slurries with both ionomer and catalyst particles. These particle/active polymer/carrier polymer systems are highly representative of slurries used in a broad range of ES applications. Figure 63 shows summary results from this steady-shear rheology study. While the ionomer/PAA slurries (open symbols) are all Newtonian across the range of PAA solids loadings, the ionomer/particle/PAA slurries (closed symbols) are all shear-thinning. This indicates a strong interaction between the PAA and particles.

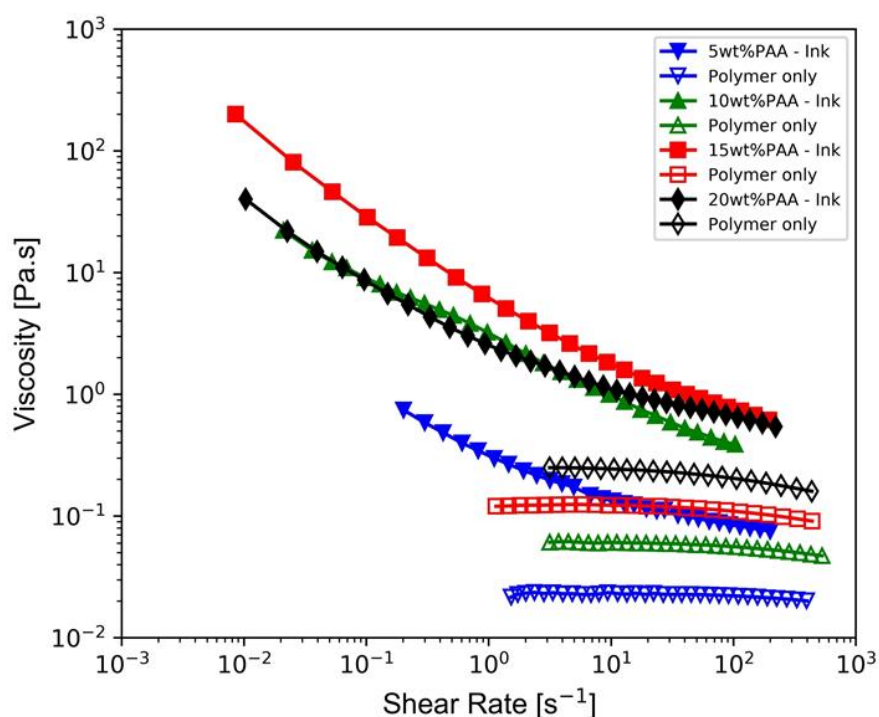


Figure 63 Steady-shear rheology of ionomer/PAA and ionomer/particle/PAA slurries over a PAA range of 5-20 wt%. Source: NREL

Additional steady (rotational) shear rheology characterization of carrier polymer (PAA), functional polymer (Nafion) and particle (catalyst on low-surface-area carbon) ES slurries was then performed. Amplitude and frequency sweep shear measurements were performed to understand the gelation behavior of these inks. Figure 64 gives amplitude sweep data for the full three-component slurry showing that at the highest solids loading of PAA, the slurry is liquid-like ($\tan\delta > 1$), but for lower solids loadings, the slurry is gel-like ($\tan\delta < 1$).

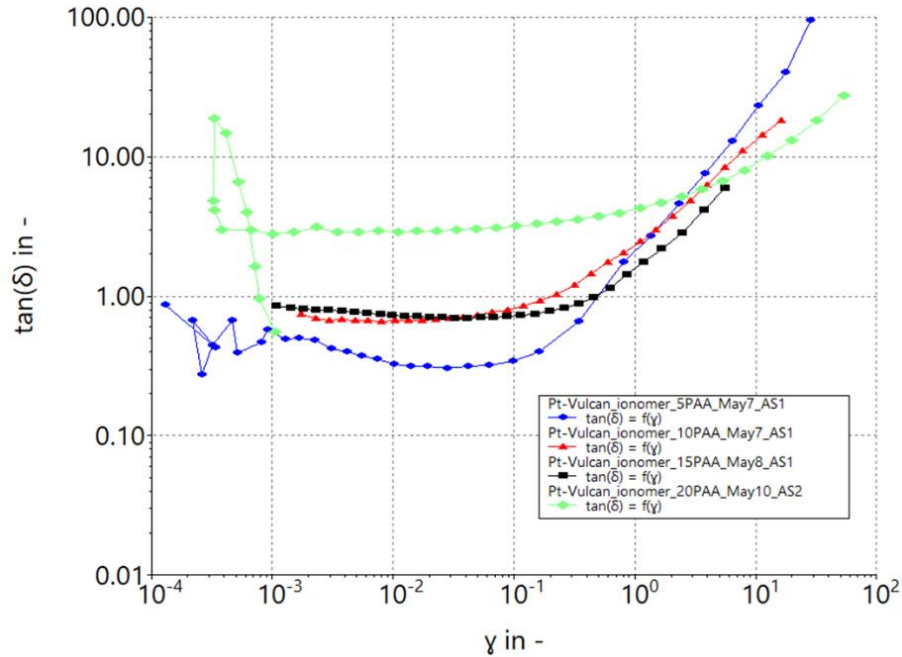


Figure 64 Amplitude sweep shear rheology data for carrier-ionomer-particle slurries as a function of carrier (PAA) solids loading from 5-20 wt%. Source: NREL

Leveraging NREL's collaboration with University of Massachusetts Amherst, extensional rheology was performed using the DoS-CaBER method, which is highly indicative of ES process physics. Figure 65 shows a comparison between extensional and shear rheology data for carrier-ionomer and carrier-ionomer-particle slurries. Of specific note is that the extensional viscosity data in Figure 65 (a) is much higher magnitude than the high-shear-rate shear viscosity data (right side of Figure 65 (b)) indicating the value of the extensional rheology in providing unique, process-relevant data for these slurries. The actual viscosity of the slurries is much higher during the spinning process than would be indicated by the high-shear region of the shear rheology data.

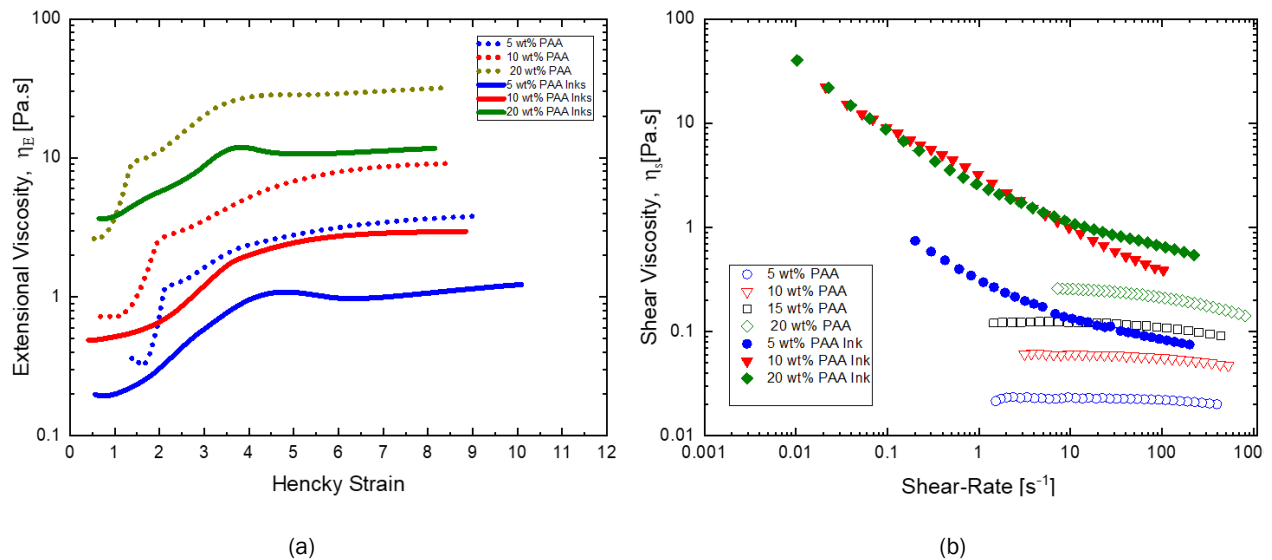


Figure 65 (a) Extensional viscosity and (b) shear viscosity data for carrier-ionomer and carrier-ionomer-particle slurries. Source: NREL

Subsequent to completion of maintenance and safety upgrades to NREL's small-scale ES station, we performed a PAA process window study. PAA was chosen because it is widely used as a carrier polymer in ES across many applications, but it is also the main carrier used in our small-scale PEMFC electrode ES effort. Thus, a broad study of PAA ES is useful generally to the community, but also forms a basis for further studies at NREL of full electrode inks for ES. For this study, the process conditions shown in Table IV were chosen based on our PEM electrode work using PAA as a carrier.

Table IV ES Process Conditions for PAA Process Window Study

Parameter	Value
Voltage	15 kV
Distance	10 cm
Humidity	35 – 40 % RH
Flow rate	0.5 ml/hr
Needle	22 gauge
Speed	100 rpm

Figure 66 shows a summary of resulting fiber diameter for the study as a function of PAA weight%, as measured by SEM where the expected profile was observed. Figure 67 shows a characterization of the observed process window. Interestingly, a multi-region window encompassing regions of no fibers ('spray coating'), fibers with beads, fibers with no or minimal beads, and, at high carrier concentrations, flow instabilities due to excessive viscosity of the ink can be observed. In this final region, Taylor cone instability was observed, as seen in the inset image along the right.

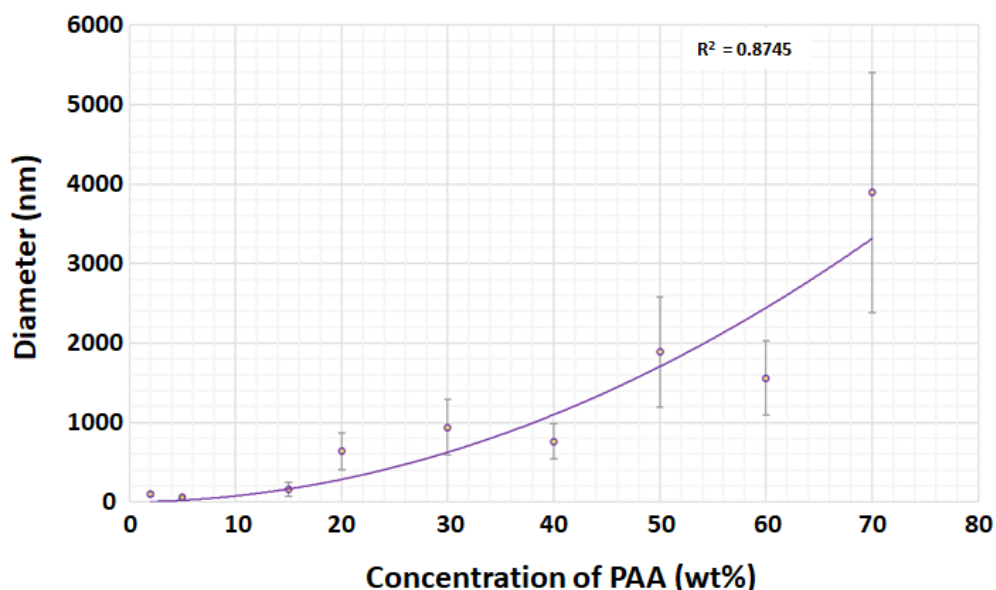


Figure 66 Summary of fiber diameter as a function of PAA concentration for the process window study. Source: NREL

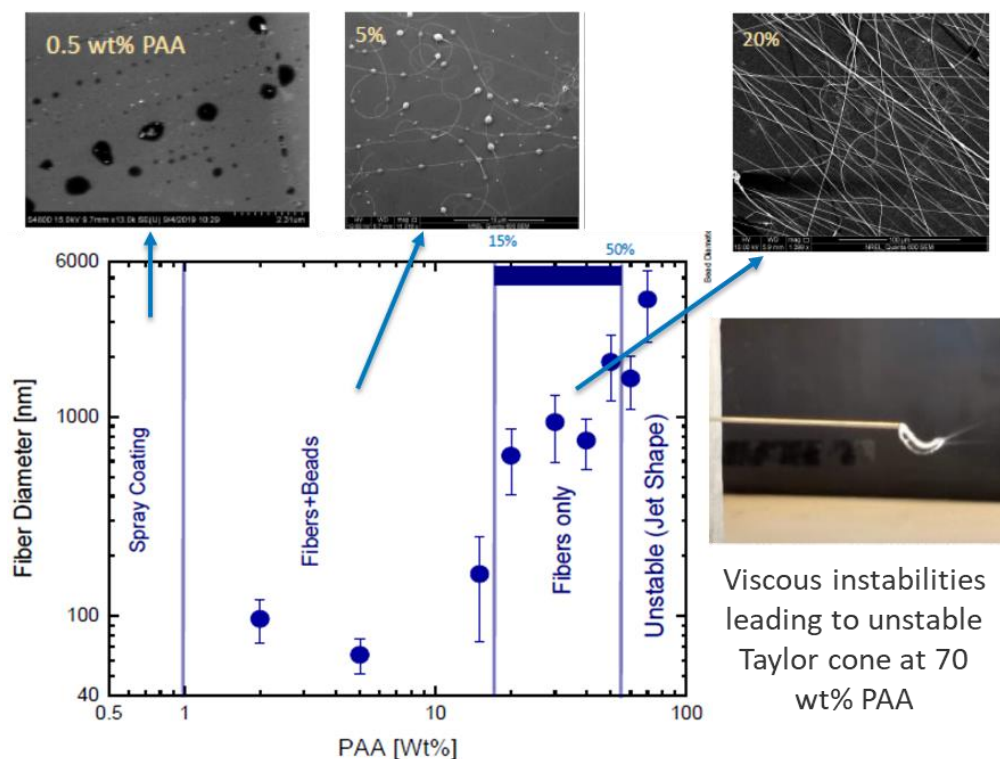


Figure 67 PAA spinning process window depiction; inset images show examples of droplets (no fibers), spinning mostly beads, and spinning good fibers, as well as viscous instability of the Taylor cone at high PAA wt%. Source: NREL

In addition, an initial process window study was performed on a full electrode ink (PAA + ionomer + catalyst particles). As depicted in Figure 68, sprayed droplets at 5 wt% PAA in the ink, spinning of fibers at 10 wt% PAA although the fibers had poor strength and were not continuous, spinning of good fibers at 15 wt% PAA with some beads (this is the standard condition for electrode spinning and testing) and larger fibers with more beads at 20 wt% PAA with some fiber agglomeration can all be observed. Given the addition of particles and a volume fraction of a polymer (the ionomer) that has much less propensity to entangle compared to the carrier polymer, the narrowing of the process window (compared to the PAA only case) was expected.

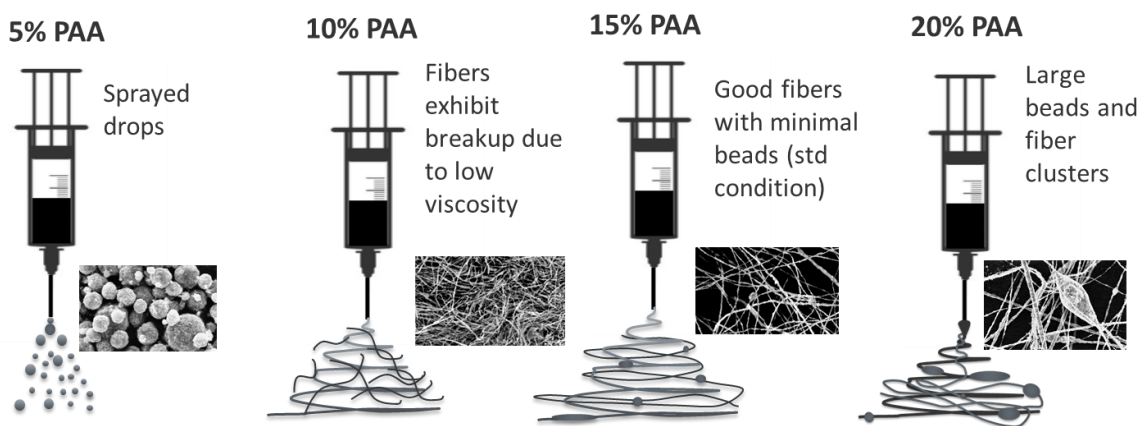


Figure 68 Full PEM electrode ink process window depiction with SEM insets showing resulting materials. Source: NREL

Fabrication and In Situ Testing of Prototype Components and Devices

A study of spray-coated multilayer cell structures was initiated in hopes of understanding interfacial behaviors relevant to our eventual multilayer slide die coated structures, as described above. Unfortunately, overall, poor performance of cells fabricated with these structures was observed including low open circuit voltage (OCV) and high hydrogen crossover. Based on surface microscopy, this may be due to poor uniformity of the sprayed membrane layer. Figure 69 (a) shows the poor polarization performance of two of the multilayer sprayed cells and Figure 69 (b) is an image from optical microscopy of the sprayed membrane.

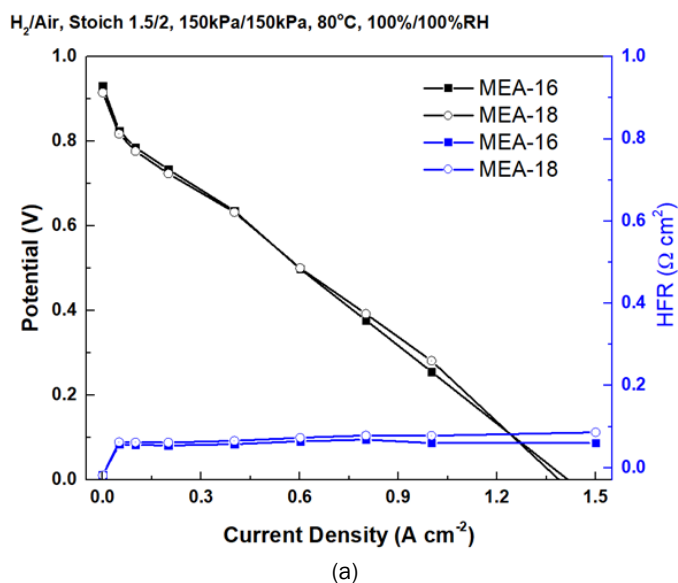


Figure 69 (a) Polarization performance of two multilayer sprayed cells (for comparison, performance should be at least 0.8 A/cm² at 0.6 volts) and (b) optical microscopy of the sprayed membrane layer. Source: NREL

However, a positive result was obtained. This was the confirmation of a new cell sealing methodology for simultaneous-coated constructions that do not have a membrane surface area larger than the active (catalyst) area for sealing, which is the typically used methodology. Figure 70 (a) shows an example of the typical cell

build (in this case for a catalyst coated membrane), with extended surfaces of the membrane for sealing, and Figure 70 (b) shows the newly validated methodology wherein one electrode of the simultaneous three-layer coated target structure is used as the sealing surface with a slightly smaller piece of gas-diffusion media (GDM) on that side of the cell. The red and brown elements along the edges depict a two-part gasketing scheme. This latter scheme will be used to support in situ testing of simultaneous multilayer cell structures.

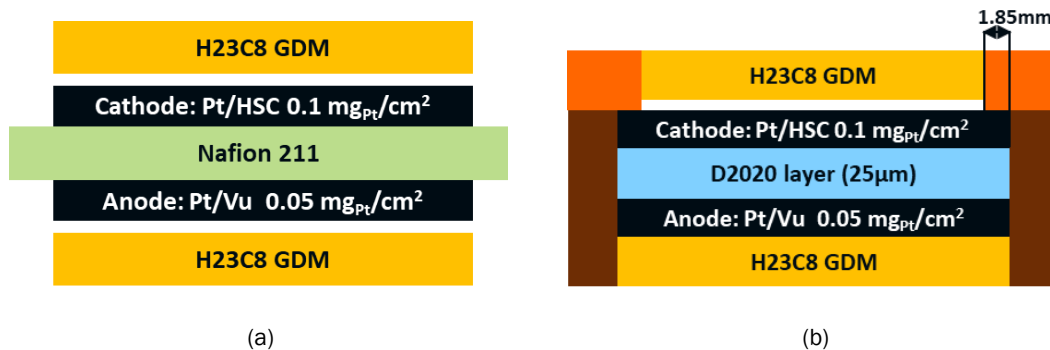


Figure 70 (a) Typical catalyst coated membrane cell structure with membrane (Nafion 211) sealing area and (b) the new structure for three-layer target construction (Cathode-D2020-Anode). Source: NREL

In addition, NREL performed in situ testing of two sets of R2R GDE samples from ORNL. The performance of the first set was less than typical, but good enough to advise ORNL to continue their coating work. However, the cells from the second ORNL coating run had lower than expected performance given the catalyst loading, even with an added ionomer overlayer as shown by the performance data in Figure 71 (a). In particular, mass activity – as evidenced by the poor kinetic polarization performance – and electrochemical surface area were low. Figure 71 (b) shows that the ORNL cell performance was lower than the NREL R2R GDE comparison cases in the kinetic, ohmic, and mass transport regions. This was the case even though the ORNL GDEs had higher catalyst loading. Surface SEM performed at ORNL appeared to show a high level of particle agglomeration in the coated electrode, which correlates to the low mass activity and electrochemical surface area. As a result, ORNL continued to study their ink dispersion methods.

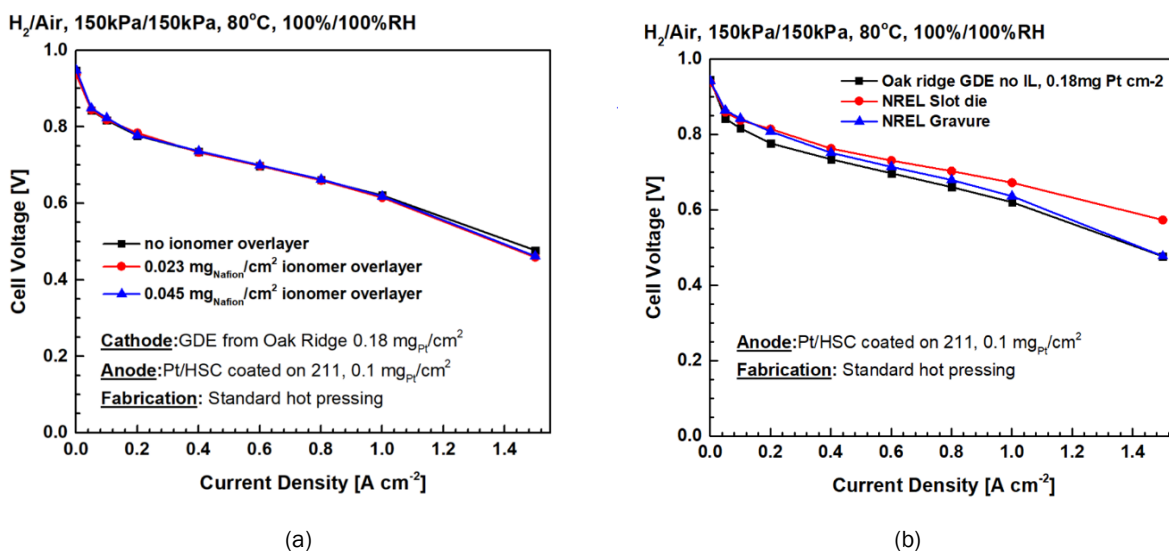


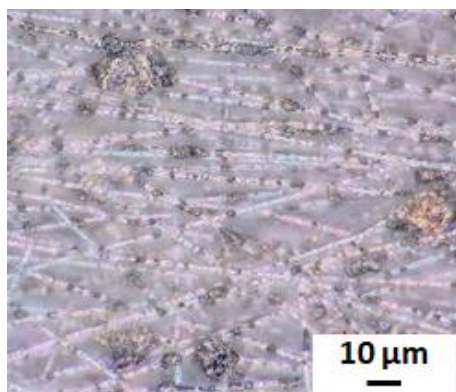
Figure 71 (a) Polarization performance of the ORNL cell without and with ionomer overlayer, and (b) ORNL cells compared to NREL R2R GDE cells. Source: ORNL

Novel NDE, QC, and Metrology Methods

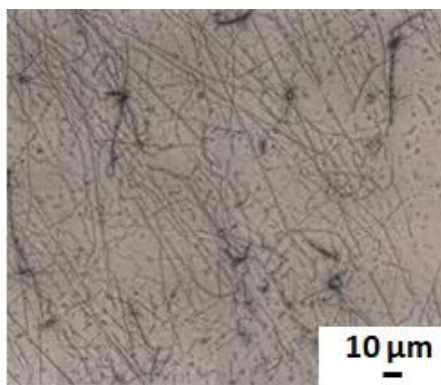
NREL performed several experiments to demonstrate real-time NDE technology applicable to multilayer electrochemical cell materials that culminated in an experiment of many single- and multilayer membrane webs on the NREL metrology web-line using multi-spectral imaging. These experiments included energy conversion membranes as well as commercial barrier films. Multilayer constructions (e.g. constructions with a protective layer, a functional layer, and a casting liner) were run at different line speeds and the thickness of each layer was imaged in the cross- and down-web directions to start to understand the parameter impact of speed on down-web resolution.

Associated with the development of in-line membrane thickness imaging techniques for multilayer films and in collaboration with the NREL High Performance Computing group, NREL developed an algorithm that enabled a processing time improvement of up to 165x (compared to the original software) of massive hyperspectral cube videos. The technique leverages the parallel computing capabilities of graphics processing units (graphics cards), rather than using standard central processing units. A software record was submitted for the development.

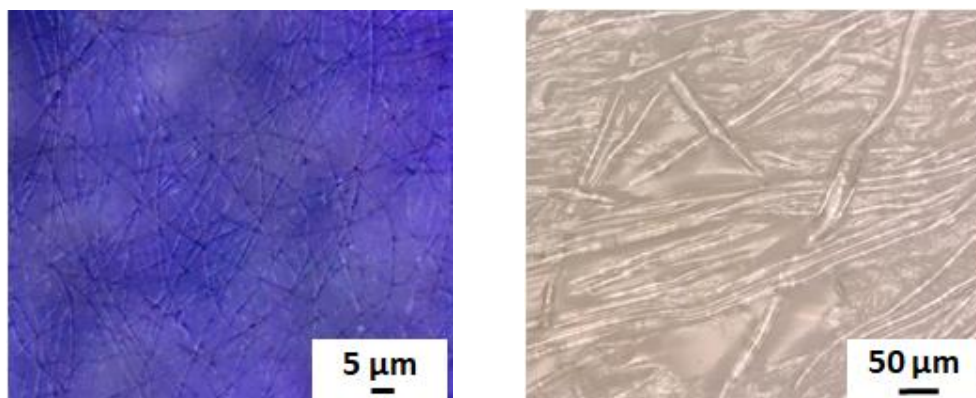
NREL purchased commercially available reverse osmosis membranes to assist in its exploratory effort to evaluate materials and methods for in-line inspection of ES and multilayer structures. These are multi-layer/multi-functional membranes relevant to AMO's strong emphasis on advancing manufacturing technologies for water processing. Using these membranes, as well as ES membrane and electrode mats fabricated at NREL, initial microscopy studies were performed to characterize the thickness, porosity, layer interfaces, and other properties to inform our plan for development of relevant in-line methods. Figure 72 shows optical microscopy of four examples from the initial sample set. Vast differences in porosity and morphology are evident.



(a)



(b)

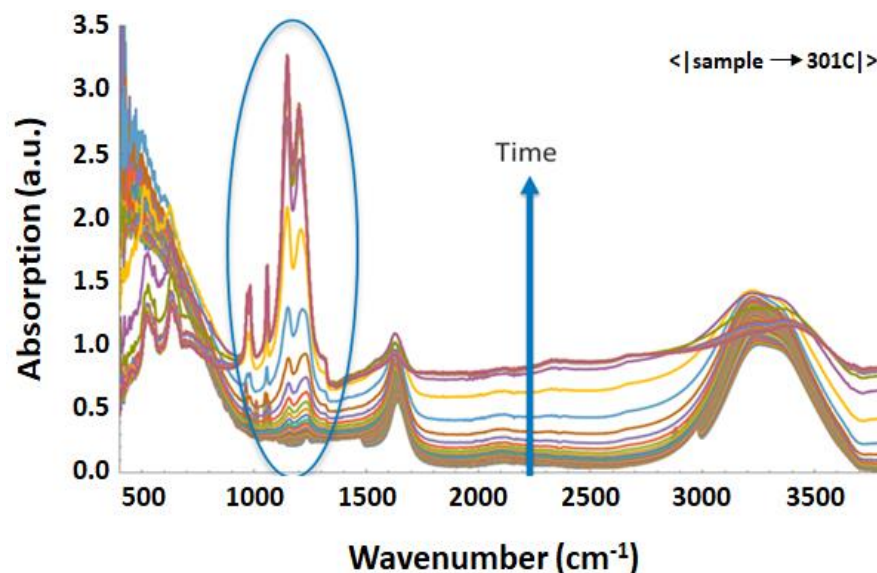


(c)

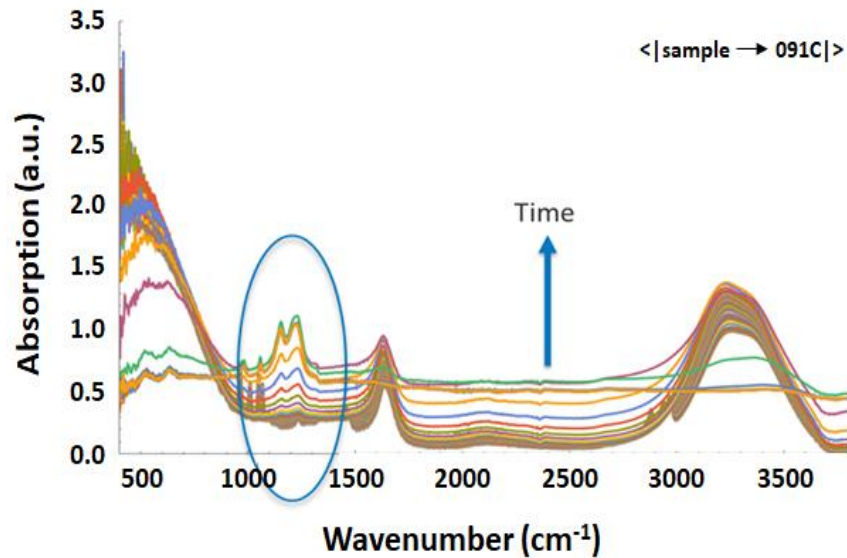
(d)

Figure 72 Optical micrographs for (a) a particle-polymer electrode, (b) an anionic membrane, (c) a cationic membrane and (d) a reverse osmosis membrane. Source: NREL

In an effort to more fundamentally explore the use of spectroscopy methods for in-line NDE, NREL, in collaboration with the Colorado School of Mines, performed studies of polymer- and polymer-particle inks and dried layers using several techniques, including attenuated total reflectance-infrared spectroscopy, ultraviolet absorption spectroscopy and ultraviolet fluorescence spectroscopy. Figure 73 (a) shows temporal attenuated total reflectance-infrared spectroscopy results of polymer-particle inks with higher polymer loadings and Figure 73 (b) for lower polymer loadings during the drying process. In this experiment, the ink is on a diamond sample tip during the measurement (not a functional substrate, e.g. a membrane or gas diffusion membrane for fuel cells). Circled in blue are the evolution of peaks characteristic of the polymer as the ink dries, of magnitude proportional to polymer loading, indicating potential to perform compositional measurements of both liquid and dried heterogeneous layers. Further studies are required to understand the sensitivity of the technique to small variations in polymer loading. This could also be an interesting diagnostic method to understand drying physics of heterogeneous inks.



(a)



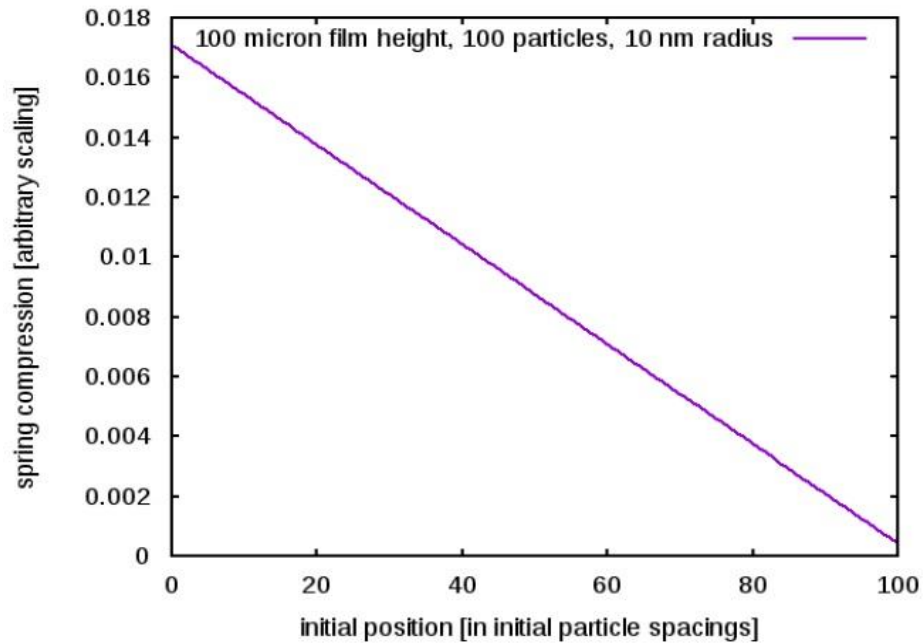
(b)

Figure 73 Attenuated total reflectance-infrared spectroscopy of polymer-particle inks during drying, with characteristic polymer peaks indicated, at (a) higher polymer content and (b) lower polymer content. Source: NREL

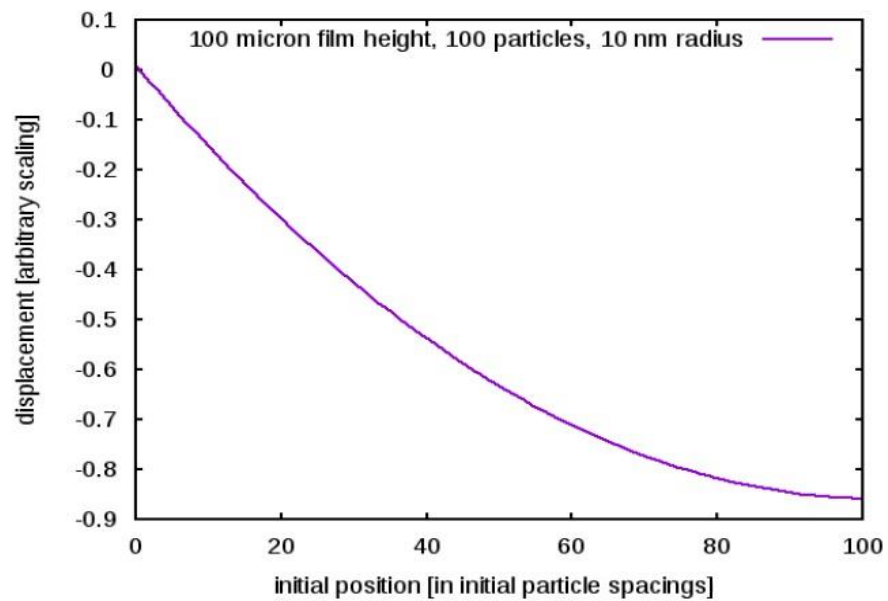
Macroscopic Mathematical Model of the Drying of a Single Layer Generic Slurry Containing Monodispersed Colloidal Particles, Binder and Solvent (LBNL Lead Laboratory)

Slurry Drying Model

Due to very late availability of funding, milestones were established late in FY 2019 (essentially for FY 2020) after meetings with and visits to the other Collaboration labs. An initial literature search and early work on a particle settling model as a first step toward a dispersion film drying model was performed. This model considered the settling of particles that are subject to buoyancy, gravity, polymer “spring” connections to other particles, and a particle network that is settling faster than surface recedes. Figure 74 (a) and Figure 74 (b) show intuitively-reasonable particle separation and particle network height under mechanical equilibrium. However, during this initial development work, it became clear that component interactions in the concentrated dispersions of interest to this Collaboration are poorly understood. Constructing a model of suspension drying that meaningfully incorporates component-level information will require the development of novel experiments for probing the behavior of these dense dispersions. LBNL has proposed to design and undertake these experiments in order to understand the physics that will be needed for further work on our film drying model.



(a)



(b)

Figure 74 (a) Relative and (b) absolute particle positions in settling particle network submodel. Source: LBNL

Subsequent efforts in FY 2019 focused on hiring postdocs and a graduate student, performing a more extensive literature search, project planning, consultation with facility scientists, and identifying and procuring the required equipment for slurry observation.

Validated Continuum-Scale Models to Accelerate Design and Scale-up of Simultaneous Die Coating Process Technology (SNL Lead Laboratory)

Model Development and Validation for Multilayer R2R Applications

Work on the model development began in late February and early March 2019 with discussions of multilayer slot- and slide-die specifications with ORNL and NREL researchers. Sandia and UNM completed the deposition model of single-layer slide coating flow using Goma 6.0 solver and began work on the multilayer slide-die model, given the specifications and range of conditions articulated by NREL. The slot-die model was planned based on the feedback from ORNL. The approach was to solve partial differential equations of capillary hydrodynamics (Navier-Stokes, coupled mesh motion and relevant constitutive equations) in a successful 2D coating process. The starting geometry for the slot-die model was for the ORNL Dynacoat Lab Coater. An example of the solid model in a finite element mesh is shown in Figure 75. In support of the SNL slide die modeling effort, NREL provided initial information on expected ink properties, slide die geometry, and process conditions for our initial target multi-layer coatings.

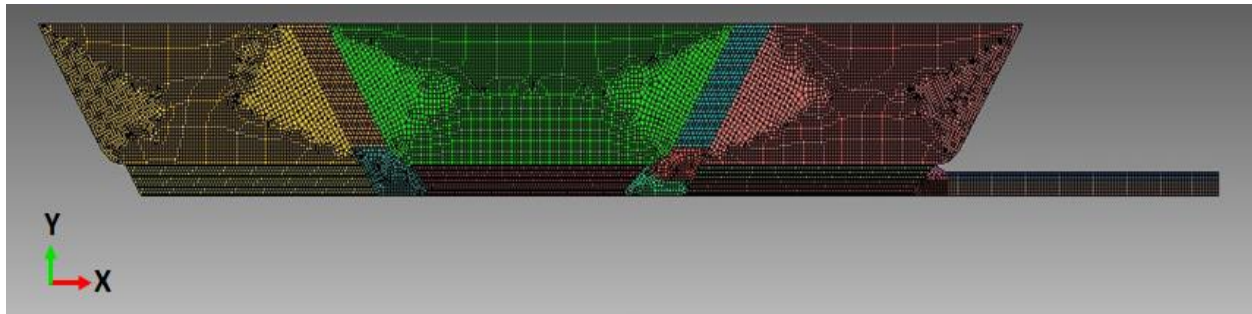


Figure 75 Solid model in a finite element mesh. Source: SNL

Procedures were needed for modeling of the physical properties and operating conditions. Experience in capillary hydrodynamic modeling is essential. The system is highly nonlinear system with a capillary force at free surface for a shear thinning liquid and a pseudo solid mesh. To obtain a direct approach to steady-state conditions with a Newton method required a “good” initial guess to stay in the ball of convergence. A free surface based solution was obtained in a strategic continuation from fixed mesh solution. A similar procedure to obtain solutions at different operating conditions and physical properties required remeshing.

SNL and UNM completed the deposition models of single- and two-layer slide coating flow using NREL’s multilayer slide-die design as a simple Newtonian base case, and the single and two-layer slot-die coating flow using ORNL’s two-layer die design as a base case. These models have a working user interface to improve usability by the partners and industry. An example of a single-layer mesh and pattern simulating pressure and flow is presented in Figure 76. NREL provided SNL with rheological data for a representative multilayer slide coating stack, and the data have been fit with standard constitutive equations and implemented in the models. Simulations with Newtonian and shear-thinning fluid layers were developed, and SNL improved the multilayer slot-die model with the specifications and range of conditions articulated by ORNL.

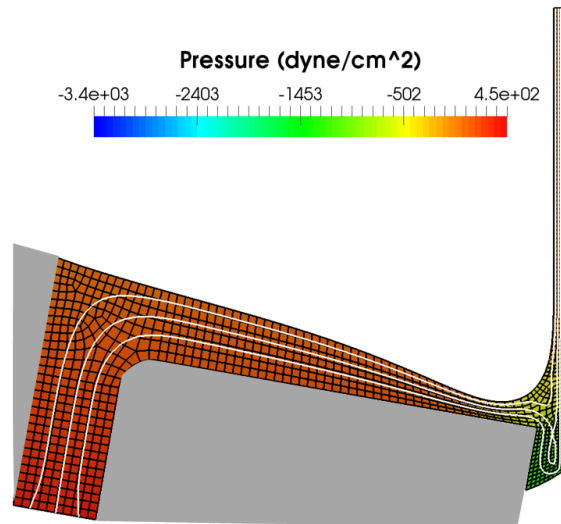


Figure 76 Single layer mesh and pattern of pressure (color map) and flow (streamlines). Source: SNL

Modeled operating conditions were a film thickness (both layers) of 0.006 cm, a viscosity of 0.45 Pa.s, a surface tension of 30 dyn/cm, a dynamic contact angle of 120° and a pressure (vacuum) of 6000 dyn/cm². Computational assumptions were pinned static contact lines, a slip-length of 0.001 cm, and a slip coefficient of 10⁻⁴. The two-layer pattern of pressure and flow is presented in Figure 77. The slide-die models were advanced to include rheologies relevant to the fuel cell applications, which are shear-thinning. Newtonian rheology is being used in the slot-die model.



Figure 77 Two-layer pattern of pressure (color map) and flow (streamlines) for ORNL slot die geometry. Source: SNL

A user-interface was advanced to include the ability to manage solutions and parameter changes. The user interface is split into two main windows: (1) Parameters and (2) Axis Editor. The parameter list includes all the parameters that are accessible to user modification. The Axis Editor executes Goma 6.0 to obtain solutions the specified parameter ranges (and displays the solution). The user interface enables global “undo/redo” of any modifications to parameter values or axis assignments in case of a convergence failure.

In the single-layer model, operability limits are set mainly by bead menisci shapes and positions. Bead breakup can be delayed with altering the rheology and slide-web gap. In the two-layer model, the interlayer and free surface shape at varying flowrates and web speed can be predicted. The focus will be to minimize flow recirculation near interlayer and thereby preventing interlayer mixing.

Coating trial studies with multilayer slot- and slide-die coating began at the end of FY 2019 with data and parameters being supplied by ORNL and NREL. SNL adapted ORNL slot-die coating parameters for coating trials of PEMFC GDE films where the coating was almost uniform and very thin (7-10 μm dry). Additional data from coating trials in FY 2020 will be used to improve models further.

Collaboration/Coordination/Outreach/CRADA Projects

Core Program

The Collaboration laboratories collaborated and with each other on a weekly basis, either through visits or via telecommunications. Team meetings involving the laboratory leads and principal investigators occurred bi-weekly and included the DOE Technical Managers at one meeting every month. Outreach continued through the principal investigators and researchers presenting at conferences, symposia, peer reviews and during direct contact with industry and the commercial sector. Specific research was reported in technical journals and through patent applications.

CRADA Projects

USC Title 15, Chapter 63, Section 3710c, paragraph 7(A) allows for non-disclosure of trade secrets or commercial or financial information that is privileged or confidential, which is obtained in the conduct of research or as a result of activities from a non-Federal party participating in a CRADA. The government agency may provide appropriate protections against the dissemination of such information for a period of up to 5 years after development of information. As such, some technical information on the CRADA projects will not be included in this report. The following information for each CRADA project was approved or provided by the CRADA partner.

Fisker, Inc

Fisker, Inc. partnered with LBNL and ORNL to demonstrate all-solid-state batteries based on LLZO separators and cathode scaffolds and scale the freeze casting process to the pilot level at ORNL. ORNL and LBNL worked with Fisker to purchase 1.5 kg of LLZO powder for freeze casting and sintering experiments. The 1.5 kg will be split between the two labs with 1.0 kg going to ORNL for scale-up processing and 0.5 kg going to LBNL for formulation and deposition development.

Through processing variable optimization, LBNL produced freeze tape cast green tapes at $< 200 \mu\text{m}$ which is a layer thicknesses suitable for practical applications. In order to mitigate the green tape cracking issue during freeze drying, 10 vol.% LLZO slurries were mainly cast for easier handling. Other processing parameters were further optimized. The slurry stability was improved by introducing a PAA dispersant which allowed the slurry to stay well dispersed throughout the entire casting period. By adjusting the casting speed and the freezing bed temperature, a range of pore sizes could be obtained as shown in the SEM fracture surfaces of Figure 78.

Vertical pore alignment is obvious. Smaller pore sizes resulted in higher specific surface area, a key factor in mitigating the cathode/electrolyte interfacial impedance. However, optimal usable pore size is dependent on the infiltration process of the cathode components which requires further exploration.

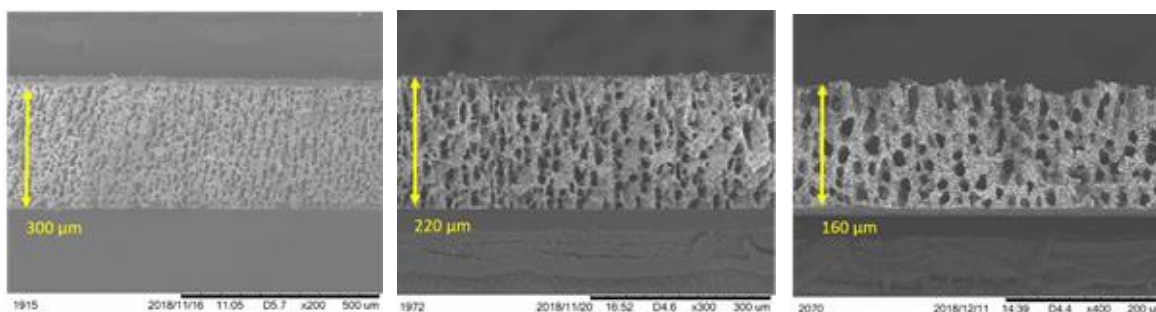


Figure 78 SEM fracture surface images of freeze tape cast (10 vol.% LLZO slurry) produced at thicknesses of 300 μm , 220 μm and 160 μm and at various casting speeds. Source: LBNL

Freeze tape cast and tape cast LLZO green tapes were stacked and sintered to produce dense/porous bilayers of LLZO as shown in Figure 79 (a). Cathode components were dispersed in an organic solvent and drop cast onto the porous layer as shown in Figures 79 (b) and Figure 79 (c). Red arrows in Figure 79 (c) indicate the nickel-manganese-cobalt (NMC) 622 ($\text{LiNi}_{0.6}\text{Mn}_{0.2}\text{Co}_{0.2}\text{O}_2$) was infiltrated to the porous layer in a slurry form of the cathode components. The cathode components occupy only a small fraction of the total porosity and mostly exist as deposits on the interior pore wall.

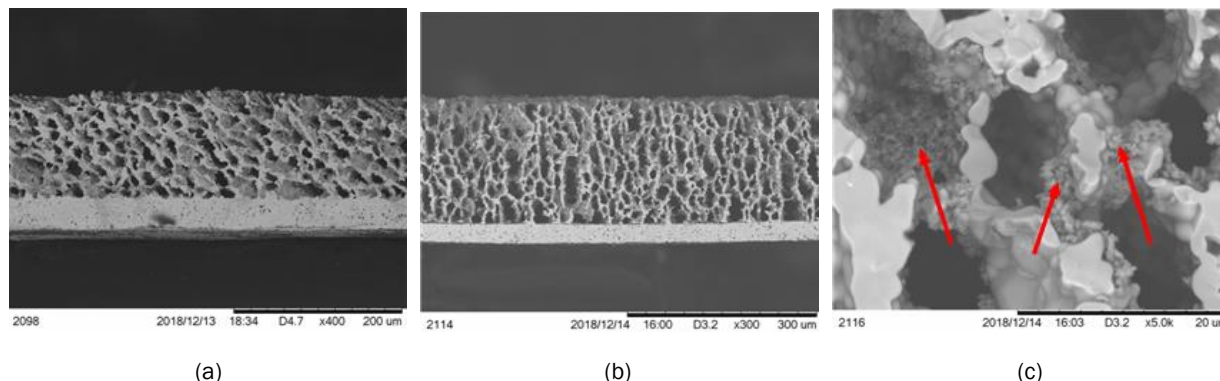
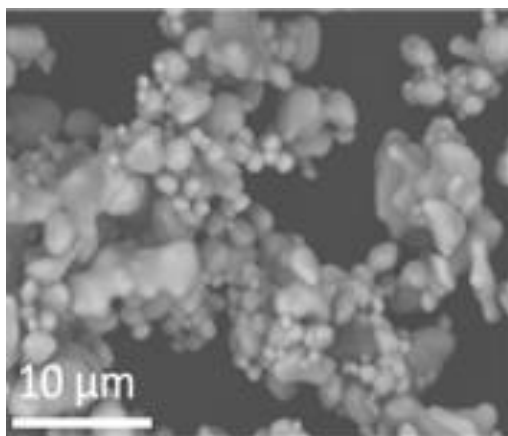


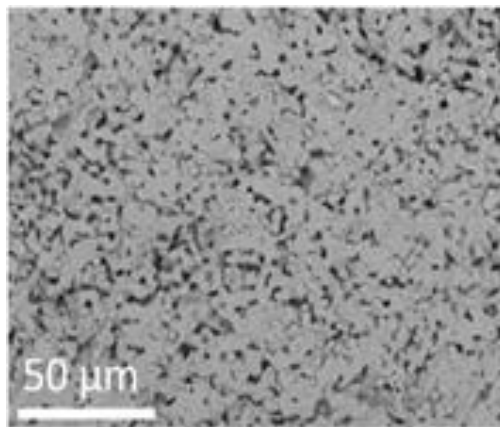
Figure 79 (a) Sintered dense/porous LLZO bilayer and (b) and (c) the cathode component infiltrated bilayer. Source: LBNL

ORNL confirmed the status of the sputter coater that will be used for depositing LiPON onto the dense LLZO layer. LBNL and ORNL collaborated on the deposition of LiPON onto the dense LLZO layer. It was decided to first deposit LiPON by itself to characterize its quality. LLZO powder was purchased from a different vendor due to difficulties in receiving commercial LLZO power from Fisker and costs from the vendor that was previously used. This required adjustments to the slurry formulation and freeze tape casting parameters. With stable production of the bilayers, research was focused on the cathode infiltration process. Little work has been done previously on the Li deposition onto LLZO, other than a gold interfacial coating. At ORNL, the clean room deposition chamber, which will be used to make Li and LiPON films, is fully contained within a glovebox having an argon atmosphere. Nitrogen will also be used for LiPON deposition. Both radio-frequency sputtering and thermal evaporation of Li can be performed in this setup. The minimum pressures that the chamber can hold are about 1 μ Torr.

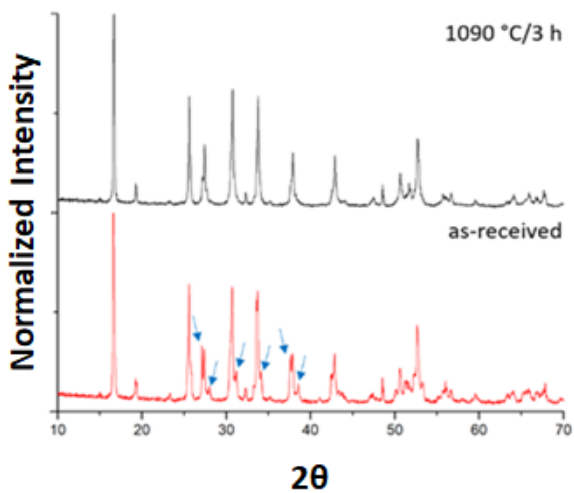
Powder characterization and freeze tape casting experiments were conducted using commercial Al³⁺ doped LLZO. As-received powders were several microns in size with majority of them showing necking from calcination as can be seen in Figure 80 (a) and Figure 80 (b). The XRD analysis in Figure 80 (c) showed a mixture of cubic and tetragonal LLZO suggesting the powder is Li rich. It also had a thick (>160 nm) Li₂CO₃ surface coating layer, as confirmed by XPS, likely due to reaction with atmospheric air. XRD of powder compacts (pellets) heated to 1090 °C/3 h showed smaller t-LLZO peaks, suggesting that c-LLZO can be obtained by blowing off excess lithium while sintering, also shown in Figure 80 (c). Zeta potentials of the powder were measured in the pH range of 3-11 using two dispersants polyethylenimine (PEI) and PAA and the plot of the data is presented in Figure 80 (d). The results suggested that PAA is a great dispersant for slurry formulation as the LLZO slurry is highly basic (pH 14+) due to the protonation of LLZO in water. However, the formulated slurry showed rapid powder flocculation and it was empirically determined that the xanthan gum, the thickener, was affecting surface chemistry of the dispersed LLZO powder.



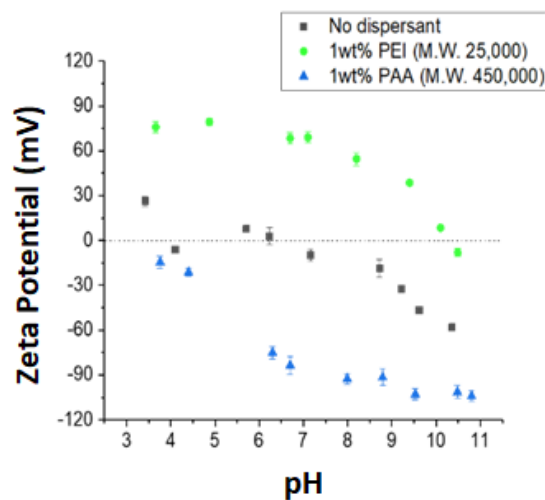
(a)



(b)



(c)



(d)

Figure 80 (a) and (b) SEM images and (c) XRD analyses of as-received LLZO power and LLZO powder compacted (pellet) and heated to 1090 °C for 3 hours where blue arrows indicate t-LLZO peaks. (d) Zeta potentials of as-received LLZO with selected dispersants at varying pH. Source: LBNL

In order to achieve viscosities suitable for freeze tape casting, the LLZO fraction was increased from 10 to 14 vol.% in the slurry. Well aligned LLZO struts are observed in the fracture surface SEM images of the freeze tape cast green tape as seen in Figure 81 (a) and Figure 81 (b). The slurry formulation was transferred to ORNL and initial results showed similar pore structures shown in Figure 81 (c) and Figure 81 (d).

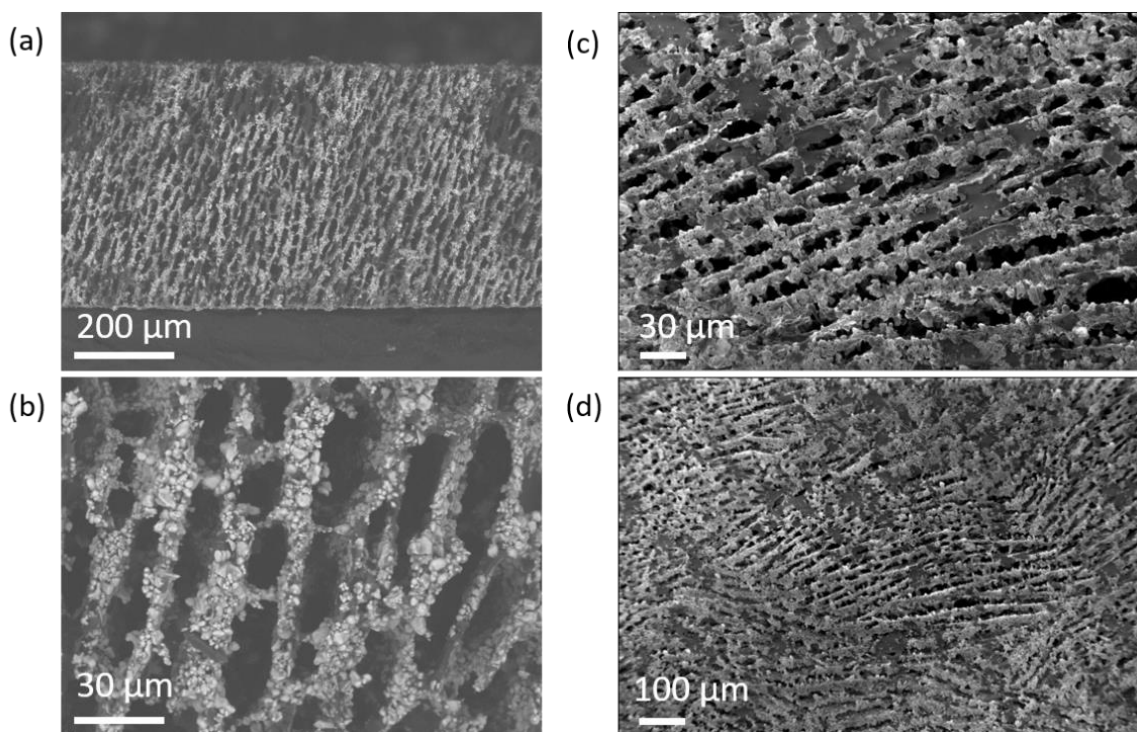


Figure 81 (a) and (b) Fracture surface SEM images of freeze tape cast LLZO green tapes produced at LBNL, and (c) and (d) surface SEM images of green tapes produced at ORNL. Sources: LBNL and ORNL

Preliminary LLZO (from NEI) slurry formulations were received from LBNL and evaluated at ORNL. Slurries were initially made (both at LBNL and ORNL) on a small scale (with 4-6 g of LLZO powder) to produce freeze tape cast porous layers which are only two to three inches long. Slurry stability was assessed visually, and the final pore structure obtained was characterized via SEM imaging.

As can be seen in Figure 82 (a) and Figure 82 (b), the water-based slurry of LLZO had stability issues. The solids tended to separate from the solvent (water) to form a two-phase mixture with time. This is an issue for scaling-up of the freeze tape casting process, as the slurry needs to be stable for several hours, given the slow speed freeze tape casting. A non-homogenous slurry would lead to segregation of LLZO and binder in the final porous layer.

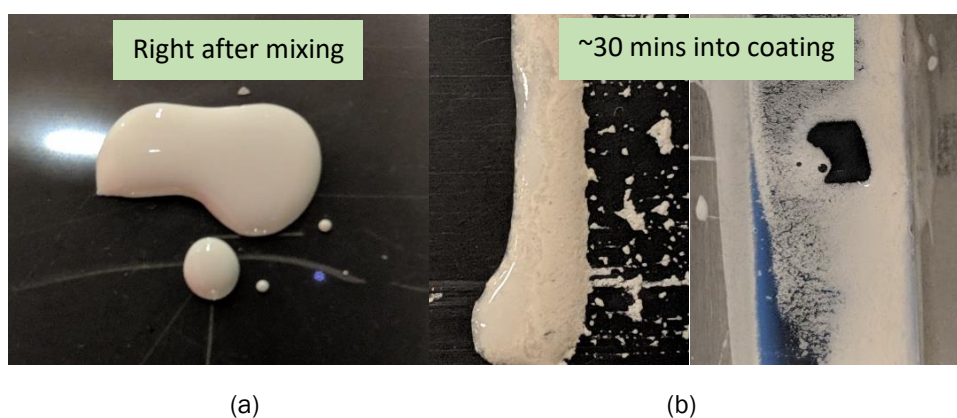


Figure 82 Photographs of a water-based LLZO slurry (a) after mixing and (b) after ~30 mins. Source: ORNL

One important characteristic that determines the slurry stability is the surface charge of particles in a dispersion as it provides electrostatic hinderance towards flocculation. To identify a suitable dispersant for the LLZO particles, ORNL measured surface charge of LLZO particles (from NEI) dispersed in water with and without the presence of various dispersants via zeta potential measurements as a function of pH as shown in Figure 83. A cationic dispersant (polyethyleneimine (PEI)), and an anionic dispersant (PAA) were chosen for the measurements. PAA was also the dispersant in the LBNL slurry recipe. Due to leaching of Li^+ -ions from LLZO when in contact with water, the LLZO slurry is very basic ($\text{pH} > 12$). Therefore, a high surface charge at this pH value of 12 would be favorable. As can be seen from the results in Figure 83, PAA would be better than PEI, as the surface charge of LLZO in its presence is < -90 mV. PEI on the other hand would be a better dispersant at a lower pH. These results were communicated to LBNL to help make guided decisions for improving the slurry stability.

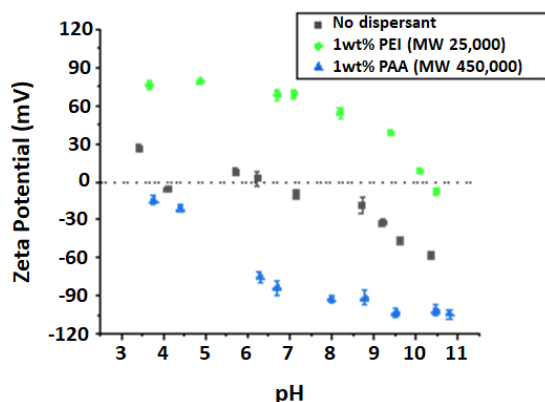


Figure 83 Zeta potential of LLZO in the presence/absence of dispersants. Source: ORNL

Various parameters such as the amount and type of dispersant, thickener amount/type, and binder as well as the mixing method were tuned to improve the long-term stability of the slurry.

Freeze tape casting formulations were further developed using the NEI LLZO powder to achieve improved stability, ice structure, flexibility, and sample uniformity. Acrylic latex emulsion binder with a low T_g (-45°C) was introduced to impart flexibility while frozen to prevent sample cracking during freeze drying. It was possible to freeze tape cast a 4'' x 4'' porous LLZO scaffold through slurry viscosity and additive content optimization which showed good sample uniformity. LBNL was able to consistently freeze tape cast LLZO powders from two different vendors. Figure 84 (a) shows the SEM fracture surface image of freeze tape cast NEI LLZO green tape and Figure 84 (b) is a higher magnification clearly showing the vertical pore structures.

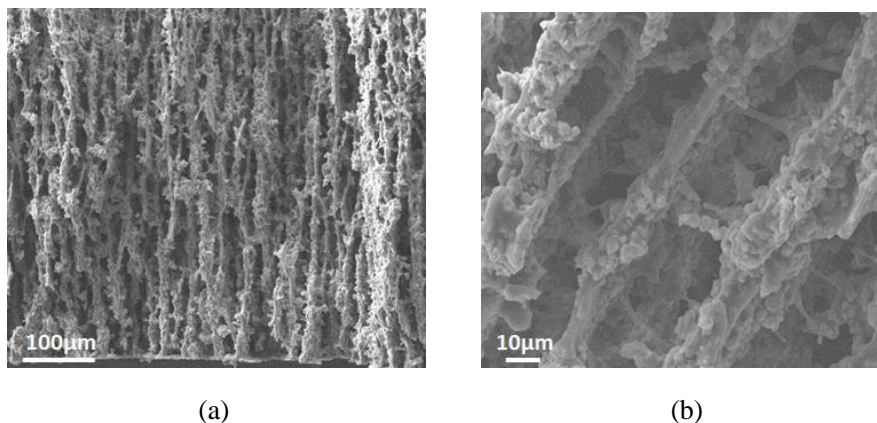


Figure 84 (a) SEM fracture surface image of freeze tape cast NEI LLZO green tape and (b) at 10x magnification. Source: LBNL

The freeze tape cast green tape from the LBNL process was combined with tape cast green tape provided by Fisker to sinter a porous/dense bilayer LLZO architecture. On sintering to 1090°C for 3 hours, the two layers were well bonded as can be seen in Figure 85 (a) and Figure 85 (b). The tape cast green tape sintered to high densities with no open pores.

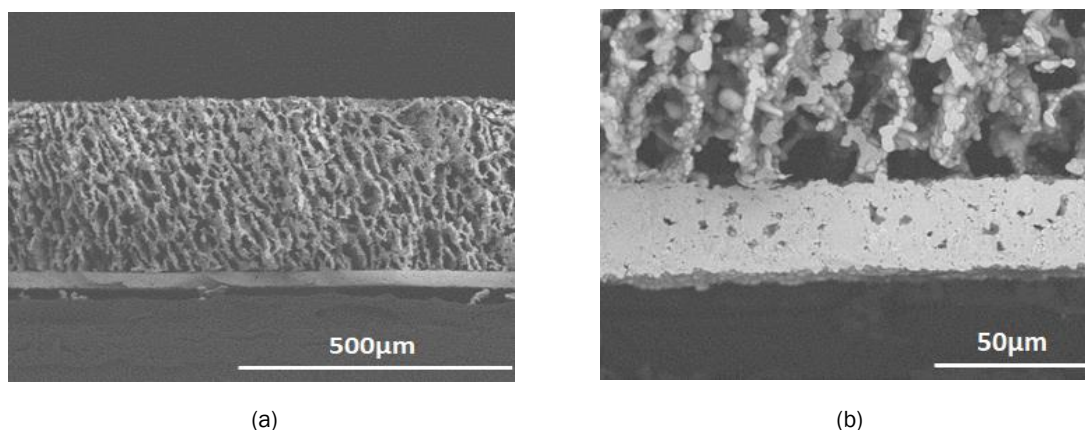


Figure 85 SEM fracture surface images of (a) a sintered porous/dense LLZO bilayer and (b) at 10x magnification. Source: LBNL

LBNL scientists visited ORNL to assist with freeze tape casting because there were inconsistencies in the ice structures between the two labs. Two postdocs worked side by side along the entire slurry formulation to freeze tape casting process and was able to reproduce the freeze tape casting results of LBNL at ORNL. Several factors including additive content, mixing method, freeze tape casting parameters were adjusted to fit the ORNL lab condition (e.g. humidity, room temperature, etc.)

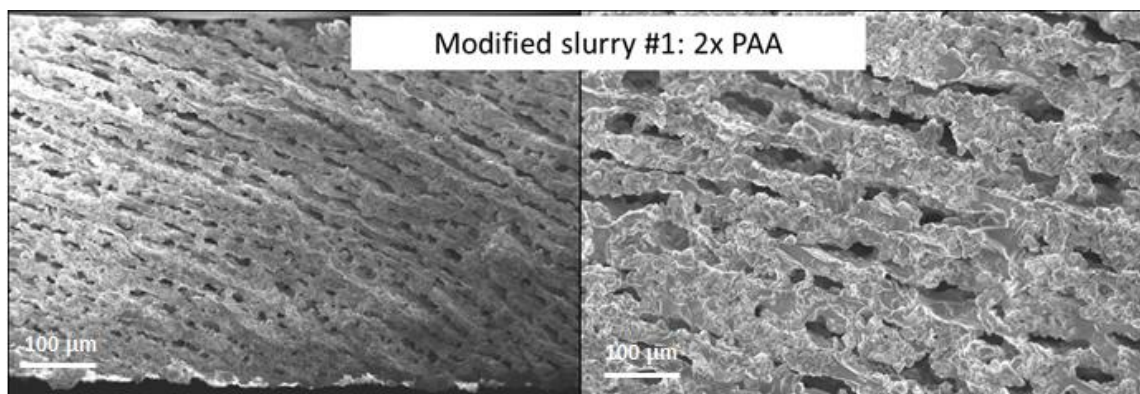
Preliminary NEI LLZO slurry formulations were received from LBNL and ORNL attempted to use them on their freeze tape caster. Table V shows the detailed slurry formulation. Initially, the slurries were made at LBNL and ORNL on a small scale with 4-6 g of LLZO powder to produce freeze tape cast porous layers which are only two to three inches long. Slurry stability was assessed visually, and the final pore structure obtained was characterized via SEM imaging.

Table V NEI LLZO Slurry Recipe for Freeze Tape Casting Transferred from LBNL to ORNL

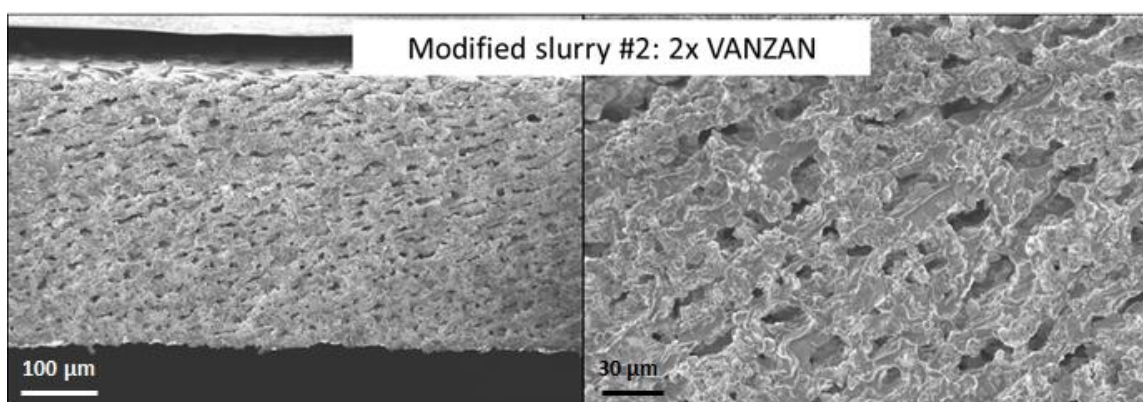
Component	Solids Weight (g)	Solution Weight (g)
NEI LLZO	6	N.A.
Li ₂ CO ₃ (20% excess)	0.33	N.A.
PAA MW: 450,000	0.032	N.A.
HA-12	0.72	1.6
VANZAN (0.2wt%)	0.00545	5.45

Flocculation in a dispersion could also be retarded sterically by increasing the viscosity. High molecular weight PAA (MW 450,000) can act both as a dispersant (discussed above) and a thickener. Xanthan gum (VANZAN) is the primary thickener in the formulation shown in Table V. In order to improve slurry stability, ORNL modified the recipe in Table V in two ways and observed the slurry stability with time visually. In one case, the amount of PAA as doubled, while in the other case, the amount of VANZAN was doubled while keeping the rest of the formulation same. In both cases, slurry stability was significantly improved, and no

flocculation was observed after 30 mins. Figure 86 (a) and Figure 86 (b) show SEM images of the cross-sections of the freeze tape cast porous tapes obtained with the above two slurry modifications.



(a)



(b)

Figure 86 SEM images of the cross sections of the freeze tape cast porous tapes obtained with slurries that have either (a) double the amount of PAA or (b) double the amount of VANZAN compared to the original recipe shown in Table V. Source: ORNL

Even though the slurry stability was improved for these cases, the resulting porosity in the freeze-dried tapes was not satisfactory. Pores alignment was not vertical, pore-size was smaller than what LBNL demonstrated for their recipe, and pore walls were thicker. An ideal case scenario demands vertical pores with almost zero tortuosity and high pore volume with large pores ($>20\ \mu\text{m}$) for easier cathode infiltration.

LBNL personnel visited ORNL to observe each step during the freeze tape casting and to point out things that ORNL might have been doing differently that resulted in not being able to reproduce the porous tape structures at ORNL. The LLZO slurry recipe shown in Table VI was freeze tape cast. This formulation was more stable towards flocculation and resulted in more flexible freeze-dried green tapes compared to the previous recipe in Table V. Specifically, this slurry recipe is different in the following aspects: (1) a higher Li_2CO_3 content (30% excess vs. 20% excess earlier), (2) use of a different emulsion binder (Rovene 97982) in combination with the previously used HA-12 emulsion binder (60:40 ratio), and (3) double the amount of PAA and VANZAN. Rovene 97982 is a soft acrylic emulsion known for its flexibility. Improvement in the slurry stability by doubling the amounts of PAA and VANZAN was observed at ORNL as well. Indeed, during freeze tape casting no visible flocculation was observed for 30-60 mins.

Table VI Modified NEI LLZO Slurry Recipe for Freeze Tape Casting

Component	Solids Weight (g)	Solution Weight (g)
NEI LLZO	6	N.A.
Li ₂ CO ₃ (30% excess)	0.495	N.A.
PAA MW: 450,000	0.065	N.A.
HA-12	0.36	0.96
Rovene 97982	0.36	0.64
VANZAN (0.2wt%)	0.011	5.5

Overall, several differences were noted in the way of mixing the slurry components as well as seemingly insignificant things during the casting step, which likely resulted in the inconsistency in the final porous tape structure obtained at LBNL versus at ORNL for the same slurry recipe. Two freeze tape casting runs were performed for the slurry in Table VI but at different freezing temperatures and line speed.

The first freeze tape casting run was made at 20% of the line speed and a freezing bed temperature of minus 13°C. Figure 87 schematically shows the areas that were characterized via SEM. A thin strip parallel to the freeze tape casting direction was cut from the middle of the dried tape. The tape was fractured by bending at three locations, more and more further from the front edge of the tape. This was done to assess the areal uniformity of the porosity. It is typically expected that the area further from the front edge would have much less developed porosity as it would be freeze cast later compared to the area closer to the front due to slurry stability/drying issues.

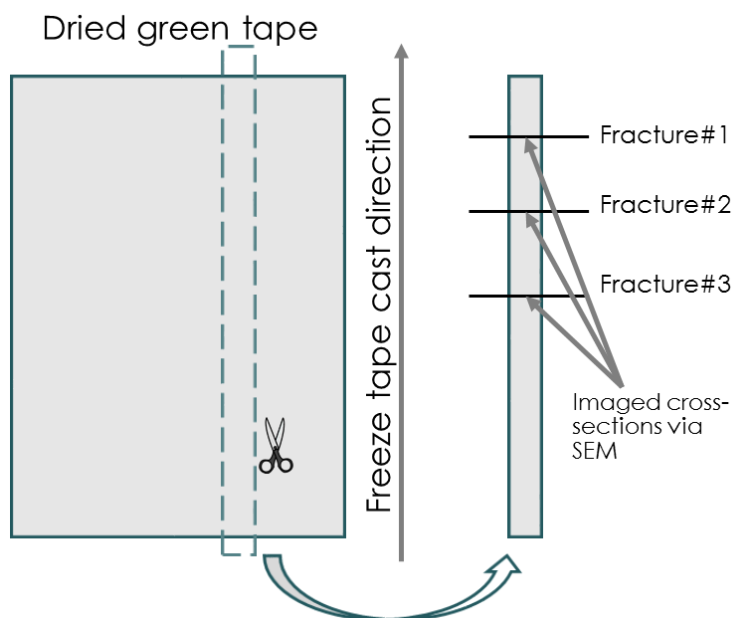


Figure 87 Schematic showing the areas of the tape that were characterized via SEM. Source: ORNL

Figure 88 shows the SEM of the three cross-section areas at 50× and 100× magnifications. Porosity can be seen throughout the width of the tape. However, it was uncertain why the pores are still at an angle (similar to Figure 86). NREL suggested that it may have to do with angle between the direction of the fracture and direction of the ice lamella growth in that region. To see perfectly vertical columnar walls, the fracture should be perpendicular to the lamellar growth. Ideally, the ice lamellar growth should occur in the freeze tape casting direction; however, for variety of reasons, ice growth occurs in random directions throughout the tape.

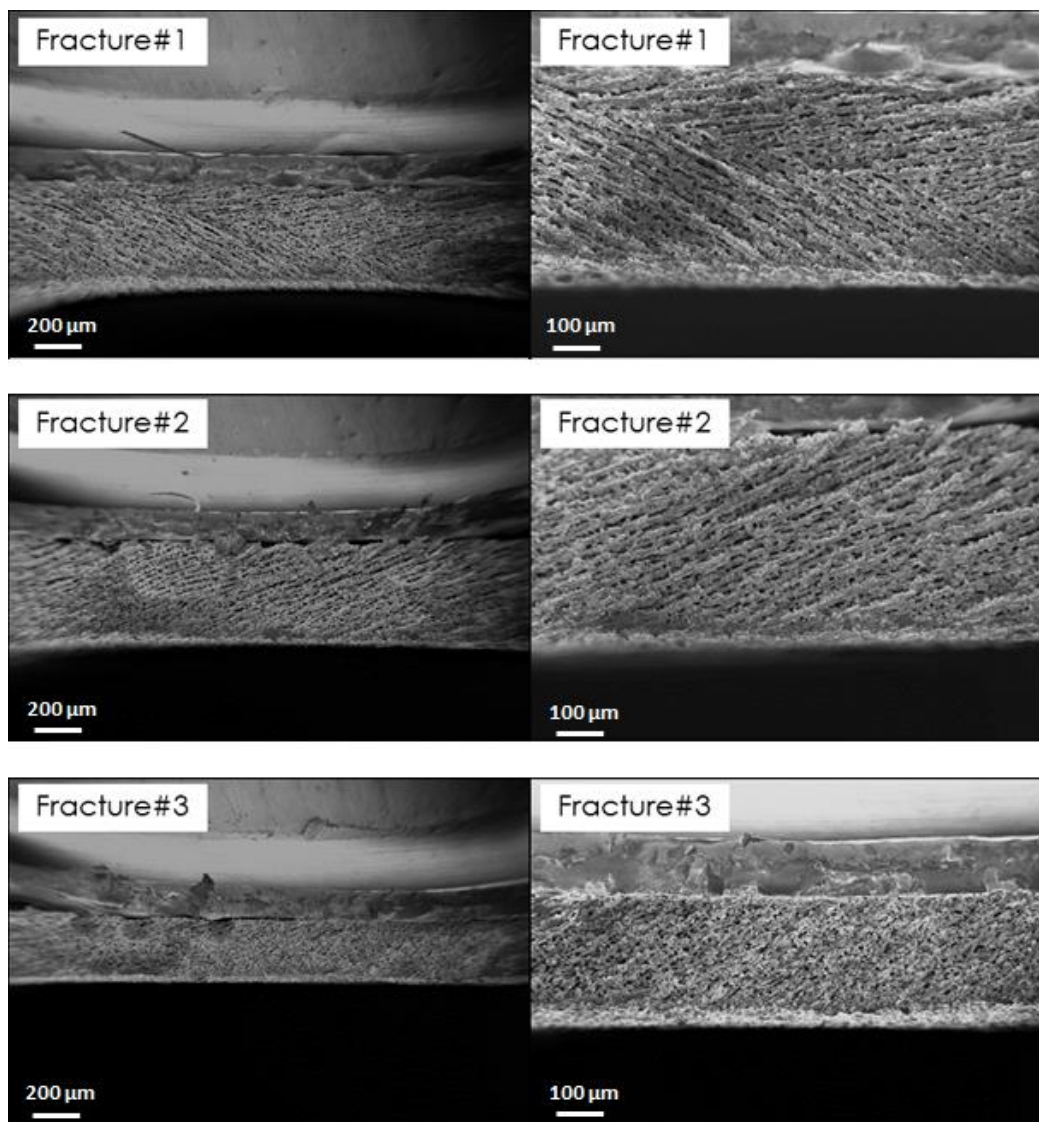


Figure 88 SEM of the cross-sections from three different areas of the LLZO freeze tape cast green tape from the first run.
Source: ORNL

The second freeze tape casting run was made at 15% of the line speed and a freezing bed temperature of minus 11°C. The same slurry recipe as in Table VI was used. Freeze tape casting conditions were changed to have higher freezing bed temperature (-11°C vs. -13°C) and slower line speed (15% vs. 20%). A higher temperature was used to get larger ice crystals and, therefore, larger pores. For SEM imaging, the sample was fractured differently this time. Fracture was done in the direction perpendicular to the ice lamella growth to observe the columnar structure. This is shown schematically in Figure 89.

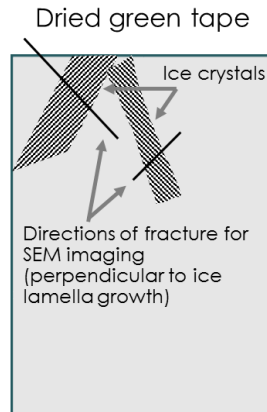


Figure 89 Schematic highlighting the difference in the way the freeze tape cast was fractured for SEM imaging the cross-sections for the second run. Source: ORNL

Three such perpendicular fractures were made, and the SEM cross-sections are shown in Figure 90. As can be seen, the vertical columnar structure can be observed in some areas; however, the areal uniformity of such porosity still needs to be greatly improved. For example, fracture #3 does not have the similar columnar porosity.

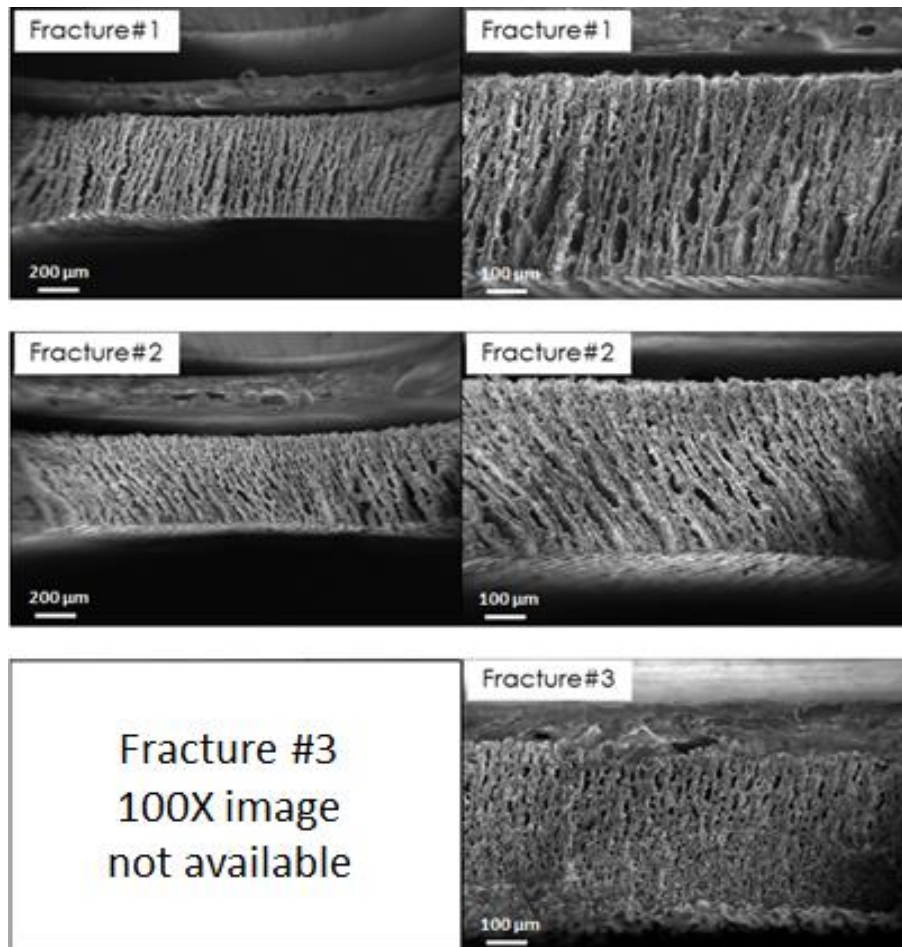


Figure 90 SEM of the cross-sections from three different areas of the LLZO freeze tape cast green tape obtained from the second run. Source: ORNL

Navitas Systems, LLC

Navitas Systems, Inc. partnered with ORNL and NREL to demonstrate R2R production of advanced separator for lithium ion batteries. A R2R method was developed to fabricate the separator, which replaces the conventional discrete operations and enables superior safety, high throughput and low manufacturing cost.

Selection of Baseline Commercially-Available Separators

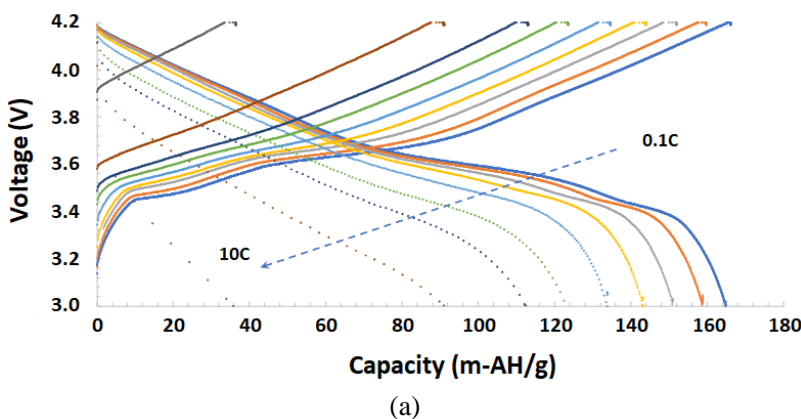
Initially, ORNL evaluated rate performance of two separators along with standard full coin cells and estimated the cost savings that could be achieved from the new technology. Most of the benefits will be seen in the heat pressing portion of the process, which has a ~90 sec cycle time. Substantial decreases in cycle time (>20%) will decrease the number of heat presses that Navitas will ultimately have to purchase and operate. Cycle time improvements could result in savings of up to \$1M in capital equipment investments and corresponding savings in facility floor space and utilities use as well as direct labor burden. At 1.5M cells/year, savings will be on the order of ~0.10/cell (0.5% of cell cost) per reduced heat press. There would be up to a ~2% cost savings on the cell product for Navitas.

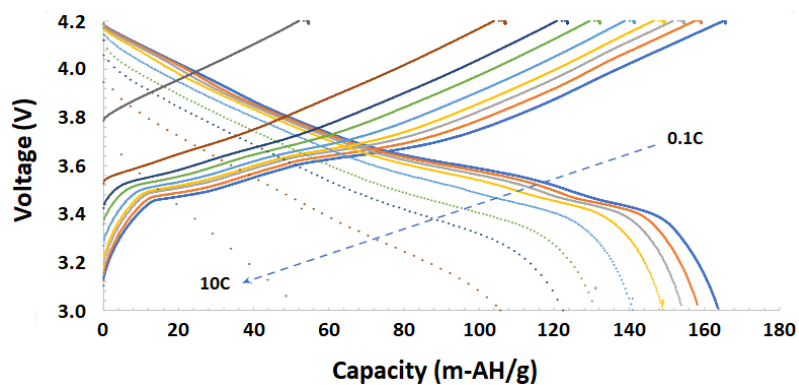
NREL and ORNL collaborated with Navitas on the designs for patterning new gravure rollers, the separators, and materials for the patterned coating. Full coin cells consisting of NMC622 and graphite from Superior Graphite (SLC 1520T) were assembled. The electrodes as fabricated with the composition in Table VII were coated by a slot-die coater. The electrodes were assembled as coated after a secondary drying at 110 °C under a vacuum oven at 30-inch Hg vacuum overnight. Triplet cells were assembled with each separator. The cells went through constant current charge to 4.2V and constant voltage charge until current dropped C/20 where 1C = 175 mA/g of NMC622. The charge rate was the same as the discharge rate when discharge rate was below C/3 and was kept at C/3 at the higher discharge rate. A series of discharge rates from 0.1C to 10C and six cycles for each rate were evaluated.

Table VII Coin Cell Electrode Areal Loading and Composition

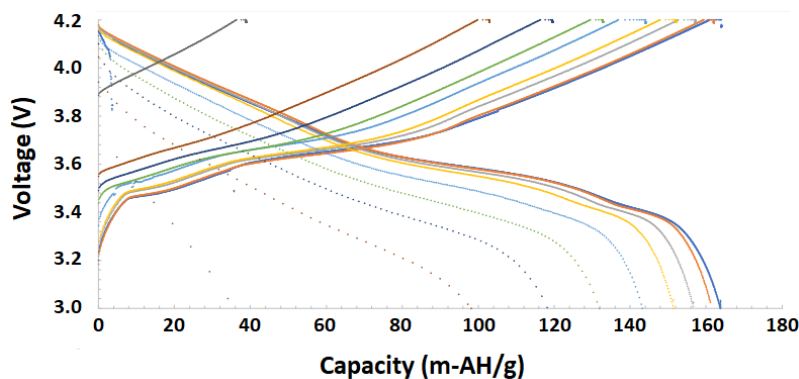
Areal Loading (mg/cm ²)	Electrode Composition
11.9	NMC622/Denka CB/5130 PVDF in 90/5/5 wt%
6.4	SLC1520T/C65 CB/9300 PVDF in 92/2/6 wt%

Voltage profiles under various C-rates for the three separators are shown in Figure 91 (a) for Celgard, Figure 91 (b) for Laminable Separator B, and Figure 91 (c) for Laminable Separator C where the solid lines and dash lines represent charge and discharge capacity, respectively.





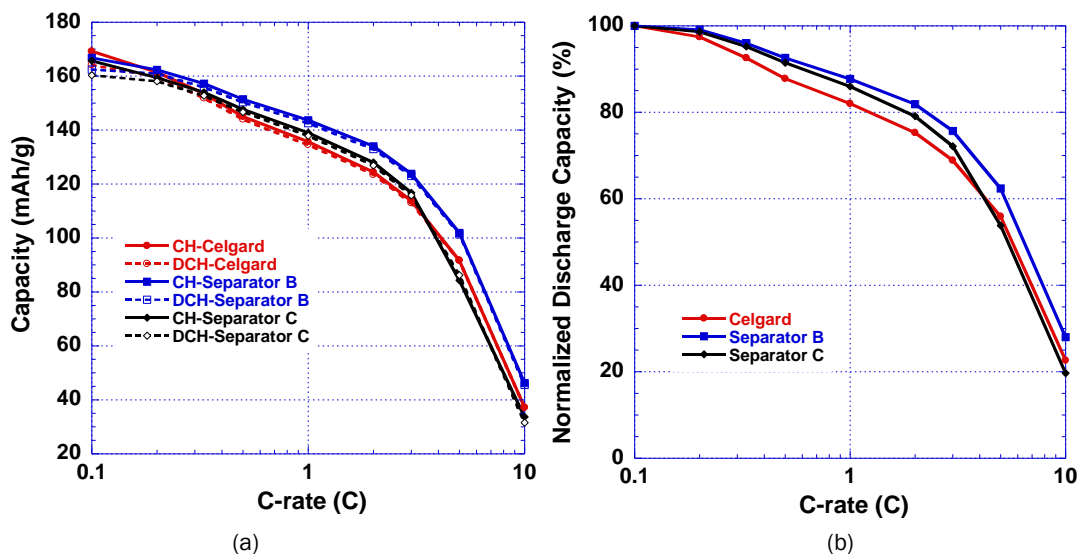
(b)



(c)

Figure 91 Voltage profiles for various separators: (a) Celgard, (b) Separator B and (c) Separator C. Source: ORNL

Rate performance is compared for capacity in Figure 92 (a) and C-rate in Figure 92 (b) where cells with three separators show great performance with >160 mAh/g at C/10. Among the three separators, Separator B shows slightly better rate performance than the other two. For example, the normalized discharge capacity was 82% at 2C compared to 75% and 79% for Celgard 2325 and Separator C, respectively.



(a)

(b)

Figure 92 Rate performance comparison for three separators: (a) capacity and (b) normalized discharge capacity vs C-rate. Source: ORNL

The self-discharge phenomenon was also investigated by recording the OCV during 24 hours of rest after fully charging the cells to 4.2C at C/3. As shown in Figure 93, the OCV dropped gradually as time went on which is normal. The initial voltage drop was due to the polarization in the cells and the subsequent voltage drop would be attributed to leakage current between cathode and anode and any side reactions. Since the cells are identical except for the separator, we could ascribe the difference to the separator. The cell with Separator B separator demonstrated less voltage drop, which indicates lower self-discharge rate.

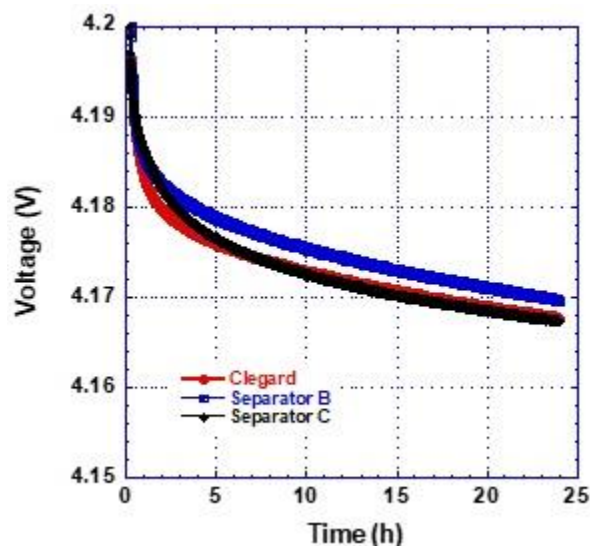


Figure 93 OCV of cells with various separators during a 24-hour rest. Source: ORNL

ORNL and NREL coordinated the design of the patch coating of separators. NREL designed and 3D-printed prototype masks for the small-scale ultrasonic spraying of the patterned coatings of interest. The pattern of interest is cross-hatched lines (for one coating) and the interior squares of the cross-hatch (for the second coating). The mask for the square pattern is simple. However, the mask for the lines involves “floating” squares that must be supported by raised elements. Using the second mask, we sprayed substrates with Pt-containing inks (i.e. fuel cell electrode inks) to understand the impact of various design aspects of the mask geometry on the uniformity of the patterning. Figure 94 provides a top view of one of the prototype masks showing the mechanical design of lines in the mask. Figure 95 is an image of the substrate sprayed with this mask showing the cross-hatched line pattern. Figure 96 is X-ray fluorescence spectroscopy (XRF) data across a square element of the mask (no coating) and two adjacent lines (with coating), using the Pt signal to indicate the uniformity and shape of each coated line. These initial experiments provided feedback on the different mask design elements and was informative for full-size mask design and printing.

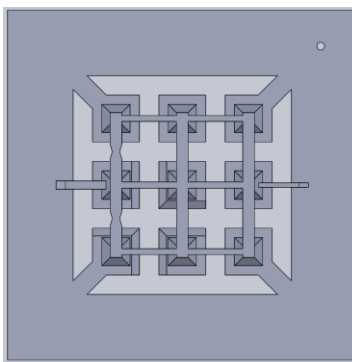


Figure 94 Top view of the mechanical design for lines in the 3D-printed prototype mask. Source: ORNL

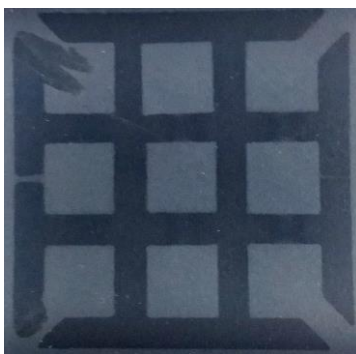


Figure 95 Substrate sprayed with the mask showing a cross-hatched line pattern . Source: ORNL

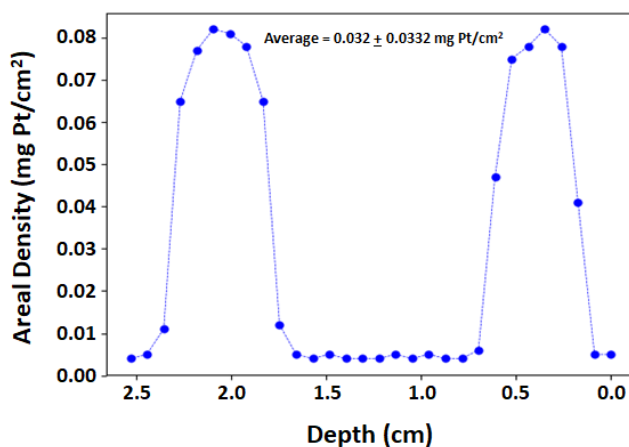


Figure 96 XRF data showing uniformity and shape of the sprayed lines. Source: ORNL

Development of Formulations for a Ceramic Coating on the Separator

Two ceramics, aluminum oxide (Al_2O_3) and titanium oxide (TiO_2), were selected for the coating materials. The initial plan was to evaluate the binder effect of the ceramic coating on the separator properties, e.g. coating quality, electrolyte wettability, thermal stability, resistance. Polyvinylidene fluoride-co-hexafluoropropylene (PVDF-HFP) and carboxymethyl cellulose (CMC) were chosen as the binders based on previous studies. The three formulations of the Al_2O_3 slurries listed in Table I were investigated.

Table VIII Formulations of the Al_2O_3 Slurries

Binder	Compositions of Al_2O_3 (%)	Compositions of NMP (%)	Compositions of Deionized H_2O (%)	Compositions of Binders (%)
PVDF-HFP	39	60	0	1
CMC	39	0	60	1
PVDF-HFP CMC	39	30	30	0.5 PVDF-HFP 0.5 CMC

When preparing the slurry, the binder (PVDF-HFP, CMC, or a combination of the two) was dissolved in solvent (N-Methyl-2-pyrrolidone (NMP), deionized H₂O or a mixture of the two) to form a binder solution first. Then the ceramic (Al₂O₃) was dispersed in the binder solution. Additional solvent was added as needed to adjust the viscosity. The ceramic coating was applied to the uncoated separator via a doctor blade with a 50 μ m gap. For the slurry with mixed binders, an individual binder was dissolved in the corresponding solvent first. The appropriate amount of each binder solution was measured and mixed followed by dispersion of the ceramic. The coating was dried at 50°C. Photographs of the coatings are shown in Figure 97 (a) for PVDF-HFP, Figure 97 (b) for CMC and Figure 97 (c) for PVDF-HFP and CMC.

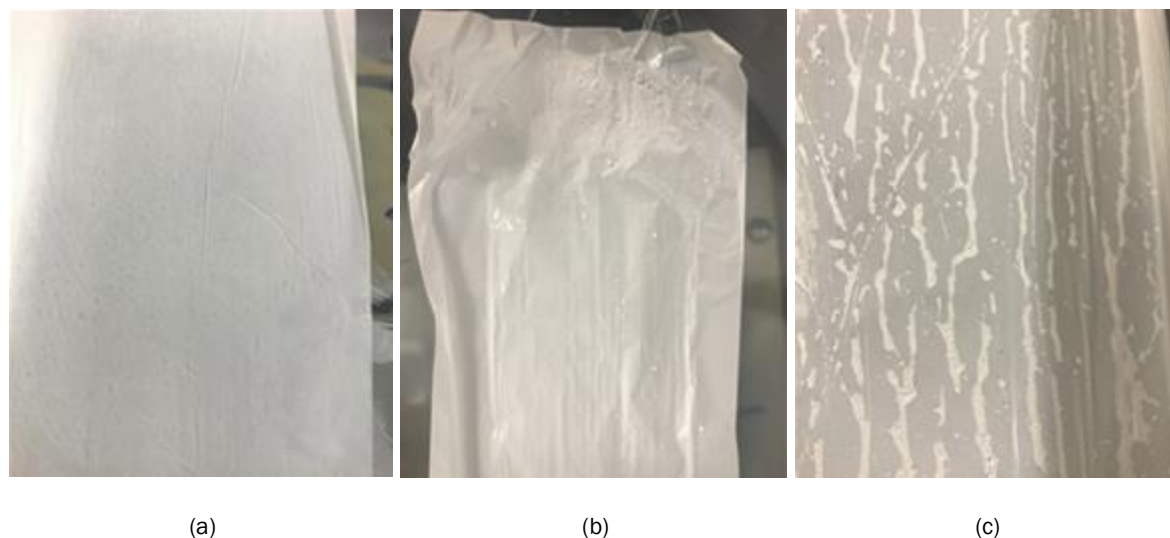


Figure 97 Ceramic coating on separators with various binders. (a) PVDF-HFP, (b) CMC and (c) PVDF-HFP and CMC. Source: ORNL

The separator with PVDF-HFP in NMP solvent had no significant agglomeration and its shape was good. In contrast, the separator with CMC exhibited binder wrinkling, indicating significant stress induced by the coating. The separator with mixed PVDF-HFP and CMC was the worst in terms of coating wetting and adhesion. Many ceramic particles fell off the surface, which could have been due to the low solubility of PVDF-HFP in the NMP/H₂O at a 50/50 weight fraction. Based on these observations, the experimental plan was slightly modified to investigate the composition of ceramics, Al₂O₃ and TiO₂, instead of binder effect.

NREL identified Carpe Diem, a supplier of specialized R2R equipment, as a suitable manufacturer for patterned gravure rolls. ORNL and NREL developed the final specification for the roll sizes and patterns. NREL also coordinated with ORNL on their development of titania and alumina slurries for the separator coatings. ORNL and NREL developed ink formulations of suitable viscosity for patterned spray coatings using the previously developed 3D printed masks for the separator substrate provided by Navitas. Additionally, NREL worked with the NREL Environmental Health and Safety group to develop a safe work procedure to enable the mixing and spraying of the ceramic nanoparticle inks.

The two ceramics, Al₂O₃ and TiO₂, were mixed in different Al₂O₃:TiO₂ ratios (1/0, 0/1, 1/1, 3/1, and 1/3) and coated onto the Navitas separator. The mixtures were 39 wt% of the ceramic, 1 wt% PVDF-HFP and 60wt.% NMP, mixed to a homogeneous slurry and coated onto the Navitas separator. Figure 98 (a) is the SEM image of the Al₂O₃ coated separator and Figure 98 (b) is the SEM for the TiO₂ coated separator. When preparing the slurry, the PVDF-HFP binder was dissolved in the NMP solvent to form a binder solution first, then the ceramic (Al₂O₃ or TiO₂) was dispersed in the binder solution. For the different ratios of ceramic, the two slurries were mixed in the required ratio and thoroughly stirred. Additional solvent was added as needed to adjust the viscosity of the slurries. Before coating, the slurries were filtered to get rid of agglomerates bigger

than 10 μm . The ceramic coatings were then applied to the uncoated Separator B separator via a doctor blade with a 10 μm gap resulting in a coated thickness of $\sim 8 \mu\text{m}$ after drying at 80 ° overnight to remove the solvent.

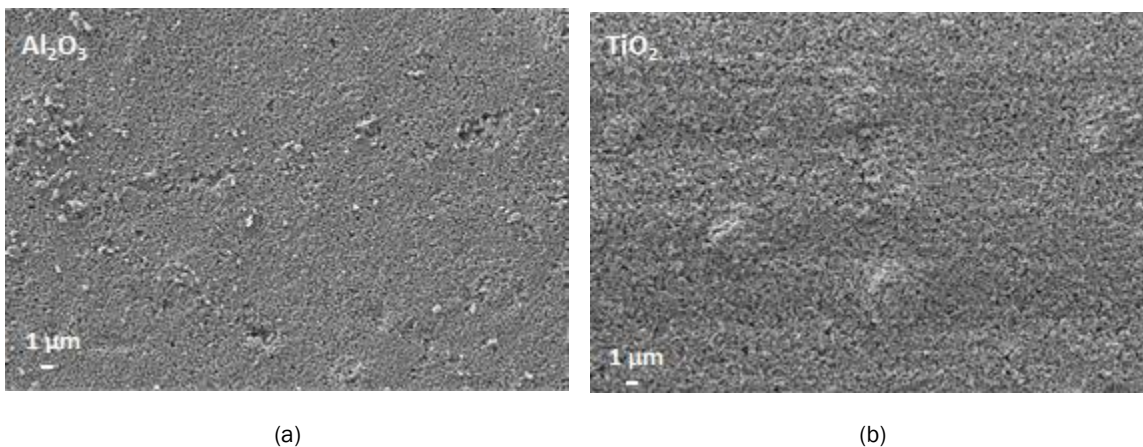


Figure 98 SEM images of (a) the Al_2O_3 coated separator and the (b) TiO_2 coated separator showing completely covered surfaces. Source: ORNL

The electrochemical impedance spectroscopy measurements were done by assembling a coin cell with each separator sandwiched between two stainless steel spacers and a single spring. The separators were soaked in the electrolyte and drip-dried before coin cell assembly. The resistance as a function of the thickness of the Al_2O_3 coating was recorded where an increase in the coating thickness produced an increase in the resistance as shown in Figure 99. The coating thickness of 30 μm shows a very high impedance of $\sim 78 \Omega$ as compared to $< 10 \Omega$ for the thinner coatings with 2.01 cm^2 .

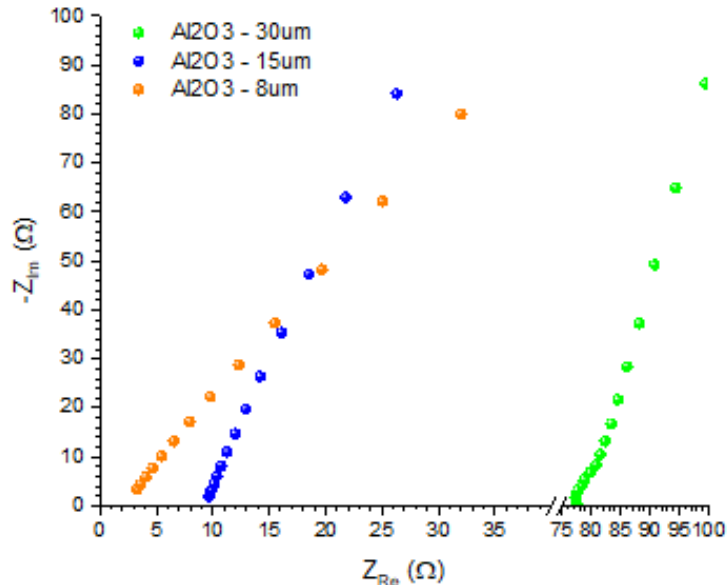


Figure 99 Electrochemical impedance spectroscopy results for the Separator B separator with different thicknesses of Al_2O_3 coatings. Source: ORNL

All the ceramics were then coated with a thickness of $\sim 8 \mu\text{m}$, giving impedance values of $0.85 \Omega/\text{cm}^2$, $1.79 \Omega/\text{cm}^2$, $1.44 \Omega/\text{cm}^2$, $1.19 \Omega/\text{cm}^2$ and $1.79 \Omega/\text{cm}^2$ for ceramic coatings Al_2O_3 , TiO_2 , $\text{Al}_2\text{O}_3 / \text{TiO}_2$ (1:1), $\text{Al}_2\text{O}_3 / \text{TiO}_2$ (3:1) and $\text{Al}_2\text{O}_3 / \text{TiO}_2$ (1:3), respectively as shown in Figure 100.

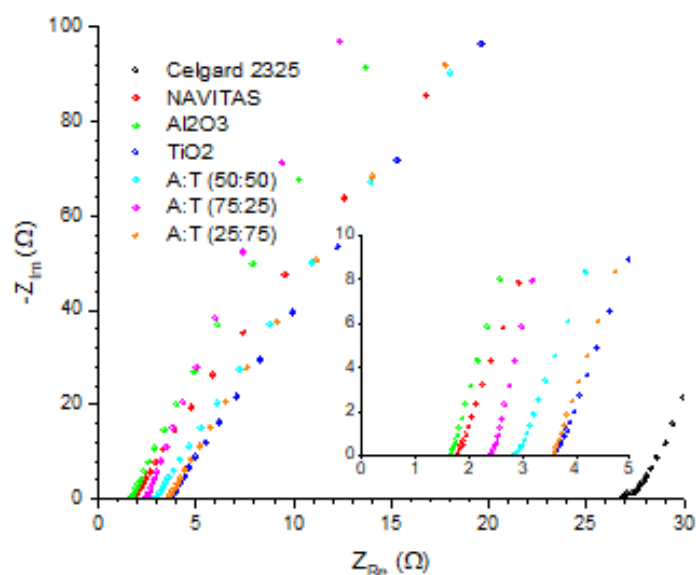


Figure 100 Electrochemical impedance spectroscopy results for the separators coated with the different ratios of Al_2O_3 and TiO_2 . Source: ORNL

The Al_2O_3 coating results in a relatively low impedance and the TiO_2 coating in higher impedance. For the ceramics in a ratio of 75:25 (Al_2O_3 / TiO_2) that were coated on the separator, the result was the lowest impedance for the coated separators.

NREL performed initial patterned-spray-coating experiments using an initial alumina slurry formulation from ORNL, separator material from Navitas, and full-sized 3D-printed pattern masks. As a first test, the alumina slurry/crosshatch pattern was sprayed. Figure 101 (a) shows one of the spray masks on the substrate prior to spraying and Figure 101 (b) shows the resulting alumina crosshatch pattern-sprayed separator. With this positive result, NREL then sprayed the full interdigitated pattern, i.e. titania/diamonds and alumina/crosshatch. In this second experiment, spatial non-uniformities in the coating thickness were observed as shown in Figure 102.



Figure 101 (a) 3D-printed spray mask and (b) alumina/crosshatch pattern-sprayed coating. Source: NREL



Figure 102 Separator with full interdigitated patterned coating showing spatial non-uniformities (e.g. lower left side of the image). Source: NREL

Based on the two preliminary spraying experiments described below, NREL performed a third experiment, with modified ink formulations and spraying conditions, and obtained interdigitated patterned coatings with much better uniformity.

The pore structure of the separators and electrochemical performance of the cells with the separators were characterized. To further investigate the effect of the coatings on the surface area of the separator with the different coatings, Brunauer-Emmett-Teller (BET) measurements were employed. Figure 103 (a) shows the N_2 physisorption isotherms of the uncoated and coated separators and Figure 103 (b) presents the data for the pore size distribution calculated from the desorption data for all separators. All the isotherms are representative of a Type-II isotherm which are indicative of a non-porous or macro-porous adsorbent. Additionally, at the low relative pressures (P/P_0), although minute, there is a sharp increase in the volume adsorption that indicates the presence of micropores (< 2 nm). All the measured separators are therefore macro-porous with a small amount of additional micropores. This corroborates SEM micrographs where macropores are observed in the uncoated separator. The isotherm for this separator also shows the initial low P/P_0 volume adsorption and therefore indicates micropores in the uncoated separator. With the coatings applied, a change in the BET surface areas is observed. With an Al_2O_3 coating (Separator 1), a decrease in the BET surface area, from $22.5 \text{ m}^2/\text{g}$ (uncoated) to $13.3 \text{ m}^2/\text{g}$, is observed. This indicates Al_2O_3 particles blocking the pores and decreasing the surface area, as can be observed in the isotherm where it starts to plateau at lower P/P_0 as compared to the uncoated separator. With the TiO_2 coating (Separator 2), a similar BET surface area of $23.2 \text{ m}^2/\text{g}$ was calculated as compared to the uncoated separator, and higher than that for the Al_2O_3 coated separator (Separator 1). This result confirms the data relative to the different types of coverages between Al_2O_3 and TiO_2 . For separator 3, with the Al_2O_3 and TiO_2 mixture of 50:50 wt.%, the surface area is also reduced. When reducing Al_2O_3 content and increasing TiO_2 simultaneously, the surface area increases.

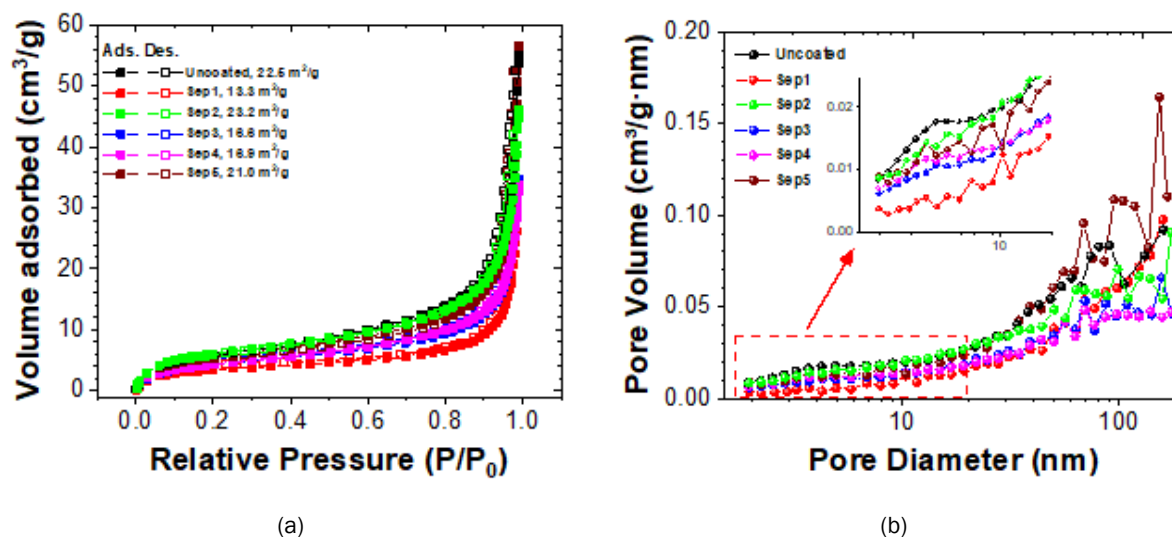


Figure 103 (a) N₂ physisorption isotherms of the uncoated and the differently coated separators with their corresponding BET surface areas and (b) their pore size distribution as calculated from the desorption data. Source: ORNL

All separators show hydrophobic behavior indicated by the large contact angles with water as shown in Figure 104. When switching water with electrolyte (1.2 molar LiPF₆ in ethylene carbonate – ethyl methyl carbonate electrolyte at 3/7 wt%), the contact angle is ~36° for the uncoated one and it is much smaller for the coated ones. The electrolyte diffuses into the coated separator quickly as well, indicating improved electrolyte wettability.

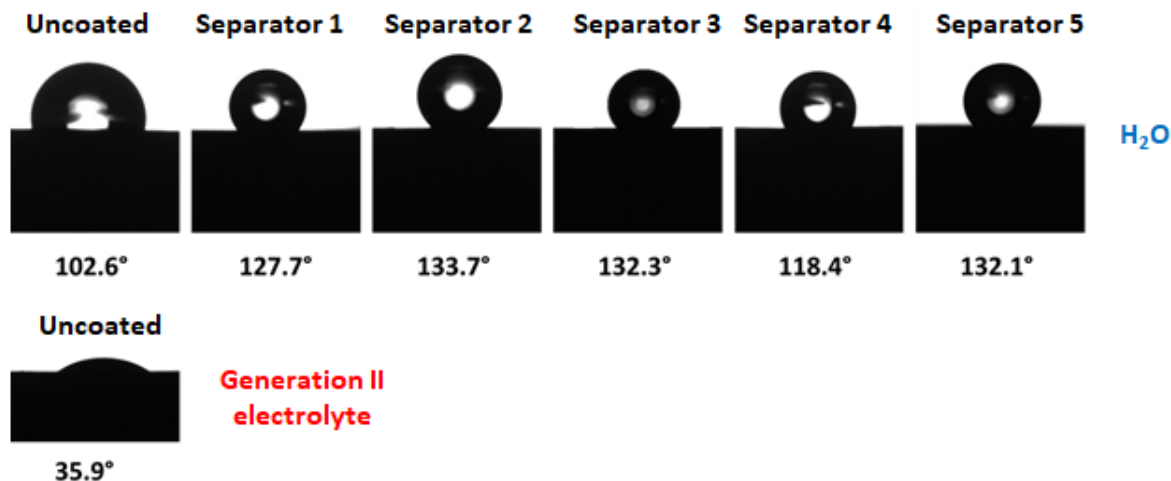


Figure 104 The average contact angle formed from water droplets on five separators with different coatings and from Generation II electrolyte on the uncoated separator. Source: ORNL

The electrochemical performance is identical at low rates shown in Figure 105 (a) and variations started at C/2 shown in Figures 105 (b) through (e). Generally, the cells with the uncoated separators are among the best performers, which is most likely ascribed to the thinner thickness (10 μm vs. 18 μm for the coated one).

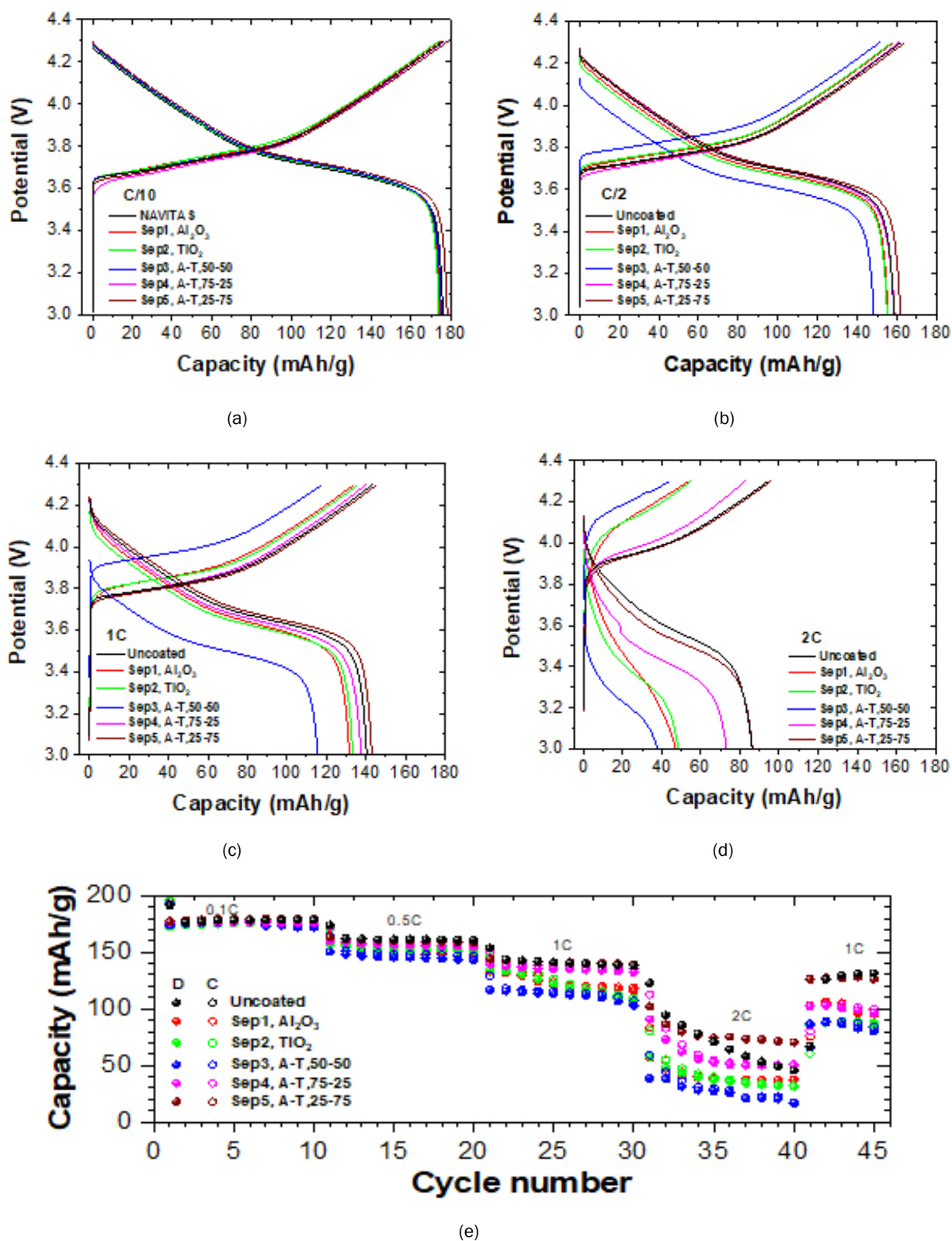


Figure 105 Voltage profile and rate performance with various separators at rates of (a) C/10, (b) C/2, (c) 1C, and (d) 2C. (e) The performance for all separators at all rates from 0 to 45 cycles. Source: ORNL

The stability of the separator was also investigated by means of self-discharge. The OCV was recorded for 350 hours after being fully charged to 4.3V. As can be seen in Figure 106, all cells with coated separators (except Separator 5) show less voltage drop compared to the uncoated one indicating less self-discharge rate.

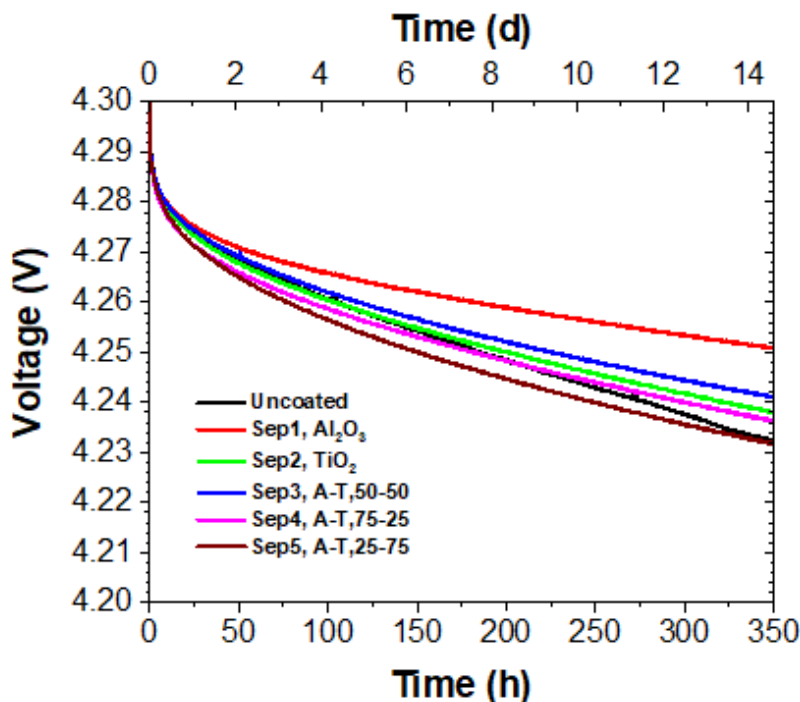


Figure 106 OCV of cells with various separators. Source: ORNL

NREL performed optical microscopy and SEM/EDS on the first series of interdigitated pattern-sprayed separators. Pinholes were observed in the microscopy, likely due to friction from the mask during the second coating. SEM/EDS at the pattern interface showed a clean transition from the TiOx to AlOx coatings. It also confirmed the microscopy, showing that spray droplets are not always coalescing into a contiguous coating.

After several spray process improvements and slight modification to the inks, a second series of patterned separators were sprayed. Quality was much improved, but residue was observed on the printed surfaces, likely due to dissolution of the 3D printed ABS mask in contact with the NMP solvent. As a result, NREL reformulated the inks with acetone rather than NMP and 3D printed new masks using Ultem, a melt-processable polymer with good stability to acetone. With the new inks and masks, a third series of patterned separators was sprayed. No residue was observed, but due to the change of solvent, it was observed that different spraying parameters must be used. A fourth coating series is planned.

NREL completed the hardware modifications on the coating station to enable forward gravure printing (making the drive motor reversible, reversing the mounting of the doctor blade, and machining new roll brackets and bearing seats), received the two patterned cylinders, and installed one in preparation for demonstration of gravure printing. Figure 107 shows the new hardware configuration for forward gravure and Figure 108 shows the two patterned gravure cylinders.



Figure 107 Side view of forward gravure setup. Source NREL



Figure 108 Patterned gravure rollers with a crosshatch pattern (top) and a diamond pattern (bottom). Source: NREL

SolarWindow Technologies, Inc. (SWT)

SolarWindow Technologies, Inc. partnered with NREL and ANL to demonstrate diffractive multiplexing for high-throughput R2R laser patterning of flexible organic PV modules.

Design and Selection of a DOE

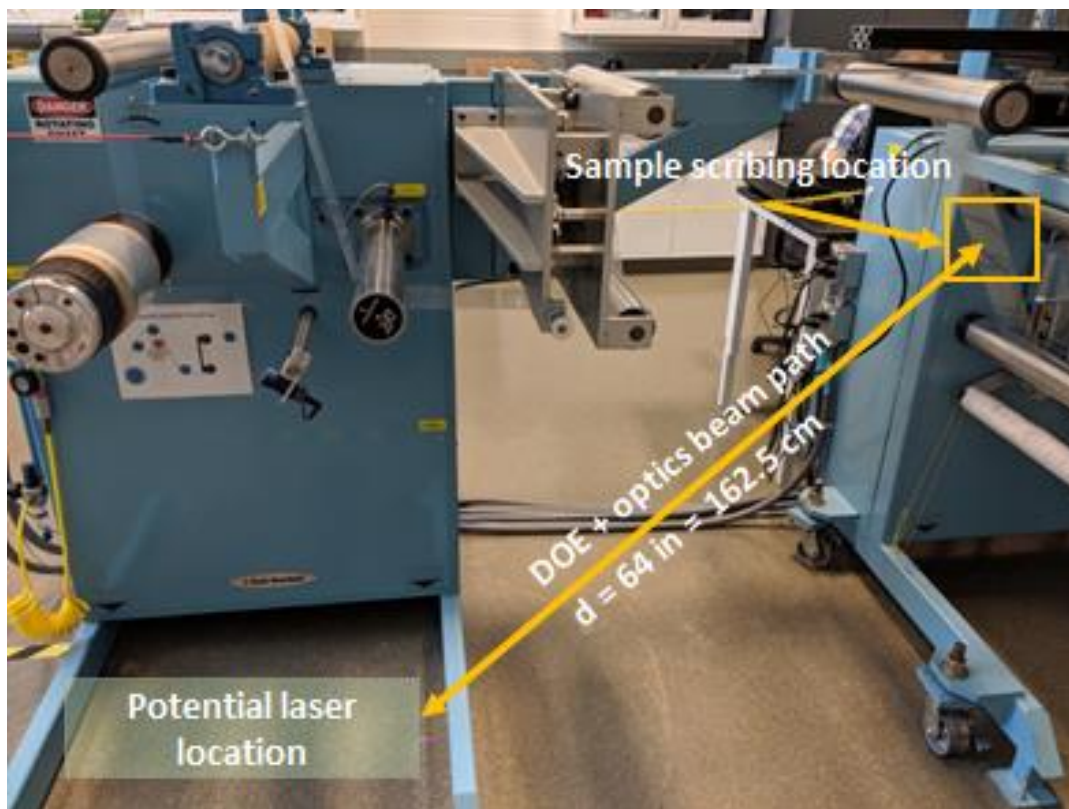
NREL worked closely with SWT to design and demonstrate diffractive optics-based laser multiplexing (DOL Multiplexing) process to perform parallel scribing across a web width with the use of a single laser source (DOL Multiplexing Process). The DOL Multiplexing Process involves designing and building the DOL Multiplexed scribing station and integrating it with an existing R&D scale R2R line. The fabrication of the DOL Multiplexing Process required the selection of the R2R line, design of DOL Multiplexed scribing station, design and selection of DOEs, fabrication of DOL Multiplexed Scribing Station, and laser beam alignment and tuning.

Custom optics for laser beam splitting and re-focusing were designed and fabricated by a vendor that specializes in laser optic studies and fabrication. NREL and SWT consulted and worked with the vendor to evaluate various DOL multiplexing designs. The feasibility study compared conceptual options for the optical design of a telecentric solution for material processing with multiple beams split by a diffractive beam splitter.

Each concept adhered to NREL and SWT specified parameters for wavelength, laser beam spots at the sample plane, beam spot separation distance, and 95% uniformity between spots. Based on the vendor study and recommendations, the most promising concept was chosen, and a more-detailed simulation of that optical configuration for the DOE was performed. SWT purchased custom diffractive optics and additional optical components (mirrors, power meter, etc.) and materials required for the fabrication of a laser safety enclosure.

Design of the DOL Multiplexing Scribing Station

The NREL R2R metrology line was selected as the system for integration of the R2R DOL multiplex scribing technology. Figure 109 (a) shows the metrology line and the planned locations of the laser system and the area on the web line where materials processing/scribing will occur. A laser safety enclosure was required by the NREL Environmental Health and Safety group to be integrated onto R2R metrology line as shown in Figure 109 (b). In addition to anodizing the entire enclosure to reduce light reflections, a custom ventilation system was installed into the enclosure that removes any material ablated from the web by the laser during the scribing. The laser ablation ventilation system was required by NREL Environmental Health and Safety to obtain “readiness verification” approval to operate the system.



(a)



(b)

Figure 109 (a) Annotated photo showing the proposed location of the laser and multiplexing optics on NREL diagnostic R2R line; (b) the R2R system for the multi-spot DOE scribing with the finished safety enclosure. Source: NREL

One task for the SWT CRADA project was the optimization of PV module coatings and subsequent scribing. Initially, about six meters of material with several layers, or thin films, of SWT device architecture were coated on NREL's R2R coating webline. The first film coating applied to the 12-in wide polyethylene terephthalate web was the bottom transparent electrode. This was followed by coating the photoactive and charge-selective layers of the solar cell stack that was 6-in. wide. This resulted in about two meters of each combination of layers—layer 1 for P1 scribing, layers 1+2+3 for P2 scribing and layers 1+2 for diagnostic purposes.

The P1 laser scribe was dialed in using the single-scribe laser system in NREL's Process Development and Integration Laboratory (PDIL). The laser power and the platform speed were adjusted to give a range of power densities. The stage was moved between 0.3 – 3.0 meter/min. Initial results showed a sizeable “processing window” that yields electrically-isolated P1 scribes that varied from low power and slow speeds to higher power and fast speeds. Next, the P2 scribing was dialed in to isolate the photoactive layers while preserving and exposing the bottom conductor.

Custom optics holders were fabricated for all optical components. A diffractive optic beam splitter is utilized to form uniform laser spots. A collimation lens parallelizes the beams, and each beam goes through a focusing lens to direct the split beams onto the surface of the R2R web sample. The laser ablation ventilation system is located below the web scribing to remove material ablated during scribing. To maintain compliance with NREL Environmental Health and Safety Regulations, all alignments, power adjustments, and scribing adjustments are monitored and performed remotely using a “web cam” within the enclosure while the laser is operating.

The first series of laser scribing was performed with a “slow” web speed of 0.6 m/min. With only gross alignment of the optics, several isolation lines were successfully scribed into the bottom transparent electrode coated on PET. Test results of the P1 scribes show electrical isolation of the bottom electrodes of each PV cell from its adjacent cell. Although the widths of the laser scribes vary slightly, all of the multiplexed scribes successfully isolate the bottom electrode creating individual sub cells. Fine tuning of the optics and laser powers was performed to achieve more uniform scribing widths will help improve sample aesthetics.

Optimization of PV Module Coatings and Scribing

Various P1 and P2 samples scribed with different scribing parameters — e.g. laser energy, laser repetition rate, and sample translation speed — were sent to collaborators at ANL for analysis using Scanning Electron Microscopy with Energy Dispersive X-ray Spectroscopy (SEM/EDS), and Raman microscopy. The initial results confirmed that the P1 scribes had complete removal of the conductive layers. The P2 scribes, however, required further optimization. Scribes using under- and over-powered laser conditions were intentionally included in the experiments. Optical microscopy and surface roughness profiling do not easily distinguish good from bad scribes, but distinguishing characteristics were clearly revealed by the SEM and Raman measurements.

To optimize the P1 scribing, NREL and SWT explored the effect of the scribing laser spot focal distance to scribe quality. A multi-lens focusing array was mounted on a micrometer so that the distance between the focusing lenses and the sample can be precisely controlled. Figure 110 shows how the distance is critical to the quality of the scribe. Too far away from the optimized focal length, the scribe is incomplete and does not electrically isolate adjacent cells. As the optimized focal distance is approached, the scribe quality is much better—thinner line and fully isolating. Unlike the single-laser scriber, the quality of the R2R multiplexed scribes seems to be more symmetric at the optimized focal length of around 50 mm. This is likely due to the fact that the R2R scribing uses a collimator before the focusing lenses.

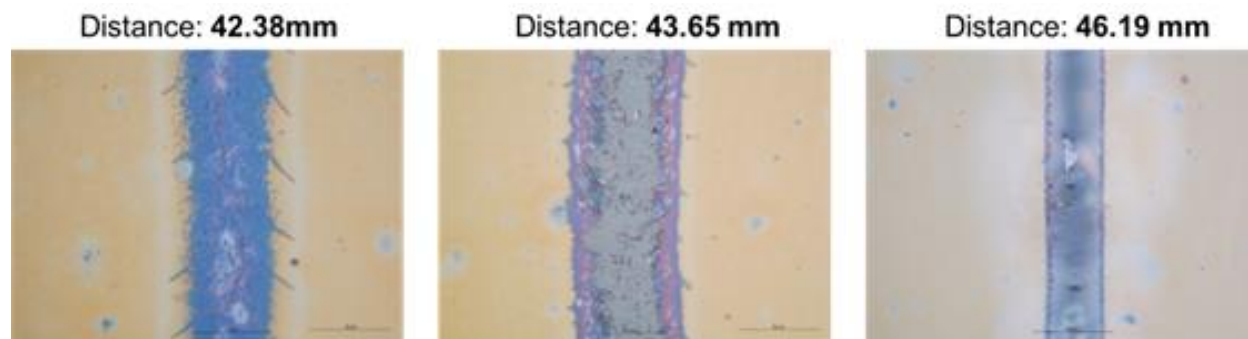


Figure 110 Optical microscope images of multiplexed DOL scribes in ZnO/ITO/PET as a function of laser spot focal distance. Source: NREL

To begin the build of the PV mini-module, NREL scribed several meters of P1 scribes on a conductive oxide/ITO/PET device on the R2R system. Comparable samples were made with single-laser P1 scribes. Approximately 6” x 6” sections were cut and coated with photoactive ink and finished with hole-collection and top contact layers. Neither set of mini-modules had good performance; most were shorted. A second set was made using the un-scribed portions of the electron transport/conductive contact/PET roll with various combinations of different photoactive inks (blade-coated) and evaporated top contacts. Working devices were made successfully with new solution formulations that will hopefully be better optimized for R2R coating as experiments progress. Based on an analysis of the multiplexed scribed device, it appears the electron transport layer used for the multiplexed laser P1 scribing was considered to be undercutting the device performance. Further optimization of all processes should solve this issue and result in devices that work as expected.

Nel/Proton OnSite

Nel/Proton OnSite has partnered with NREL, ORNL, and ANL to conduct research on R2R manufacturing of advanced (low loading, direct coated onto membrane) electrolysis electrodes for low-cost hydrogen production. Ink characterization and optimization, R2R coating, advanced electrode characterization, and metrology development capabilities at the labs will be used to support the overall goals of reducing the manufacturing labor for the membrane electrode assembly (MEA) by a factor of 15-20 and the overall cost of the MEA by over 60%.

In late in FY 2019, NREL, ORNL and ANL received foreign engagement approval from the DOE Office of International Affairs (IA) and received DOE site office approval for their roles in the project. As a result of IA coordination with FCTO, a joint work statement was coordinated with the FCTO Technology Manager and Proton OnSite. FCTO approved the final joint work statement for the CRADA which completed all approvals needed. The CRADA was executed in September 2019 and NREL has received project funds from ORNL. Project initiation is waiting receipt of project funds at ANL which is expected in the first quarter of FY 2020.

Workforce Development/Educational Outreach

The Collaboration laboratories integrated students and postdocs into all aspects of the program and ensured proper education and dissemination of information from the program thereby promoting a workforce with skill sets that support research, development and modeling for manufacturing technologies and processes. The R2R AMM DOE Laboratory Collaboration expanded its workforce development and educational outreach efforts in FY 2019 for the laboratories and universities listed in Table IX.

Table IX Educational Development at the Collaboration Laboratories

Collaboration Lab	Post Doc/Student/Intern	University
LBNL	Eongyu Yi, Post Doc Zhi Huang, Post Doc	University of Michigan Purdue University
ANL	Patrick Yang, Associate Devon Powers, Post Doc	Stony Brook University Vanderbilt University
ORNL	Ritu Sahore, Post Doc Anand Parejiya, PhD Student TJ Christensen, Tech Intern Erin Creel, Post Doc	Cornell University University of Tennessee Bredesen Center N/A University of California Berkeley
NREL	Sunil Khandavalli, Post Doc Min Wang, Post Doc Brian Green, Undergraduate Derek, Jacobson, Graduate Intern Mason Liu, Graduate Intern Radhika Iyer, Undergraduate Intern Janghoon Park, Post Doc Nisha Sharma, Post Doc	University of Massachusetts Amherst Case Western Reserve University University of Denver Colorado School of Mines University of Colorado at Boulder Northern Illinois University University of Massachusetts Amherst Western University (Ontario)
SNL	Chris Wall, Graduate Student Ben Wall, Graduate Student Lena Hoover, Graduate Student Sebastian Valencia, Graduate Student	New Mexico Tech (Albuquerque, NM) New Mexico Tech (Socorro, NM) University of New Mexico Georgia Institute of Technology
Total	20	18 different universities

Results of the research will be published and where applicable intellectual property be filed in collaboration with all contributing laboratories. The collaboration continued to reach out to industry to ensure technology transfer.

Challenges/Contingencies

The R2R AMM DOE Laboratory Collaboration built upon successes from the previous three-year consortium efforts in battery and fuel cell materials research and development. Because the FY 2020 projects began late in FY 2019 due to receipt of funding and there were new starts for early stage research program, the biggest programmatic challenge was to meet established and approved milestones after a delayed start. Task schedules and milestone dates were adjusted contingent on receipt of funding. An example of a technical challenge that occurred was having to redevelop the freeze tape casting parameters because of the different surface chemistry of the new LLZO powder. The contingency was that the industry partner was able to develop and share samples of LLZO dense layers which LBNL and ORNL used for producing bi-layers to mitigate project delays. Typical challenges occur when additional time is needed to get test equipment operational (downtime) or to receive new equipment and materials from vendors as well as negotiating contractual agreements which creates delays. One technical challenge that occurred in FY 2019 was that a coating layer in a PV stack—the ZnO electron transport layer—had unexpectedly poor performance. This challenge was met by developing new ZnO precursor solution chemistry that was more reliable.

Risks and Risk Handling

Early stage research usually has higher risks for the outcome of successful technologies compared to advanced development because of the nature of the basic science and phenomenology being investigated. Certain risks occur when funding or materials/equipment are not readily available to begin experimentation. Table X list some risks and their mitigation during FY 2019. When risks are identified as the project continues through FY 2021, research plans will be modified, and the appropriate risk management procedures will be used to eliminate or mitigate those risks in accordance with the DOE Risk Management Guide [4].

Table X Risks Identified During FY 2019 and Their Mitigation

Risks	Frequency	Impact	Rank	Mitigation
Novel R2R Deposition System Based on Electrospinning Technology and Advanced / In Situ Characterization and Testing Capabilities				
The vendor generates a delay in R2R module for ES system	low	Risk may cause delays in R2R ES machine customization and recipe implementation	high	(1) Communicate with the vendor in a biweekly basis to ensure the tool lead time (2) Start tool customization design in advance to reduce the overall customization time
Colloidal Chemistry, Surfactant Research, Slurry Processing, Deposition and Drying and Curing and Curing Methods				
FY19 funding delay of four months will put timing for initiating experiments in jeopardy	high	Four months of milestone slippage	high	Communicate the need to receive funding to the program sponsor

Physics and Methodologies for Multilayer Coatings/Deposition; Fabrication and In Situ Testing of Prototype Components and Devices; and Novel Non-Destructive Evaluation, Quality Control and Metrology				
The multi-layer slide die fabrication and delivery takes longer than quoted	low	Could delay FY 2019 and FY 2020 milestones related to the slide die	low	Various sequential multi-layer experiments can be performed to advance knowledge prior to receipt of the slide die. Also, as the project duration is 3-years, any slippage will be accommodated during the remainder of the project
Macroscopic Mathematical Model of the Drying of a Single Layer Generic Slurry Containing Monodisperse Colloidal Particles, Binder, and Solvent				
Accurate measurement of the fractal dimension of carbon black aggregations in polymer solution of different molecular weights	low	Accuracy of slurry model will be affected	low	Obtain SEM images of the carbon black structures and then modify the tool in ImageJ to get more accurate value of the fractal dimension
In-situ visualization of aggregates structures during mixing by using the new experimental setup	low	Data obtained will not be useful	low	Obtain a better digital optical microscope and then dilute the slurry solution to improve the visibility
Accurate tokenization of sentences and identification of materials entries	low	Accuracy of synthesis model will be affected	low	Develop heuristic algorithms to treat most common cases of incorrect tokenization and then create the algorithm for words/sentence tokenization in scientific texts
Validated Continuum-Scale Models to Accelerate Design and Scale-Up of Simultaneous Die Coating Process Technology				
Receipt of data from other labs to create/improve continuum models	low	Delay in providing models to other labs for developing their R2R processes	low	Communicate with the other labs on a regular basis to receive the data as soon as available
CRADA Projects				
The industry partner is unable to provide commercial LLZO powder for conducting the freeze tape casting experiments	low	Delay in obtaining the needed data by the end of the agreement period.	low	Labs will purchase a new commercially available LLZO powder from a different vendor. Slurry formulation and freeze tape casting parameters will have to be adjusted for the new powder possibly causing unknown delay for obtaining results

Project Ratings

Project performance assessments are determined through quantitative and qualitative methods in accordance with DOE Program and Project Management for the Acquisition of Capital Assets. [5] Programs are assessed by the following definitions: green – project is expected to meet its current performance baseline; yellow – project is potentially at risk of not meeting an element of the current performance baseline; red – project is highly at risk of requiring a change to the performance baseline by the Acquisition Executive or is not being executed within the acquisition strategy and Project Execution Plan.

Table XI provides the project overview for each laboratory and the overall program performance for FY 2019.

Table XI R2R AMM Laboratory Collaboration Project Ratings

ANL

Key Performance Indicator	Rating (red/green/yellow)	Status/Corrective Action
Performance	●	All performance targets were met.
Cost	●	Project cost was within FY 2019 budget.
Schedule	●	All tasks and milestones were met on schedule.

ORNL


Key Performance Indicator	Rating (red/green/yellow)	Status/Corrective Action
Performance	●	All performance targets were met.
Cost	●	Project cost was within FY 2019 budget.
Schedule	●	All tasks and milestones were met on schedule.

NREL




Key Performance Indicator	Rating (red/green/yellow)	Status/Corrective Action
Performance	●	All performance targets were met.
Cost	●	Project cost was within FY 2019 budget.
Schedule	●	All tasks and milestones were met on schedule.

LBNL




Key Performance Indicator	Rating (red/green/yellow)	Status/Corrective Action
Performance	●	All performance targets were met.
Cost	●	Project cost was within FY 2019 budget with carryover.

Schedule		All tasks and milestones were met on schedule.
-----------------	---	--

SNL

Key Performance Indicator	Rating (red/green/yellow)	Status/Corrective Action
Performance		All performance targets were met.
Cost		Project cost was within FY 2019 budget with carryover.
Schedule		All tasks and milestones were met on schedule.

OVERALL PROJECT

Key Performance Indicator	Rating (red/green/yellow)	Status/Corrective Action
Performance		All performance targets were met.
Cost		Project cost was within FY 2019 budget.
Schedule		All tasks and milestones were met on schedule.

Conclusions

FY 2019 was the first year of a three-year project for early stage research and development on R2R advanced technologies in a national multi-laboratory collaboration that will deliver advances in the fundamental understanding of R2R processing on moving webs, carriers, or other substrates and develop tools, metrology approaches, processes, and new materials to improve yields, overall quality, processing rates and reduce cost. Technologies under development will overcome the lack of scalability and understanding of fundamental chemistry and materials properties demonstrated on selected key technology applications with cross-cutting impacts. Nanofibers applicable to solid electrolytes, fuel cell electrodes and water filtration membranes were fabricated and a prototype ES system with 56 specially-designed nozzles that enable multiple jets of electrospun fibers to be applied on a R2R web was developed by ANL. PEMFC cathode GDE coatings of uniform thickness were produced on the ORNL pilot slot-die coating line and a membrane electrode assembly of the slot-die coated GDE was fabricated and tested at NREL. Cubic-phase LLZO with orders of magnitude more conductivity was processed by ORNL using improved annealing conditions.

Multiple modeling and simulation efforts were completed in FY 2019. NREL leveraged an empirical slide die coating window model and developed full-quadratic ink models for catalyst ink surface tension. These models were provided to SNL for further development of multi-layer slide die continuum models. NREL also completed a study showing a multi-region process window characterized by droplet spraying, spinning of fibers and beads, and an unstable flow region with viscous instability in the Taylor cone. LBNL developed a generic particle network settling model as part of its longer-term coating drying modeling efforts; however, recognizing the deep lack of fundamental knowledge about the concentrated dispersions of interest, proposed a set of novel experiments for probing the influence of component interactions on macroscopic dispersion behavior. LBNL proposes to design and execute these experiments in order to obtain information that will be incorporated into its multilayer coating drying models. SNL completed their two-layer slide coating and slot coating models using Goma 6.0 that will allow for accelerated process development. The capillary hydrodynamic slide-die coating model was designed using the geometry of the NREL slide die. For two-layer

systems, the model can predict interlayer and free surface shape at varying flowrates and web speeds focused on minimizing flow recirculation near interlayer and preventing interlayer mixing. Additionally, models for slot- and slide-deposition systems with accommodation for three or more simultaneous miscible layers (multiple layers of varying rheology) were developed.

Three CRADA projects that initiated in mid-FY 2018 continued through FY 2019 with one project completing in May 2019. One project demonstrated the feasibility of a pilot-scale freeze-casting coating and made initial recommendations to the industry partner on how the freeze casting process could be industrially scaled. A second project resulted in a down-selection of an improved separator material and trial operations handling the separator in a R2R manner began at the industry partner product site. The third project selected a DOE-based multiplexing system for R2R laser scribing that will drastically reduce up-front capital and on-going operational costs compared to currently used laser/optics systems and will also increase process speeds over galvanometer step-and-scan systems. Scribing experiments were initiated, and optimization of the scribing process continued through FY 2019.

Efforts will continue for the projects that began in FY 2019 with the goal of advancing our understanding of R2R processing for high-throughput advanced manufacturing to enable new devices and lower the cost of existing processing routes for competitive U.S. manufacturing. The projects directly support the AMO's Multi-Year Program Plan challenges for the use of multilayer coating technologies applicable to flexible and integrated electronics, separation membranes, PVs, and selective barrier materials addressing the AMO identified targets of technologies with a 10x production capacity increase and in-line instrumentation tools to evaluate the performance and functionality.

Key Publications

Doeff, M.M; Yi, E.; Shen, H., Chen, G.; Sofie, S. "Towards Scalable Manufacturing of Solid State Batteries", Presentation at the 236th meeting of the Electrochemical Society, Atlanta GA, Oct. 13-17th, 2019.

Khandavalli S.; Park, J.H., Kariuki, N.N.; Myers, D.J.; Stickel, J.J.; Hurst, K.; Neyerlin, K.C.; Ulsh, M.; Mauger, S.A. "Rheological investigation of fuel cell catalyst inks." Presentation at the Society of Rheology meeting, Houston, TX; October 2018.

Khandavalli, S.; Park, J.H.; Kariuki, N.N., Myers, D.J.; Stickel, J.J.; Hurst, K.; Neyerlin, K.C. Ulsh, M.; Mauger, S.A. 2018. "Rheological Investigation on the Microstructure of Fuel Cell Catalyst Inks", ACS Appl. Mater. Interfaces, Vol. 10, pp 43610–43622.

Khandavalli S., Park J.H., Kariuki N.N., Zaccarine S.F., Pylypenko S., Myers D.J., Ulsh M., Mauger S. 2019 "Investigation of the microstructure and rheology of iridium oxide catalyst inks for low-temperature PEMWE." ACS Appl Mater Interfaces, 11 (48) 45068-45079.

Wang, M.; Park, J.H.; Kabir, S.; Neyerlin, K.C.; Kariuki, N.N; Lv, H.; Stamenkovic, V.R; Myers, D.J.; Ulsh, M.; Mauger, S.A. 2019. "The Impact of Catalyst Ink Dispersing Methodology on Fuel Cell Performance Using In-situ X-ray Scattering", ACS Appl. Energy Mater. July 26, 2019, 2, 9, 6417-6427
<https://doi.org/10.1021/acsaem.9b01037>

Wood, III, D.L.; M. Wood, Z. Du, J. Li, I. Belharouak, R. Rao, and S. Solberg, "Materials Processing and Performance Challenges of Thick Electrodes for High Energy Density Li-Ion Batteries," 70th Southeastern Regional Meeting of the American Chemical Society (SERMACS 2018), Augusta, Georgia, October 31 – November 3, 2018. **(Invited)**

Wood, III, D.L.; M. Wood, J. Li, Z. Du, C. Daniel, A. Dunlop, B. Polzin, A. Jansen, G. Krumdick, P. Rupnowski, M. Ulsh, F. Ma, V. Battaglia, and R. Prasher, "Advanced Processing Considerations for Lithium-

Ion and Polymer Electrolyte Fuel Cell Electrode Coatings,” AIMCAL R2R Conference, Phoenix, Arizona, October 28-31, 2018. (Invited)

References

1. Howell, D. “Vehicle Technologies Office Electrochemical Energy Storage R&D Overview”. (2017), The 2017 U.S. Department of Energy (DOE) Fuel Cell Technologies Office (FCTO) and Vehicle Technologies Office (VTO) Annual Merit Review and Peer Evaluation Meeting (AMR), Washington, DC, June 6, 2017. https://www.energy.gov/sites/prod/files/2017/06/f34/es000_howell_2017_o.pdf
2. Garland, N. “Manufacturing R&D Program Area - Plenary Presentation”. (2017), The 2017 U.S. Department of Energy (DOE) Fuel Cell Technologies Office (FCTO) and Vehicle Technologies Office (VTO) Annual Merit Review and Peer Evaluation Meeting (AMR), Washington, DC, June 6, 2017. https://www.hydrogen.energy.gov/pdfs/review17/mn000_garland_2017_o.pdf
3. Macknick, J.; Newmark, R.; Heath, G.; Hallett, KC. “A Review of Operational Water Consumption and Withdrawal Factors for Electricity Generating Technologies”. (2011) Technical Report NREL/TP-6A20-50900, March 2011. <https://www.nrel.gov/docs/fy11osti/50900.pdf>
4. DOE Risk Management Guide, DOE G 413.3-7A 1-12-2011, updated October 22, 2015 <https://www.energy.gov/projectmanagement/directives>
5. DOE Program and Project Management for the Acquisition of Capital Assets, DOE 413.3B updated April 12, 2018. <https://www.energy.gov/projectmanagement/directives>

